NUMERICAL MODELING OF LONG WAVES FROM ATYPICAL SOURCES: ATMOSPHERIC DISTURBANCES AND VOLCANIC ORIGIN

A THESIS SUBMITTED TO
THE GRADUATE SCHOOL OF NATURAL AND APPLIED SCIENCES
OF
MIDDLE EAST TECHNICAL UNIVERSITY

BY

GÖZDE GÜNEY DOĞAN BİNGÖL

IN PARTIAL FULFILLMENT OF THE REQUIREMENTS
FOR
THE DEGREE OF DOCTOR OF PHILOSOPHY
IN
CIVIL ENGINEERING

JUNE 2022

Approval of the thesis:

NUMERICAL MODELING OF LONG WAVES FROM ATYPICAL SOURCES: ATMOSPHERIC DISTURBANCES AND VOLCANIC ORIGIN
submitted by **GÖZDE GÜNEY DOĞAN BİNGÖL** in partial fulfillment of the requirements for the degree of **Doctor of Philosophy** i**n Civil Engineering, Middle East Technical University** by,

Prof. Dr. Halil Kalıpçılar
Dean, Graduate School of **Natural and Applied Sciences** _____

Prof. Dr. Erdem Canbay
Head of the Department, **Civil Engineering** _____

Prof. Dr. Ahmet Cevdet Yalçıner
Supervisor, **Civil Engineering, METU** _____

Examining Committee Members:

Prof. Dr. İsmail Aydın
Civil Engineering, METU _____

Prof. Dr. Ahmet Cevdet Yalçıner
Civil Engineering, METU _____

Prof. Dr. Utku Kânoğlu
Aerospace Engineering, Dokuz Eylül Uni. _____

Prof. Dr. Efim Pelinovsky
Fundamental Mathematics, Russia National Research Uni. _____

Assist. Prof. Dr. Cüneyt Baykal
Civil Engineering, METU _____

Date: 30.06.2022

I hereby declare that all information in this document has been obtained and presented in accordance with academic rules and ethical conduct. I also declare that, as required by these rules and conduct, I have fully cited and referenced all material and results that are not original to this work.

Name Last name : Gözde Güney Doğan Bingöl

Signature :

ABSTRACT

NUMERICAL MODELING OF LONG WAVES FROM ATYPICAL SOURCES: ATMOSPHERIC DISTURBANCES AND VOLCANIC ORIGIN

Doğan Bingöl, Gözde Güney
Doctor of Philosophy, Civil Engineering
Supervisor : Prof. Dr. Ahmet Cevdet Yalçıner

June 2022, 148 pages

Earthquakes are the main cause mechanisms of tsunamis and large tsunamigenic earthquakes, especially in the subduction zones, occur on relatively much shorter timescales, but destructive tsunamis are also produced by volcanic eruptions, which have been threatening the coastal communities throughout history. Furthermore, while earthquake-generated tsunamis have been studied immensely, there is less focus on research related to tsunamis induced by atmospheric disturbances (meteotsunamis). Consequently, this study focuses on numerical modeling of long waves (tsunamis and meteotsunamis) sourcing from those atypical origins, volcanic activities and atmospheric disturbances and investigates the complex mechanisms behind them.

Initially, scenario-based research for the numerical modeling of the December 2018 Gunung Anak Krakatau tsunami was conducted to investigate the possible source mechanisms and their contribution to explaining the observed sea level disturbances. A flank collapse (partial destabilization of the volcano) scenario was suggested appearing capable of generating the observed tsunami along the coast of the affected area, Sunda Strait. Coupling of a two-layer landslide model and a hydrodynamic model was performed to test the ability of such an implementation to reproduce a

recent and large-scale volcanic eruption induced tsunami via post-tsunami field survey observations and tide gauge record comparisons.

Secondly, the long wave generation and amplification induced by spatial and temporal changes of the atmospheric pressure disturbance is numerically solved by introducing pressure and wind field terms to the nonlinear shallow water equations. Several numerical tests are conducted to compare against a new analytical solution for meteotsunami generation in water channels of quasi-parabolic shape (including triangular cross-section) and satisfactory results with less than 1% error are achieved. Furthermore, the possible wave amplification factors, oceanographic and hydrodynamic, are investigated via more than 500 simulations based on different basin configurations and pressure field characteristics, prepared with the "isolation of parameter" principle in mind. The influence of the wind field characteristics, which is the other contributing forcing mechanism in meteotsunami generation but lacks sufficient coverage in literature, on the wave response is also discussed based on several numerical tests. The relationships between the parameters and the possible wave amplification mechanisms are discussed based on the empirical curves derived from the simulation results.

Finally, the propagation of the air pressure waves induced by the January 2022 Hunga Tonga-Hunga Ha'apai volcanic explosion and the consequent sea waves are modeled globally. Two different modeling approaches are proposed to solve the air pressure propagation: i) development of a synthetic pressure model based on barometric measurements and ii) implementation of the nonlinear shallow-water theory using an initial disturbance at the volcano. Then, the hydrodynamic model was forced with the produced pressure fields to compute the resulting tsunami waves in the Pacific Ocean, the Caribbean and the Mediterranean. The modeling results are presented with discussions on the possible sea level amplification mechanisms. Fairly well agreement between the computed and measured air pressure waves and sea levels at several locations around the globe is promising for explaining the far reach and long duration of the tsunami generated by the Hunga Tonga-Hunga

Ha'apai eruption. The suggested novel approaches can be alternative modeling applications for such phenomena with the efficient utilization of global data available for such an event for the first time.

Keywords: Numerical Modeling, Tsunami, Meteotsunami, Atmospheric Disturbance, Volcanic Origin

ÖZ

ATİPİK KAYNAKLARDAN KÖKEN ALAN UZUN DALGALARIN SAYISAL MODELLEMESİ: ATMOSFERİK DEĞİŞİKLİKLER VE VOLKANİK KÖKEN

Doğan Bingöl, Gözde Güney
Doktora, İnşaat Mühendisliği
Tez Yöneticisi: Prof. Dr. Ahmet Cevdet Yalçıner

Haziran 2022, 148 sayfa

Depremler, tsunamilerin ana kaynak mekanizmaları olup tsunami oluşturan büyük depremler özellikle dalma zonlarında nispeten daha sık meydana gelse de volkanik patlamalara bağlı yıkıcı tsunamiler de tarih boyunca kıyı topluluklarını tehdit eden bir unsur olmuştur. Bu durum son yıllarda yaşanan volkanik olaylara bağlı oluşan tsunamiler ve yüksek etkileri ile tekrar gün yüzüne çıkmıştır. Deprem kaynaklı tsunamiler konusunda çok fazla araştırma mevcuttur. Ancak bugüne kadar yapılan çalışmalarda atmosferik değişiklikler veya bir başka söylemle meteorolojik olayların neden olduğu tsunamilere (meteotsunamiler) çok daha az odaklanılmıştır. Dolayısıyla, bu çalışmada, bu tipik olmayan kökenlerden, volkanik faaliyetler ve atmosferik değişikliklerden kaynaklanan uzun dalgaların sayısal modellemesine odaklanılmış ve bunların arkasındaki karmaşık mekanizmalar araştırılmıştır.

İlk olarak, olası kaynak mekanizmalarını ve bu mekanizmaların gözlemlenen deniz seviyelerine katkısını araştırmak için Aralık 2018 Gunung Anak Krakatau tsunamisinin sayısal modellemesi için senaryo tabanlı bir çalışma yapılmıştır. Oluşan tsunaminin başlıca kaynağı olabilecek bir senaryonun, kısmi destabilizasyona bağlı yamaç çökmesi, etki alanı olan Sunda Boğazı kıyıları boyunca

gözlemlenen tsunami dalgalarını oluşturabilecek nitelikte olduğu ortaya koyulmuştur. İki katmanlı bir heyelan modeli ile bir hidrodinamik model birleştirilerek, böyle bir uygulamanın, büyük ölçekli bir volkanik patlamanın neden olduğu tsunamiyi yeniden üretebilme kapasitesi tsunami sonrası saha araştırması verileri ve mareograf ölçümleri ile karşılaştırılarak incelenmiştir.

İkinci olarak, atmosferik basınç değişikliklerinin alansal ve zamansal değişimlerine bağlı olarak meydana gelen uzun dalgaların oluşumu ve amplifikasyonu, doğrusal olmayan sığ su denklemlerine hava basıncı ve rüzgar alanı terimleri dahil edilerek sayısal olarak çözülmüştür. Çok sayıda sayısal test gerçekleştirilmiş, yarı parabolik şekilli (üçgen kesit dahil) su kanallarında meteotsunami oluşumu için yeni bir analitik çözümle karşılaştırmalar yapılmış ve %1'den daha az hatayla tatmin edici sonuçlar elde edilerek model doğrulanmıştır. Ayrıca, olası oşinografik ve hidrodinamik dalga amplifikasyon faktörleri, "parametrelerin izolasyonu" ilkesi göz önünde bulundurularak hazırlanan farklı basen ve basınç alanı özelliklerine bağlı konfigürasyonlar ile 550'den fazla simülasyon yapılarak araştırılmıştır. Meteotsunami oluşumundaki bir diğer etki mekanizması olan ancak literatürde yeterli yer bulamamış rüzgar alanlarının özelliklerinin oluşan dalgalar üzerindeki etkisi de çok sayıda sayısal test ile incelenmiştir. Her bir parametre ve dalga amplifikasyonu arasındaki ilişki, simülasyon sonuçlarından elde edilen gözlemler ile tartışılarak sunulmuştur.

Son olarak, Ocak 2022 Hunga Tonga-Hunga Ha'apai volkanik patlamasının neden olduğu hava basıncı dalgalarının yayılması ve volkanik kökenden oluşan hava basıncı dalgalarının oluşturduğu deniz dalgaları küresel ölçekte modellenmiştir. Basınç dalgalarının yayılımını çözmek için iki farklı modelleme yaklaşımı önerilmiştir. Bu yaklaşımlar: i) barometrik ölçümlere dayalı sentetik bir basınç modelinin geliştirilmesi ve ii) patlama anında oluşan basıncın eşdeğeri su yuksekliği volkanda ilk koşul olarak verilerek, doğrusal olmayan sığ su teorisinin basınç dalgaları yayılımının çözülmesi için uygulanmasıdır. Ardından, üretilen basınç alanları hidrodinamik modelde girdi olarak kullanılmış, Pasifik Okyanusu,

Karayipler ve Akdeniz'de ortaya çıkan tsunami dalgaları hidrodinamik model ile hesaplanmıştır. Modelleme sonuçları, olası dalga büyütme mekanizmalarına ilişkin tartışmalarla birlikte sunulmuştur. Dünyanın farklı bölgelerinde hesaplanan ve ölçülen hava basıncı dalgası profilleri ve deniz seviyesi ölçümleri arasındaki oldukça iyi uyumun, Hunga Tonga - Hunga Ha'apai patlaması tarafından oluşturulan tsunami dalgalarının uzak mesafeli ve uzun süreli ilerlemesinin açıklanması için umut verici olduğu söylenebilir. Önerilen özgün yaklaşımlar, böyle bir olay için ilk kez mevcut olan küresel verilerin verimli kullanımı ile, bu tür olaylar için alternatif modelleme uygulamaları olabilecektir.

Anahtar Kelimeler: Sayısal Modelleme, Tsunami, Meteotsunami, Atmosferik Düzensizlik, Volkanik Köken

To the angel of my life, Gülistan…

ACKNOWLEDGMENTS

I would like to express my deepest gratitude to my supervisor Prof. Dr. Ahmet Cevdet Yalçıner, for his guidance, advice, criticism, encouragement and insight not only throughout this research but also in life. Words cannot express how grateful I am for our long hours of discussions, his patience during hard times, for sharing his experience on many subjects, and all the precious moments we spent together. I always knew that I could share anything in my life with him; he has been more of a "PhD father" than a supervisor. He has always believed in me and never let me give up, even though I failed from time to time. His supervision, solution-oriented approaches and perspectives on life always inspired me and enlightened my way. I am also so thankful to him for his continuous support and for providing me with several different opportunities to improve my research skills and experience. I am sure our strong relationship will continue endlessly, stating that I have tears in my eyes while writing these lines.

I also want to thank Prof. Dr. Ayşen Ergin for her endless positive energy, support, enlightening conversations and joyful memories. I have always admired her and feel fortunate to be one of her graduate students. Her nice compliments have always given me great motivation and made my day better.

I feel grateful to Dr. Işıkhan Güler for his endless support, motivation and, his faith in me. His efforts to solve any problem that we face and his constructive approaches to creating a friendly environment in our laboratory are so valuable. I am happy that he has been one of my mentors, but he means much more to me. I am also grateful for our long and rich content discussions on life issues that have been incredibly useful to me.

I want to express my sincere thanks to Dr. Gulizar Ozyurt Tarakcioglu and Dr. Cuneyt Baykal for their support during my graduate studies, their efforts to improve

the collaborative work in the laboratory and their thoughtful approaches to graduate students.

I would like to express my special thanks to my dear colleague Dr. Gokhan Guler for his endless support, awesome friendship and the feeling of knowing that he is and will be always there. It is a great chance to be with sincere people with whom you can be friends and colleagues, have fun, share, work and produce together.

I would like to thank Prof. Dr. Mehmet Lütfi Süzen for his support and Duygu Tüfekçi-Enginar for her friendship and efforts and support in all our collaborative works.

My sincere gratitude is also to Prof. Dr. Efim Pelinovsky, Prof. Dr. Fumihiko Imamura, Prof. Dr. Andrey Zaytsev, Assoc. Prof. Dr. Ira Didenkulova, Dr. Öcal Necmioğlu, Prof. Dr. Mehmet Semih Yücemen, Prof. Dr. Orhan Polat, Prof. Dr. Yalçın Yüksel, Dr. Alessandro Annunziato and my thesis monitoring committee members Prof. Dr. İsmail Aydın and Prof. Dr. Utku Kânoğlu for all the valuable support and contributions at different stages of this study with their tremendous experience.

My special thanks to my colleague and roommate, Bora Yalçıner, who has always been kind and helpful to me. I also thank him for his outstanding performance in upgrading the numerical code NAMI DANCE SUITE in the GPU environment.

I would like to extend my special thanks to Yağız Arda Çiçek, Ufuk Şentürk, Koray Deniz Göral, Can Özsoy, Kadir Karakaş, Mert Yaman, İlker Çoban, Sedat Gözlet, Ghazal Khodkar, Aslıhan Devran, for making life better during this long journey. I would like to also thank the MSc students Bilge Karakütük and Furkan Demir for their help during this study. Nuray Emre and Yusuf Korkut are also gratefully acknowledged for their help.

I feel grateful to have my dear friends, Naeimeh Sharghivand, Ramez Mohammadi, Arın Özge Himmetoğlu, Merih Himmetoğlu, Yağmur Öztürk, Bircan Işık and Ilgın

Akbıyık, and my dear extended family members, Veli Doğan, Nilgün Doğan and Saniye Özkan without whom it would be much difficult to overcome the tough times. I feel so lucky to be surrounded with these amazing people.

My family, Habib Doğan, Seval Doğan and Ali Doğan, deserves special thanks for their continued and committed support, help, huge contributions to my life, and unconditional love. They did not stop supporting me for a second. I am unsure if I could succeed in completing this study without them. Mustafa Bingöl, Dilek Bingöl, and Cemre Bingöl are also gratefully acknowledged for their love and support during the last years of this study.

The most special and sincere thanks go to my dear husband, my other half, Cem Bingöl, who is truly one in a million. I am so grateful for his endless, unconditional love and support that I always feel from the heart. His patience during the hard times, even when I become a tough person to endure and his attitude of never letting go of my hand is invaluable. His understanding when I stole many times from our spare time to work more is admirable. I am so thankful for meeting him, being his other half, and for all the priceless moments we shared. This study surely would not be possible without him.

I would like to also express my profound gratitude to my sweetheart grandmother, Gülistan, who passed away but will always be with me in my heart. She is the most special person I have ever met. Without her and her unconditional and committed love and support, I would not be who I am today. I owe so much to her and always feel her precious touch on my life.

This thesis was partly supported by EC project Assessment, Strategy And Risk Reduction for Tsunamis in Europe - FP7-ENV2013 6.4-3, Grant 603839 (ASTARTE), and Japan–Turkey Joint Research Project by JICA on earthquakes and tsunamis in Marmara Region by MarDim SATREPS, TUBITAK 221M750, 213M534, 113M556, 108Y227 projects and AFAD Grant UDAP-Ç-12-14. EP acknowledges RFBR grants (20-05-00162, 18-05-80019, 19-55-15005). I also

acknowledge President Grants NS-2485.2020.5 and MD-148.2020.5 and ETAG grant PUT1378 for partial support to the papers published within this study.

I am thankful to Dr. Udrekh from Agency for the Assessment and Application of Technology (BPPT) for the bathymetry/topography data provided in the close area of Gunung Anak Krakatau. The institutions of the Coordinating Ministry for Maritime Affairs (CMMA-RI), Ministry of Maritime Affairs and Fisheries (MMAF-RI), and Indonesian Tsunami Scientific Community (IATsI) are also gratefully acknowledged for providing the tide-gauge data in the Sunda Strait and close collaboration.

I thank Dr. Pakoksung Kwanchai from the International Research Institute of Disaster Science (IRIDeS), Tohoku University, for his invaluable support in landslide modeling.

NAMI DANCE was initiated in collaboration with Ocean Engineering Research Center, Department of Civil Engineering, Middle East Technical University, Turkey, and Institute of Applied Physics, Russian Academy of Sciences, and Special Research Bureau for Automation of Marine Researches, Far Eastern Branch of Russian Academy of Sciences, Russia.

I also acknowledge the Weathernews Inc. meteorological observation system for providing barometric pressure data from Soratena weather sensors in Japan and the Turkish State Meteorological Service for atmospheric pressure data from the meteorological stations in Turkey. I also acknowledge the CALYPSO SOUTH project, partly financed by the EU under the Operational Programme Italia-Malta 2013-2020, and co-ordinated by Prof. Aldo Drago from the Physical Oceanography Research Group of the University of Malta for providing data in Malta. The Indonesian authorities are also acknowledged for providing barometric data in Prigi.

TABLE OF CONTENTS

LIST OF TABLES

TABLES

LIST OF FIGURES

FIGURES

LIST OF SYMBOLS AND ABBREVIATIONS

a_{peak}	Peak amplitudes of the pressure wave
a_{trough}	Trough amplitudes of the pressure wave
B_w	Bandwidth of the atmospheric pressure forcing
B_w	Bandwidth of the atmospheri pressure disturbance
c	Wave celerity
C_d	Drag coefficient
c_j	Propagation phase speed of jth mode of edge waves
c_{peak}, c_{trough}, c_1, c_2	Empirical constants
D	Total water depth
d	Average distance from HTHH volcano
dx	Spatial grid size
d_{point}	Radial distance of a point from HTHH volcano
f	Coriolis parameter
f_b	Friction coefficient
g	Gravitational acceleration
Fr	Froude number
H	Water depth along channel axis
h	Undisturbed water depth
h_1	Water depth before the sloping section in basin with shelf bathymetry

h_2	Water depth after the sloping section in basin with shelf bathymetry
h_c	Critical water depth where $Fr = 1$
M	Discharge flux in horizontal plane along x
M_a	Molecular mass of air
m	Slope
m_a	Arbitrary positive constant
N	Discharge flux in horizontal plane along y
n	Manning's roughness coefficient
P	Amplitude of the forced wave
P_{atm}	Atmospheric pressure
Q	Amplitude of the free wave
R	Radius of the Earth
R_a	Universal gas constant
R^2	Coefficient of Determination
S	Variable cross-section of bay filled with water
S_w	Moving speed of the wind field
T	Temperature
t	Time
u	Water particle velocity in x direction
U_{w10}	Wind Speed in East-West direction at 10m elevation
V	Traveling speed of atmospheric pressure disturbance
v	Water particle velocity in y direction

V_l	Atmospheric pressure velocity in alongshore direction
V_{w10}	Wind Speed in East-West direction at 10m elevation
X	Horizontal distance along basin in East direction
x	Horizontal coordinate in zonal direction
X_d	Distance travaled by atmospheric disturbance
y	Horizontal coordinate in meridional direction
z	Cross-section function of quasi-parabolic channel
α	Density ratio
γ	Ratio of the principal specific heat capacities of the air
λ	Wavelength
ρ	Fluid Density
ω	Angular velocity of the Earth
ϕ	y-coordinate in degree
η	Water surface elevation above still water level (wave amplitude)
η_0	Water level change due to static pressure gradient
η_{max}	Maximum wave amplitude
η_{peak}	Peak amplitude of the wave
τ_d	Dispersion time parameter
τ_x , τ_y	Bottom shear stresses along x and y
ΔP	Pressure Gradient
AK	Anak Krakatau

BATNAS	Batimetri Nasional from Badan Informasi Geospasial (National Bathymetry from Geospatial Information Agency), Indonesia
BBIP	Center for Coastal Fish Breeding
BIG	Badan Informasi Geospasial (Geospatial Information Agency), Indonesia
BNTN	Ciwandan Tide Gauge Station
BPPT	Badan Pengkajian dan Penerapan Teknologi (Agency for the Assessment and Application of Technology), Indonesia
CFL	Courant-Friedrichs-Lewy
CPU	Central Processing Units
DART	Deep-ocean Assessment and Reporting of Tsunamis
DEM	Digital Elevation Model
FFT	Fast Fourier Transform
GAK	Gunung Anak Krakatau
GFZ	German Research Centre for Geosciences
GPU	Graphics Processing Units
GUI	Graphical User Interface
HTHH	Hunga Tonga-Hunga Ha'apai
InaTEWS	Indonesia Tsunami Early Warning System
KTAG	Kota Agung Tide Gauge Station
NLSW	Nonlinear Shallow Water
NZF	Name for DART buoy in New Zealand
OBU	Ocean Bottom Unit

PANJ	Pelabuhan Panjang Tide Gauge Station
PLTU	Electric Steam Power Plant
RMSE	Root Mean Square Error
SERA	Serang Tide Gauge Station
TG	Tide Gauge Station

CHAPTER 1

INTRODUCTION

Long waves are the sea surface oscillations, which typically have wave periods from 5 minutes to 12 hours, including tsunamis, seiches and storm surges (Nielsen, 2009; Toffoli&Bitner-Gregersenand, 2017). Another distinctive characteristic of sea waves can be related to the water depth over which the waves propagate. Those waves have a traveling water depth/wavelength ratio of less than 1/20, which makes them also defined as shallow-water waves. The sea is never still, and most ocean waves are generated by winds. However, more hazardous waves like tsunamis and storm surges are mostly caused by underwater displacements where a large displacement of water occurs and severe weather where strong atmospheric disturbances exist. The word "tsunami" originally refers to the Great Sanriku earthquake and the consequent long hazardous waves in 1896 in Japan, meaning "harbor wave" in Japanese. It was defined as "seismic sea waves" in other languages. Tsunamis are typically generated by large and shallow or intermediate-depth earthquakes, mostly in subduction zones, due to the sudden vertical displacement of the seafloor. The Pacific Ocean, with its Ring of Fire subduction zones, hosts more than 80% of the world's tsunamis (UNESCO IOC-ITIC, 2022). On the other hand, seiches and storm surges are caused by meteorological disturbances such as strong winds and atmospheric pressure changes, but seiches are induced by a resonance effect on enclosed or semi-enclosed basins. Therefore, tsunamis can potentially produce additional long-wave components (seiches) depending on local bathymetric conditions. The long waves generated by meteorological disturbances are also called "meteotsunamis" which were first introduced by Defant (1961) and are more commonly used in recent years. Meteotsunamis and storm surges are both generated by inverse barometric effect. However, meteotsunamis needs an abrupt change, or pulse-type in other words, in the atmospheric pressure and associated winds. Hence, the rate of change of water

level in storm surges is lower, whereas rapid oscillatory change is observed in meteotsunamis. In addition, storm surges are generated by pressure and wind systems but are more related to strong wind fields, while meteotsunamis are more to the moving pressure systems, which do not necessarily exclude winds and are combined with resonance effects and have a multi-resonant characteristic. The seismic tsunamis, seiches and meteotsunamis have similar oscillatory characteristics at the coast, with oscillation periods from few minutes to few hours depending on the local basin and shelf dimensions and sea-level oscillations lasting few hours to days. Furthermore, the impact areas of meteotsunamis could be considered local to regional in nature. However, the most recent volcanic eruption induced meteotsunami of January 15, 2022, Hunga-Tonga Hunga Ha'apai event, showed that they could affect the entire globe.

1.1 Motivation and General Description of Study

Earthquakes are the main source mechanisms of tsunamis and large tsunamigenic earthquakes, especially in the subduction zones, occur on relatively much shorter timescales. Nevertheless, destructive tsunamis are also produced by volcanic eruptions, which have been reported throughout history, threatening the coastal communities. This situation has come to the fore again with the high impact volcanic tsunamis experienced in recent years. Furthermore, while earthquake generated tsunamis have been studied immensely, there is less focus on research related to tsunamis induced by atmospheric disturbances (meteotsunamis). Consequently, this study focuses on numerical modeling of long waves (tsunamis and meteotsunamis) sourcing from those atypical origins, volcanic activities and atmospheric disturbances and investigates the complex mechanisms behind them. It can be necessary to define the atypical sources here, which are referred to as "non-mega thrust and aseismic" sources in IOC/UNESCO TOWS-WG Team reports (IOC/UNESCO TOWS-WG Team, 2020) and can be further categorized as volcanic

sources (large scale collapses, submarine explosions, and pyroclastic flows) and submarine/subaerial landslides and tsunamis from meteorological disturbances.

In the initial step, scenario-based research for the numerical modeling of the December 2018 Gunung Anak Krakatau tsunami was conducted to investigate the possible source mechanisms and their contribution to explaining the observed sea level oscillations at the coastal area in the Sunda Strait. On December 22, 2018, a destructive tsunami was generated due to the volcanic eruption of the Gunung Anak Krakatau (GAK) that caused serious damage and killed more than 400 people, as reported by the Indonesian Disaster Management Authority as of December 25, 2018 (Badan Nasional Penanggulangan Bencana, BNPB, https://bnpb.go.id/). An aerial view of GAK during the eruption is given in Figure 1.1. GAK was the result of the Krakatau volcano eruption in 1883, which is one of the largest explosive eruptions in historical time and produced one of the largest instrumentally recorded tsunami waves (Nomanbhoy and Satake 1995; Choi et al., 2003; Pelinovsky et al., 2005). The volcano is partly built on a steep wall of the caldera (Deplus et al., 1995; Paris et al., 2014), which makes a flank collapse and a tsunami highly expectable. The December 2018 Sunda Strait tsunami hit the coastal cities and had severe impacts on the western coast of Banten and the southern coast of Lampung in Sunda Strait, Indonesia. This recent event challenged the traditional understanding of tsunami hazard, warning and response mechanisms and raised the topic of volcanic tsunami hazard.

Figure 1.1 Aerial view of Gunung Anak Krakatau during December 22, 2018 eruption (Photo by N.Hidayat, retrieved from https://www.dw.com/en/anak-krakatau-volcano-erupts-spewing-ash-500-meters-high/a-53093078)

The processes leading to tsunami generation by volcanoes can simply be stated as submarine volcanic explosions, volcanic flow entries into the seawater, flank failures (collapses) or deformations (subaerial), and submarine failures (submarine landslides) which are not necessarily triggered by a volcanic eruption (Latter, 1981; Paris et al., 2014; Day, 2015; Williams et al., 2019). The most important factors affecting tsunami formation by landslides at volcanoes, which seem responsible for the wave generation in most cases, including the December 2018 event, can be expressed as the volume, thickness and velocity of the landslide in the broadest sense (Paris et al., 2014). Nevertheless, the complex mechanism of this volcanic tsunami generation still needs further investigation due to several factors. Those are the lack of immediate observations of the source in the near-field area because of the impossibility of instrumentation, the lack of large-scale data on the mechanism between landslide motion and tsunami generation and lack of observations of the governing processes in sufficient detail. Although there are a good number of modeling studies on flank failures of volcanos and resulting tsunamis (Tinti et al., 2000; Kawamata et al., 2005; Satake, 2007; Torsvik et al., 2010; Abadie et al., 2012;

Giachetti et al., 2012; Omira et al., 2016; Ioki et al., 2019), these studies need further validation since volcanic tsunami events have not been well recorded previously like the Sunda Strait event.

As Anak Krakatau is one of the potentially tsunamigenic volcanoes in the world, according to several criteria (Paris et al., 2014), the Sunda Strait region is prone to probable future collapse and associated tsunamis. Furthermore, Indonesia, the Philippines and Papua New Guinea are the Pacific countries for which tsunamis are one of the major volcanism-induced disasters (Nishimura, 2008). Therefore, understanding of the triggering/source mechanism of the December 2018 tsunami is a key step and would help to demonstrate the extent of tsunami hazard in the region. Consequently, the possible source mechanisms of this volcanogenic phenomenon and their contribution to an explanation of the observed sea level disturbances by considering the impacts of this destructive event were investigated in the first part of this study. A flank collapse (partial destabilization of the volcano) scenario was suggested appearing capable of generating the observed tsunami along the coast of the affected area, Sunda Strait. Coupling of a two-layer landslide model and a hydrodynamic model was performed to test the ability of such an implementation to reproduce a large scale current volcanic eruption induced tsunami via post-tsunami field survey observations and tide gauge record comparisons.

In the second part of the study, the long wave generation and amplification due to moving atmospheric disturbances were investigated. The atmospheric perturbations act on the water surface and generate free and forced waves, which are amplified due to the resonance and shoaling. Meteotsunami generation generally requires large-scale atmospheric systems, including intense atmospheric pressure gradients and strong wind fields. However, several small-scale atmospheric perturbations can also be found in unstable atmospheric layers, which is given as ‘‘tumultuous atmosphere’’ in Šepić et al. (2015) and lead to meteotsunami generation under favorable synoptic conditions. Meteotsunami waves are observed during meteorological events such as thunderstorms, squall lines, frontal passages, and pressure jumps. However, it is not always a severe weather condition that

meteotsunami events occur. Those hazardous waves, being observed at different locations of the world oceans, often have local names such as “Rissaga” (Balearic Islands), “Marubbio” (Sicily), “Milghuba” (Malta), “Abiki” (Nagasaki Bay) and “Seebär” (Baltic Sea) (Monserrat and Rabinovich, 2006).

The pioneering research on this subject dates back to Honda et al. (1908), who overviewed the nonseismic long period oscillations in Japan’s harbors and bays. The term “meteorological tsunami” was most probably suggested by Nomitsu (1935) for the first time for the atmospherically generated long waves on the Japanese coast, indicating their similarity to the regular (seismic) tsunamis. However, the subject is still relatively young as the essential characteristics to distinguish those waves are emerging and it still has a lot to be discovered. The tsunami catalogs include numerous “tsunami-like” events of “unknown origin,” which may be, in fact, meteotsunamis (Monserrat et al., 2006). Until recent years, there were still discussions on the term to define those meteorologically induced tsunami-like waves as some proposed “Rissaga” and “meteotsunami” in the scientific community. However, the key features of those events are emerging as the new studies analyzing previous meteotsunami events increase and the community seems to have agreed on the term “meteotsunami”. Still, the phenomenon is considered as a rare and underrated hazard (Pattiaratchi and Wijeratne, 2015; Rabinovich, 2020).

Numerical modeling is an essential part of conducting meteotsunami research, may be more than many other related subjects, as it is almost impossible to reproduce the phenomena in a physical environment. All the available studies are based on either analysis of previous examples or numerical modeling of certain cases. Despite the promising state-of-the-art modeling work containing detailed analysis of the wave generation and amplification mechanisms remain limited in this large area of research. Climate change also has an impact on the changing characteristics of the atmospheric systems. Although there is a long way to reach a conclusion on the role of climate change on such events, some regional and global climate models expect an increase in their frequency and intensity (Walsh et al., 2004; Walsh et al., 2012; Walsh et al., 2019; Knutson et al., 2010) which recalls the expectation in the

Mediterranean or Black Sea (Gaertner et al., 2007), where their coastal areas have already been indicated as “meteotsunami-favorable areas” in Sepic et al. (2015). Therefore, developing a robust modeling infrastructure to solve long waves due to atmospheric disturbances with a particular focus on the amplification mechanisms is another primary objective of this study.

In the final part, the study focused on the violent eruption of the Hunga Tonga-Hunga Ha’apai (HTHH) volcano (20.546°S, 175.390°W) and the consequent tsunami observed globally due to an unusual source: air pressure disturbances. The eruption occurred on January 15, 2022, at 04:15 UTC (USGS, 2022), following prior volcanic activity, and generated a large tsunami that caused serious damage in many of the Tonga Islands, killing three people and struck far-off shores across the ocean. Waves up to 15 meters were reported locally, destroying the west coast of the Tongatapu Island and highly impacting the surrounding Tonga islands (Government of Tonga, 2022). More than 1-meter waves were recorded at several coastal gauges in the Pacific basin (New Zealand, Japan, Hawaii, Mexico, Chile, and the US west coast), up to 1.2 m in Japan and 2 m in Mexico specifically. Damaging waves reaching Peru also caused two deaths; where additionally, an environmentally catastrophic oil spill occurred near the Ventanilla district to the north of the Lima metropolitan region and destroyed the marine ecosystem.

On the other hand, the explosion of HTHH with the volcanic explosivity index of (VEI) 6 generated an ash plume and the ashfall reached Tonga (particularly Tongatapu Island) and the islands of Vatoa and Ono-i-Lau in Fiji. The preliminary estimations for the explosive energy give 4 to 18 megatons of TNT (NASA, 2022), with an equivalent magnitude of 5.8 earthquake as reported by the USGS. The atmosphere was blasted out of the way as a shockwave emanated from the island, radiating outward at close to the speed of sound. Then, the shockwave formed in the immediate vicinity of the explosion reached a stable state after ~5 km traveling (Lynett et al. 2022). Those air waves formed in the mid-stratosphere (more than 20 km) circled Earth for days as a positive pressure pulse generating particular conditions over the oceans that potentiate the generation of a tsunami, in this case,

called a volcanic origin atmospheric pressure induced tsunami. The atmospheric pressure waves were measured on barometers as they traversed the globe and the consequent ocean waves were observed in the Pacific, on coastal gauges in the Caribbean, across the Atlantic and in the Mediterranean as well.

HTHH is only one of the submarine/subaerial volcanos in Tonga, a part of the arc of volcanoes of the "Ring of Fire", which can produce even more hazardous eruptions; the threat is not over. In fact, a large tsunami inundated large areas of Tongatapu island in the mid-15th century with runup heights up to 30 m, and the Tu'i Tonga kingdom was severely impacted by this event, where the source of the tsunami was hypothesized as a caldera-forming eruption that would have caused the total collapse of an ancient island volcano, probably located along the Tonga ridge less than 150 km southwest off Tongatapu (Lavigne et al., 2021). This unique event needs to be understood in detail from many aspects and people from different disciplines have a lot to learn from this significant experience. The December 2018 Gunung Anak Krakatau eruption and the consequent tsunami had already driven the international tsunami community on volcanic tsunamis and raised the topic of tsunamis from atypical sources.

The Pacific Tsunami Warning System responded to a tsunami from an atypical source for the first time and has had considerable difficulties in addressing the operational requirements within the desirable timeframe. The urgent need for preparedness against the volcanic tsunami hazard is indisputable. We must better understand the complex mechanisms behind this unique and considerably rare, once-in-a-century event, which to be prepared for the unexpected. Furthermore, the January 2022 event has been one of the most instrumentally recorded tsunami events on a global scale, bringing a considerable amount of high-quality data. Several volcanogenic tsunami events occurred previously throughout the world's oceans, most of which could not be recorded/observed adequately (Paris et al. 2014). Therefore, this event provides a unique test for modeling studies, which the early warning systems, mitigation strategies and preparedness are gravitating around. Beyond these, this event reminded the huge computational cost, which stands as a

barrier to solving such a global scale tsunami by using atmospheric models, which even work at subkm-scale or 3D compressible flow models. The need for the development of alternative modeling approaches based on reasonable assumptions to explain the air-sea coupling and the consequent tsunami via atmospheric forcing and resonance mechanisms was the motivation behind this part of the thesis study.

Chapter 2 provides a thorough literature review of tsunamis from atypical sources, their generation mechanisms and available numerical modeling approaches, structured in three parts for the volcanic activities, atmospheric disturbances and the volcanic origin atmospheric pressure induced tsunamis. Chapter 3 presents the modeling of tsunamis from volcanic origin, an implementation of the December 22, 2018 Gunung Anak Krakatau tsunami in the Sunda Strait, Indonesia. This part of the study is previously presented in Dogan et al. (2021a). In Chapter 4, the long wave generation and amplification due to traveling atmospheric disturbances are given by introducing the numerical model, verification of the model and numerical tests performed in different types of basins. This part of the study is previously presented in Dogan et al. (2021b). The final part of the study is presented in Chapter 5, covering the modeling efforts to solve the global propagation of air pressure waves and the consequent sea waves due to the January 15, 2022 HTHH volcanic eruption. This part of the study has been submitted for publication (Dogan et al., 2022).

CHAPTER 2

LITERATURE REVIEW

2.1 Tsunamis due to Volcanic Activities

Several volcanic tsunami events occurred previously throughout the world oceans, most of which could not be recorded/observed adequately (Paris et al. 2014). Some remarkable examples are the eruption of Santorini (1628 BC) in the Aegean Sea (Pararas-Carayannis, 1992; Cita and Aloisi, 2000; Dominey-Howes, 2004; Bruins et al., 2008), the lateral collapse of Oshima-Oshima volcano (AD 1741) in Japan Sea (Satake and Kato, 2001; Kawamate et al., 2005; Satake, 2007), large pyroclastic flows from Mount Tambora (AD 1815) in Indonesia (Wood, 2014; Murphy, 2019) and the lateral collapse of Ritter Island (AD 1888) in the Bismarck Sea in Papua New Guinea (Karstens et al., 2019; Ward and Day, 2003). Except for these historical events, Karymsky in the Kamchatka Peninsula, Russia, in 1996 (Belousov and Belousova, 2001; Torsvik et al., 2010), Stromboli in Italy, in 2002 (Bonaccorso et al., 2003; La Rocca et al., 2004; Tinti et al., 2006), and Soufrière Hills, Montserrat in 2003 (Pelinovsky et al., 2004) are few well-reported events as yet.

The western Pacific basin is where the vast majority of volcanic tsunamis occur and most notably in Southeast Asia, the Caribbean, and the Mediterranean basins. A preliminary list of 50 possibly tsunamigenic volcanoes from around the world can be found in the "Report by IOC/UNESCO TOWS-WG Team on Atypical Tsunami Sources" with their classification according to the tsunami triggering mechanisms (IOC/UNESCO TOWS-WG Team, 2022). Some remarkable ones in the Indian Ocean Basin are Barren Islands in India (explosive activity or flank collapse), Piton de la Fournaise in Reunion Island, France (flank collapse), and Anak Krakatau in Indonesia (flank collapse, pyroclastic flows and tsunami from generated pressure disturbance). In the North and South Atlantic Basins, the probability of a volcanic

tsunami is indicated as low with events with very low recurrence, i.e., no documented volcanic tsunami in the last three centuries in the South Atlantic Basin. In the Caribbean, Soufrière Hills in Montserrat (pyroclastic flows), Mount Pelée in Martinique (pyroclastic flows and debris flows), Kick'em Jenny in Grenada (submarine explosions and flank instability) and Soufrière in St. Vincent (pyroclastic flows) can be listed as some of the important ones with tsunami history. The tsunamigenic volcanoes in the Mediterranean can also be given as Vulcano in Italy, which has been in an unrest state in the recent years, Stromboli in Italy, which is also a very active volcano (landslides and pyroclastic flows), Kolumbo in Greece, which is an active submarine volcano (explosive activity) and Santorini in Greece with historical explosive eruptions.

2.1.1 Generation Mechanisms

A thorough review of the tsunami triggering mechanisms related to volcanic activities can be found in Paris et al. (2014) and Paris (2015). The primary mechanisms at work when a volcanic eruption produces a tsunami (Figure 2.1) could be listed based on available data from past events (40 events between 1550–2007): i) submarine explosions, ii) pyroclastic flows, iii) earthquakes before or during the eruption, iv) flank failures, v) caldera collapse (leading to rapid subsidence of the sea floor), and vi) collapse of the coastal lava bench. Additionally, atmospheric disturbances (shock waves or Lamb-type air pressure waves) created by large explosions can also cause tsunamis by dynamic coupling of the air pressure and the sea surface, as for meteotsunamis and as observed in the 1883 Krakatau and 2022 Tonga volcanic eruptions. According to documented cases of volcanic tsunamis, shock waves, lahars, and lava bench failures are unlikely to produce tsunamis with wave heights more than 3 m. The only source mechanisms that are likely to demonstrate volumes greater than 1 km^3 are pyroclastic flows, flank failures, and caldera collapse. Latter (1981) also states that the tsunamis caused by the pyroclastic flows and landslides induced by volcanic activity are particularly hazardous. A

summary of the information on the source mechanisms of volcanic tsunamis is given in Table 2.1, whereas a general sketch for those mechanisms is presented in Figure 2.1.

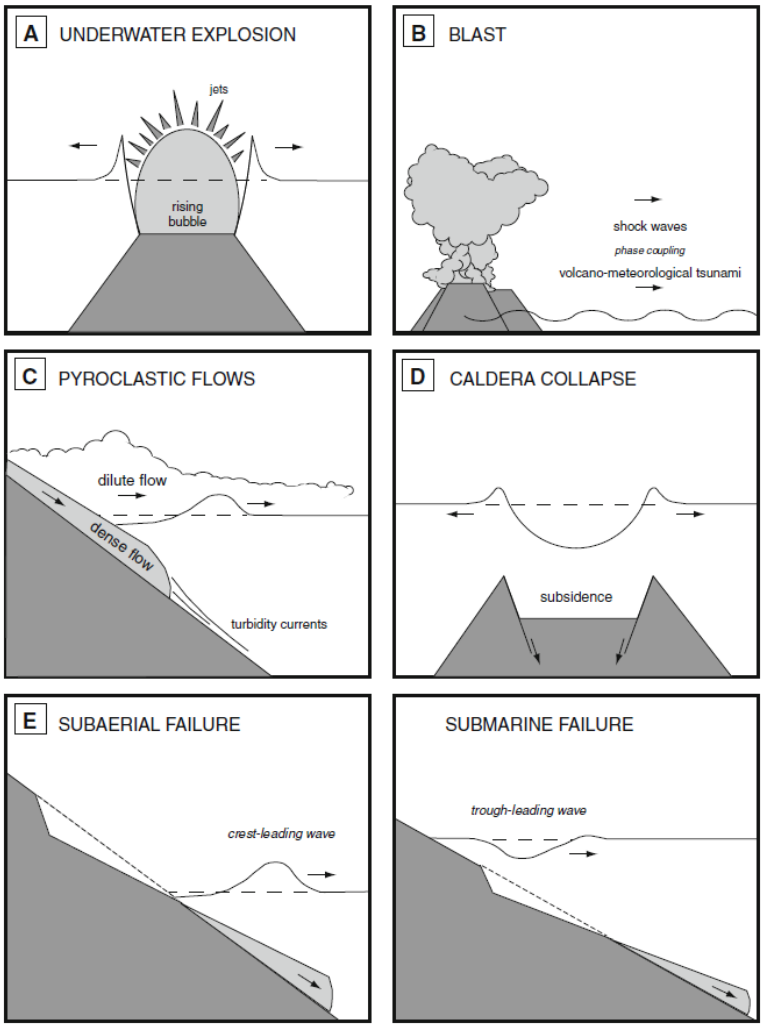

Figure 2.1 General sketch showing the main source mechanisms of volcanic tsunamis (retrieved from Paris et al., 2014)

Table 2.1 Useful information for the source mechanisms of volcanic tsunamis (Modified from Paris et al., 2014)

Source Mechanisms	% of Events	Source Volume (km^3)	Volume Flux (m^3/s)	Wave Height at shoreline (m)	Travel Distance (km)
Underwater explosion	25	<1	$<10^9$	<10	<200
Pyroclastic flow	20	1-200	10^5-10^8	<30	<300
Earthquake	<20			<15	<500
Flank failure	15	1-500	10^5-10^6	<100?	<6000
Caldera subsidence	10	1-100		<20	<200
Air wave	5			<3	>1000
Collapse of lava bench	<1	<0.01	$<10^6$	<2	<10

2.1.2 Numerical Modeling

It is possible to simulate tsunami propagation using depth-averaged models, nonlinear shallow-water equations, or Boussinesq-type equations in the case of tsunamis driven by slope instability or volcanic activity (Yavari-Ramshe & Ataie-Ashtiani, 2016; Fritz et al., 2004; Watts et al., 2003). It is advised to employ weakly dispersive depth-averaged models (Boussinesq type) or completely dispersive three-dimensional models (e.g., Reynolds-averaged, Navier-Stokes models) as those tsunamis are typically characterized by intermediate to deep-water waves with shorter wavelengths than seismic tsunamis. However, the choice of the model is case specific as tsunamis from atypical sources can have different configurations (subaerial and/or submarine) and different types of motions (slow or rapid). Different rheologies can also play a role in modeling. Here the important points are how to approach the source in terms of geometry and duration and the use of sufficient grid dimensions. On the other hand, complex models, including dispersive and coupled flow-water approaches, imply high computational costs. Thus, the goals that must be achieved largely determine the modeling technique.

A couple of numerical modeling studies after the December 2018 GAK tsunami was presented. Some of them used sophisticated models, including the dispersion effect, 3D approach with σ-layers, and different rheology (Grilli et al., 2019). Some applied rather simpler models by following a multilayer approach and somehow defining rheology with different methods but employing the NLSW equations (Omira and Ramalho, 2020; Paris et al., 2020). Some only considered initial estimates for the landslide source dimensions and inputted them as a static source in which the landslide generation phase (i.e., the interaction between the landslide material and the sea water) was ignored (Heidarzadeh et al., 2020a). All mentioned studies achieved satisfactory modeling results to a certain extent. Furthermore, it is important to note that several past events were satisfactorily reproduced by implementing nonlinear shallow water equations, such as the 1883 Krakatau tsunami in the Sunda Strait in Indonesia (Nomanbhoy and Satake, 1995; Giachetti et al., 2012), and the 1741 Oshima-Oshima tsunami in Japan Sea (Satake, 2007; Ioki et al., 2019).

2.2 Tsunamis due to Atmospheric Disturbances

Long sea waves sourcing from meteorological disturbances, which are called as meteotsunamis, have been observed globally and discussed in many studies; USA East Coast (Churchill et al., 1995; Sallenger et al., 1995; Pasquet and Vilibić, 2013; Lipa et al., 2014), Gulf of Mexico (Paxton and Sobien, 1998), The Great Lakes (Ewing et al.,1954; Donn, 1959; Bechle and Wu, 2014), Atlantic Ocean (Mercer, 2002; Candella, 2009; Dragani et al., 2009), Adriatic Sea (Vučetić et al., 2009; Šepić et al., 2012), Mediterranean (Airy, 1878; Monserrat et al., 1991; Rabinovich and Monserrat, 1996; Vilibić et al., 2008), the Aegean Sea (Papadopoulos, 1993), Black Sea (Vilibić et al., 2010), East China Sea (Hibiya and Kajiura, 1982; Tanaka, 2010), Sea of Japan (Park, 1986) and Yellow Sea (Wang et al., 1987; Cho et al., 2013). Moreover, Pattiaratchi and Wijeratne (2015) listed 35 meteotsunami events around the world with the highest two observed wave heights: 5 m in the Balearic Islands

and 4.8 m in Nagasaki Bay in Japan. Kânoğlu et al. (2020) also mentioned one of the most destructive meteotsunami events, the March 19, 2017 Dayyer event in the Persian Gulf. The event was analyzed in detail by Heidarzadeh et al. (2020b) and was found to be local but high impact on the coast of Dayyer due to the active atmospheric processes during March 18-22, 2017. More recently, Rabinovich (2020) overviewed 51 known events since 1992 to analyze the origin of waves and their correlation to atmospheric disturbances. He categorized the analyzed meteotsunami events based on the weather conditions (good or bad) and the bathymetric/topographic features at their impact location (open coast or harbor-type). He further indicates five "hot" regions of meteotsunamis as the Mediterranean (especially the Adriatic Sea and the Balearic Islands), the Yellow Sea and the East China Sea, Unites States East Coast, the Gulf of Mexico, and the Great Lakes. He emphasizes the "calm and sunny" weather conditions surprisingly reported during some meteotsunami events as one would expect severe weather in such events. The reason behind this is the synoptic conditions (small-scale but intense atmospheric disturbances) which occur in high altitude layers of the atmosphere but result in meteotsunamis due to resonant effects. Therefore, the atmospheric system does not always necessitate extreme weather conditions or strong forcing but the resonance effects.

2.2.1 Generation and Amplification Mechanisms

General characteristics of meteotsunamis are similar to those of tsunamis of tectonic or landslide origin. They have similar spatial scales to landslide tsunamis due to being local events, whereas temporal scales of several minutes to hours are common for all of them. These tsunami waves may cause devastating destructions in the coastal zone (Monserrat et al., 2006). The difference is in the mechanisms of their generation. For meteotsunamis, sources are spatial and temporal pressure distributions, atmospheric gravity waves and squall lines (Rabinovich, 2020). However, in order to be noticeable, meteotsunamis require amplification as the

equilibrium response to atmospheric pressure variations (inverted barometer principle) can only generate a few centimeters of water level change (Romero et al., 2019). Figure 2.2 depicts the meteotsunami generation processes in general terms.

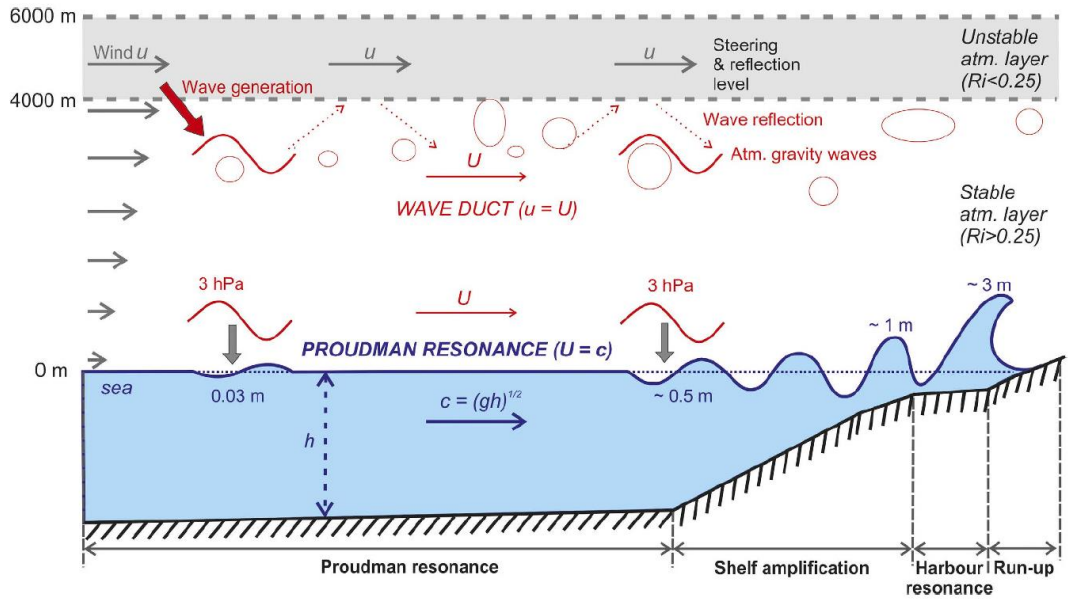

Figure 2.2 Schematic representation of meteotsunami generation processes (retrieved from Šepić et al., 2015)

There have been several studies focused on the mechanisms of meteotsunami generation and propagation. Some researchers also used analytical and numerical models to analyze the mechanism of ocean wave generation by atmospheric pressure disturbances under idealized conditions. Vilibić (2008) simulated the Proudman resonance caused by sinusoidal air pressure disturbances. He also discussed the similarities between meteotsunamis and landslide tsunamis as both mechanisms generate forced waves and free waves, which then propagate along the ocean surface. A series of analytical studies on the trap and refraction of ocean waves induced by moving atmospheric pressure over a step bottom and continental shelf were conducted by Vennell (2007, 2010), Thiebaut and Vennell (2011), and Melinand (2015). Niu and Zhou (2015) studied the shape of water surface oscillations under a moving low-pressure system with different speeds by adopting a nonlinear shallow water model. They used a moving low pressure with Gaussian distribution in an

unbounded flat-bottom water area and analyzed the effects of speed, central pressure drop and spatial scales on the water elevation. Choi and Seo (2017) investigated the ocean waves induced by a low-pressure system moving over a slope towards shore based on an idealized problem from the landing process of a typhoon or a hurricane. They also investigated the runup and development of edge wave patterns generated by a moving circular shape atmospheric pressure disturbance across a straight shoreline on a sloping beach. A Gaussian shape pressure drop of 20 hPa was used at the center in the circular area of a 200 km radius. Various speeds of pressure disturbance were selected up to 50 m/s and tested. The change in the maximum runup was presented according to different moving speeds for the given atmospheric pressure disturbance. While wave runup and rundown were repeated at the shoreline, the generation and propagation of edge waves in the alongshore direction due to wave refraction were also observed.

Chen and Niu (2018) focused on the generation and propagation of forced waves due to a circular shape atmospheric pressure drop moving over a constant shore slope. They numerically investigated the formation of Proudman resonance when the moving pressure disturbance speed is close to the wave celerity while the disturbance moves over a slope towards the shore. The wave pattern starts as a concentric-circle type but develops to a triangular type with increasing Froude number on the slope. Froude number can be defined as $Fr = V/c$; the ratio of the atmospheric pressure speed, V, to the celerity of long ocean waves $c = \sqrt{gh}$, where g is the gravitational acceleration and h is the water depth. They discussed the characteristic parameters of the circular pressure disturbances and slope gradient affecting the wave pattern. Their findings demonstrated that the significant peak of the maximum water elevation can be produced by a pressure disturbance with small spatial scale and high moving velocity over a milder slope, which is not always possible to be observed prior to the landing of the pressure disturbance. An extremely high runup was observed when the forced wave reached the shore. They further indicated a "hysteresis effect," which refers to the peaks not occurring at the time of Proudman resonance condition is achieved ($Fr = 1$) but rather later (at about $Fr = 1.45$). In

another recent study, Niu and Chen (2020) investigated the energy accumulation during the growth of the forced wave due to a circular Gaussian shape pressure disturbance and attempted to quantify the time required to excite the forced wave by introducing a parameter, namely response time. The forced wave induced by the pressure disturbance gradually grows and finally reaches a quasi-steady state. However, the response time and the energy accumulation are highly related to the Froude number and the effects of the bottom friction and nonlinearity are only significant when Fr is close to 1.

Mercer et al. (2002), Niu and Zhou (2015), Chen and Niu (2018), and Sun and Niu (2021) considered a circular pressure drop for the atmospheric forcing in their modeling studies, whereas Vilibic (2008) and Williams et al. (2021) used sinusoidal pressure signals, showing band-shape characteristic with certain widths (wavelength of the atmospheric forcing). A summary of the used pressure forcing characteristics available in those studies is presented in Table 2.2. The meteotsunami-generating atmospheric systems, including moving pressure and wind fields, can show such a band-shape characteristic with pressure drop and certain wavelengths, as observed in several previous meteotsunami events (Monserrat et al., 1991; Vilibic et al., 2004; Rabinovich, 2020; Kim et al., 2021; Kim et al., 2022). Furthermore, the available studies mostly focus on constant depth basins or a uniform constant slope towards the shore or are based on specific case studies. Therefore, in the second part of this study (Chapter 4), a pressure drop with a broad range of different traveling speeds is considered traveling over basins with shelf bathymetries with different shelf slopes as closer to the real situation in most of the basins, in addition to the flat bottom and triangular cross-section basins which were employed for the model verification. Mercer et al. (2002) highlighted the reflection and refraction processes that take place over the continental slopes during the propagation of the generated ocean waves, especially as the primary cause of the unusual sea level observations on the Newfoundland coast of Canada during Tropical Storms Jose and Helene. In addition, the average moving speed of the atmospheric pressure is in the range of 13-40 m/s, according to the analysis of significant meteotsunami events between 1992 and 2019

in Rabinovich (2020). Therefore, the considered average moving speeds for the atmospheric forcing are 7 to 44 m/s in this study.

Table 2.2 Summary of atmospheric forcing and basin characteristics used in available studies

Source	**Pressure forcing characteristic**				**Basin characteristic**
	Shape	**ΔP**	**Spatial Scale**	**Average moving speed**	
Mercer et al. (2002)	Circular drop	30 hPa	Radius, 40 km	≈30 m/s	Real bathymetry of Newfoundland, Canada
Niu and Zhou (2015)	Circular drop	2-200 hPa	4-40 km	9.9 m/s	Constant depth of 10 m
Chen and Niu (2018)	Circular drop	20 hPa	2-20 km	9.9-44.3 m/s	Uniform shore slope 1:400 – 1:1000
Sun and Niu (2021)	Circular drop	1 hPa	3 km		
Vilibic (2008)	Band-shape sinusoidal pressure signal	1 hPa	13.3-79.7 km	22.15 m/s	Constant depths of 10 m – 200m
Williams et al. (2021	Band-shape sinusoidal pressure signal	1 hPa	40 km	22.15 ± 2 m/s and variable forcing speed	Constant depth of 50 m ± 4 m and 2 different uniform slopes (one steep and one shallow)
This study	Band-shape	20 hPa	10-40 km	7 – 44.3 m/s	Constant depth of 200 m, triangular cross-section, shelf

	pressure drop	bathymetry from 200 m to 20 m depth with slopes 1:10 – 1:700

In addition to the atmospheric pressure variations, strong winds also have a significant role in meteotsunami generation. In the Derecho of June 29–30, 2012, in the Great Lakes, Chesapeake Bay, and on the Atlantic coast of the USA, energetic winds played the main role in seiche formation in the impacted bays (Vilibic et al., 2014). Although the atmospheric pressure disturbances are the most important for the Atlantic coast, and the combined effect of pressure oscillations and wind is considered responsible for pronounced events in the Great Lakes.

2.2.2 Numerical Modeling

Many meteotsunami events were reproduced by numerical modeling with different degrees of accuracy (Rabinovich et al., 1999; Liu et al., 2003a; Vilibić et al., 2004; Dragani, 2007; Vilibić et al., 2008; Orlić et al., 2010; Tanaka, 2010; An et al., 2012; Bechle and Wu, 2014; Šepić et al., 2018; Heidarzadeh et al., 2020b). Romero et al. (2019) claim that as long as the atmospheric coupling and resonant mechanisms are taken into consideration, a shallow water model can be sufficient to explain the dynamics and amplification of long ocean waves. Some of the research on meteotsunami modeling uses available numerical ocean models that utilize Navier-Stokes equations with hydrostatic and Boussinesq approximations. Romero et al. (2019) used shallow water equations with the atmospheric forcing term, and they included a drag force in the momentum equation to integrate bottom roughness and seabed frictional resistance. Šepić et al. (2018) used an ocean model solving depth-integrated shallow water equations with Coriolis term and all nonlinear terms excluding the bottom friction to simulate the 2014 Odessa meteotsunami. In their code, differently from other models, which mostly employ the spatial gradient of the

pressure disturbance in the momentum equations, the time derivative of air pressure is inserted into the continuity equation. They also indicated the insignificance of the Coriolis effect on meteotsunami/tsunami time scale and the effect of linearity/nonlinearity on wave heights up to 1-2 m as ascertained from Kowalik et al. (2012).

Bubalo et al. (2018) simulated Chrystal and Proudman resonance effects in a closed rectangular basin with two finite element models (ADCIRC and SCHISM) and one finite difference (ROMS) ocean model. They stated that even though all three models solve the same equations with similar approximations, there is a substantial difference in the time-stepping integration technique between them and the Courant-Friedrichs-Levy (CFL) condition becomes important when these models are used to describe Proudman resonance as accurately as possible. They conclude that the errors that may arise from choosing an inadequate integration time step for all areas of the grid may be very significant and affect the quality of the results of Proudman resonance in the open sea, which will, therefore, affect the reproduction in coastal areas. Bubalo et al. (2019) attempted to improve the numerical simulations by including the flooding and drying option of a finite element model (ADCIRC) for Adriatic since many of the previous studies either had cut-off depths set at several meters or did not utilize flooding and drying option. They also stated that flooding and drying are not frequently used in meteotsunami studies, contrary to storm surge and tsunami research. They showed that the inclusion of flooding and drying leads to a much more accurate reproduction of the event and grid refinement is very important as well. They recommend the use of a flooding and drying algorithm for modeling meteotsunami events.

Denamiel et al. (2019) discussed the challenges in meteotsunami modeling, stating that resolution and bathymetry used in ocean models, as well as meteorological forcing, are not sufficient to accurately reproduce the generation, propagation, and amplification of these events. Following the experiences of many researchers (Monserrat et al., 2006; Tanaka, 2010; Horvath and Vilibić, 2014), they concluded that while the main challenge is reproducing the atmospheric physics responsible for

creating the atmospheric disturbances, the development of reliable atmospheric-ocean coupled models for the short-term forecast is also important. They recommended a temporal resolution of one minute for the atmospheric forcing to be imposed on an ocean model to capture the speed and amplitude of pressure disturbances and the offshore meteotsunami dynamics as well. The spatial resolution should also be sufficiently fine to allow for an accurate representation of the continental shelf. However, Denamiel et al. (2019) concluded that the lack of precise bathymetric data and the spatial resolution limit the accuracy of the present state-of-the-art hydrodynamic numerical models to represent the ocean and complex geomorphology of the coast; primary factors affecting the meteotsunami generation and amplification (Proudman and topographic resonances). Their discussion further continued with the operation of a regional meteotsunami system developed for the Adriatic region and aims to work in real-time for early warning and forecasting purposes. Given the overwhelming limitations, the AdriSC Meteotsunami Forecast component shows skills in fair reproduction of meteotsunami events, which might be used for operational forecasting.

2.3 Volcanic Origin Atmospheric Pressure Induced Tsunamis

Long-period ocean waves are generated by coupling with the barometric perturbations in the atmosphere, requiring certain conditions in case of a volcanic explosion. It requires high explosive energy to create free waves in the atmosphere and long traveling distances over the sea for sufficient energy transfer from the air to water (Ewing and Press, 1953; Yokoyama, 1987; Rabinovich and Monserrat, 1996). The discussion of Yokoyama (1987) on the 1883 Krakatau eruption, which generated a transoceanic tsunami, showed that the observed waves in the Sunda Strait could be explained by a usual tsunami source but not the air-sea coupled waves due to the shallowness of the area. He also highlighted the large explosive energy in the 1883 Krakatau event, confirming the air wave generation. Such atmospheric waves were also recorded during the 1956 eruption of the Bezymianny volcano,

Kamchatka (Soloviev, 1974). The atmospheric induced tsunamis of volcanic origin are mainly characterized by the earlier arrival of the tsunami, then predicted based on hydrodynamic theory (Ewing and Press, 1955; Pelinovsky et al., 2005). Similar effects were observed during the 1883 Krakatau eruption (Garrett, 1970; Harkrider and Press, 1967; Pelinovsky et al., 2005), the c. AD 200 Taupo eruption, New Zealand (Lowe and De Lange, 2000; Paris, 2015) and probably the devastating eruption of Santorini, Greece (1650 BC), as Kusky (2022) speculated.

2.4 Importance of Post-tsunami Field Surveys

Post-tsunami field surveys are an essential component of tsunami mitigation as they provide invaluable data collected after a tsunami showing the tsunami's scientific, economic, and social impact on affected coasts and communities. The data is mostly perishable and therefore has to be collected immediately after the tsunami and documented in a standardized procedure (UNESCO-ITST, 2014). The post-tsunami observations collected by teams of tsunami scientists should also be reported to both the decision-makers and the public to support an efficient post-event emergency response and recovery efforts. In addition, the post-tsunami field surveys are significant in documenting the regional effects of a tsunami which highly differ from location to location. The field measurements further provide key information for future preparedness, including improvement of numerical modeling, forecasting, warning systems and engineered structures. The data collected from field reconnaissances provide a basis for modeling studies as instrumental records are mostly limited. In this regard, reconnaissance studies after some remarkable recent tsunami events, which the author contributed are summarized here. Post-event field surveys immediately after the July 20, 2017 Bodrum-Kos tsunami were conducted in coastal zones impacted by the tsunami, i.e., the coastlines of Bodrum Peninsula, Karaada Islet and Akyaka Town in Gokova Bay, Turkey, and eastern Kos Island, Greece. The survey data and field observations are presented in Dogan et al. (2019) and present significant impact data of a low-moderate tsunami in the eastern Aegean

Sea experienced after more than 50 years. Another post-tsunami field survey was performed after the September 28, 2018, Palu tsunami in Sulawesi Island of Indonesia by the UNESCO international tsunami survey team along the 125 km of coastline of the Palu Bay. The coastal observations, eyewitness interviews and tsunami runup and flow depth measurements are presented in Omira et al. (2019). Moreover, the October 30, 2020 Samos-Izmir, Aegean Sea tsunami highly impacted the coast of Izmir in Kusadasi Bay, Turkey and the northern coast of Samos Island, Greece, although it was a moderate event. National teams performed two post-tsunami field surveys on 31 October to 1 November 2020, and 4–6 November 2020, along the Turkish coastline, focusing on a ~110-km-long coastline extending from Alacati (Cesme District of Izmir) to Gumuldur (Menderes District of Izmir). The findings of the reconnaissances provide insights into the coastal impact of local tsunamis in the Aegean Sea and constitute a basis for the modeling and hazard assessment studies in the region, presented in Dogan et al. (2021c). The field observations in Samos Island from the Greek survey teams are also given in Kalligeris et al. 2021 and Triantafyllou et al. 2021, showing the overall impact of the most recent, October 30, 2020 Aegean Sea tsunami along the affected coastlines.

CHAPTER 3

MODELING OF TSUNAMIS FROM VOLCANIC ORIGIN: NUMERICAL ASSESSMENT OF 2018 GUNUNG ANAK KRAKATAU TSUNAMI

Here, the study was conducted by numerical modeling of possible configurations and scenarios of the source of the December 22, 2018 Sunda Strait tsunami based on a careful evaluation of the available post-event field survey observations, tide gauge measurements as well as published geological studies and satellite images (before and after the event). A flank collapse scenario was hypothesized with a volume of 0.25 km^3 as a combination of submarine and subaerial mass movement. Furthermore, a bathymetric dataset through pre- and post-event analyses was employed, indicating submarine slope failures in the southwestern proximity of Gunung Anak Krakatau (GAK). Hence, additional two alternatives of elliptical landslide sources on the slopes of the bathymetry change area (could be triggered by seismic motion/volcanic eruption) were considered, showing the possible effects of the tsunami that might be generated by these submarine landslides.

TWO-LAYER numerical code, which solves the nonlinear form of the long-wave equations simultaneously within two interfacing layers, was used to simulate the tsunami generation by submarine/subaerial landslide. The tsunami propagation and inundation were then simulated by the NAMI DANCE model in GPU (Graphics Processing Unit) environment by using the distribution of water surface elevations and discharge fluxes at a certain time after the slide generation computed by TWO LAYER model. The performance of the modeling approach was tested to reproduce a large scale current volcanic eruption induced tsunami via post-tsunami field survey observations and tide gauge record comparisons, which provides considerable contribution to further hazard assessment. As flank failure (lateral collapse) is one of the tsunami generation mechanisms due to volcanic eruptions, this part of the study

also helps to elucidate not only the Gunung Anak Krakatau volcanic tsunami hazard but also other possible future volcanic eruptions, also from other volcanoes, in the region (Dogan et al. 2021a).

3.1 Summary of Field Survey Observations

Several post-event field surveys were conducted along the Sunda Strait coast by different Indonesian and international survey teams in collaboration with the experts from Indonesian authorities. The information gathered from these field survey observations establishes a good base for the numerical modeling part of this study and has been summarized in the following. Published field data from Muhari et al. (2019), Syamsidik et al. (2019), Takabatake et al. (2019), and the rapid field survey data by the Indonesian national survey team, four members of which collaborated within this study were used for the comparisons. Other field surveys of the Anak Krakatau volcano tsunami were also conducted by Borrero et al. (2020) and Heidarzadeh et al. (2020c), which are summarized below but can be referred to for further information.

Between 28-30 December 2018, a field survey was performed by a team of Indonesian national experts along the western coast of Java Island. The team measured flow depth and inundation distances in the area and acquired eyewitness observations of the event. Their survey results indicated that the Center for Coastal Fish Breeding (BBIP) in Cigorondong (Figure 3.1) experienced up to four tsunami waves most probably associated with the reflection phenomenon from Paraja Bay (Figure 3.2) with a flow depth of more than 4 m. They deduced that the role of coastal protection structures (breakwaters, seawalls, and embankments) was quite significant in reducing the impact of the tsunami. The orientation, morphology and geometry of the coast towards the direction of the tsunami also influenced the impact and consequent damage. Figure 3.1 presents the summary of this field survey results with photos from some of the survey locations.

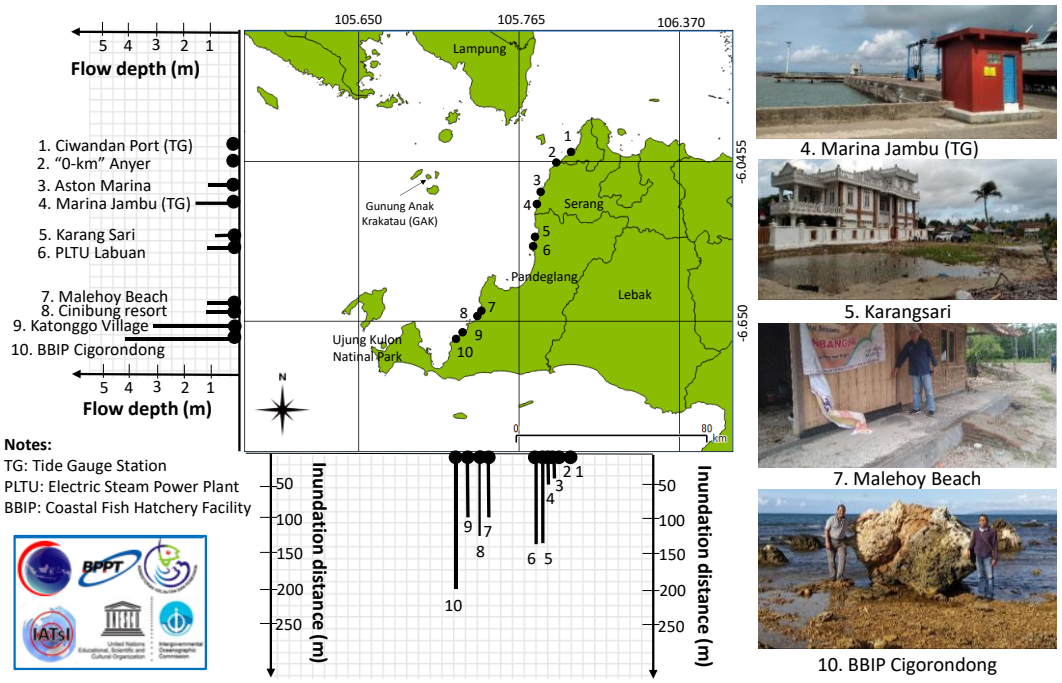

Figure 3.1 Summary of 28-30 December 2018 Indonesian national post-tsunami field survey results of Sunda Strait event along the West Coast of Java Island

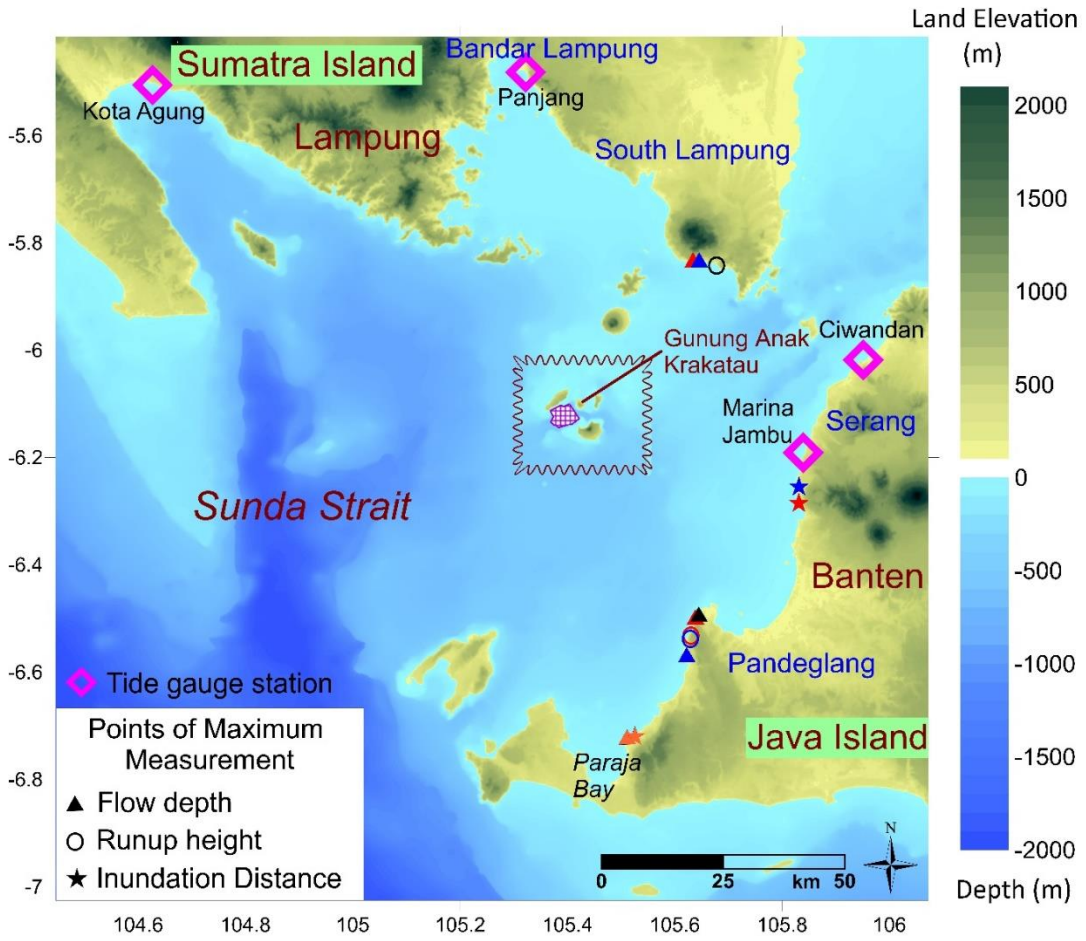

Figure 3.2 General view of the study area, including the gathered field survey results and tide gauge locations. The crosshatched area shows the post-event bathymetry data in the southwestern proximity of GAK. Triangle, circle and star symbols represent the maximum measured values of flow depth, runup height, and inundation distance, respectively, in different post-event field surveys. The orange color represents Indonesian national field survey team measurements, the red color represents Syamsidik et al. (2020), the blue color represents Muhari et al. (2019), and the black color represents Takabatake et al. (2019) field survey results.

According to Muhari et al. (2019)'s inferences from their field survey, which was performed four days after the tsunami, the tsunami runup heights highly differed due to the local morphology. Moderate tsunami runups were observed at flat coastal areas (Lampung and the northern part of Banten coast in 6.17°S–6.49°S), whereas high

runups at cliff-type beaches (southern part of Banten in 6.50°S–6.65°S). They indicated a maximum runup of 13.5 m (6.51699°S, 105.63335°E) at a cliff-type beach in the south of Banten (Figure 3.2) and a maximum inundation distance of 330 m (6.26°S, 105.83°E) in the flat coastal areas. The team also measured the maximum flow depth as 5.4 m at the southern coast of Banten (6.56774°S, 105.61664°E). They also highlighted the effect of coastal forests on tsunami impact according to their airborne survey. They observed a reduction of tsunami height up to 88% at the southern part of the Banten coast (impacted by a 3.6-m tsunami). In contrast, they observed complete damage to the coastal forest on the islands surrounding Anak Krakatau. They indicated that the runups at these coastal areas most probably were much higher.

Syamsidik et al. (2019) also conducted a field survey two days after the event in 5 main areas (Pandeglang and Serang districts on the western coast of Banten, South Lampung and Tanggamus districts of Lampung Province). They investigated flow depths, inundation, building damage behavior and tsunami boulder transportation to infer velocity. According to their findings, tsunami flow depths were relatively higher in Banten area than at Lampung, where a maximum of 6.6 m flow depth was measured at Cipenyu Beach (6.503802°S, 105.640432°E). A maximum runup of 14.9 m was indicated at Tanjung Jaya Beach at Pandeglang District (in the south of Banten, 6.517582°S, 105.633862°E), which is consistent with Muhari et al. (2019). They found out that the tsunami arrival times were slightly faster in Banten than on the Lampung side, although the initial time of tsunami generation from the source is still questionable. Furthermore, their maximum velocity estimation was about 4.37 m/s from a tsunami boulder measured at Banten.

Another field survey was conducted by the team of Takabatake et al. (2019) about three weeks after the event. They inferred from the observations that relatively higher inundation and runup heights were found in the north-northeastern direction from Anak Krakatau in Sumatra island, with a maximum surveyed runup height of 6.8 m (5.837889°S, 105.66806°E). They observed significantly higher runup heights at Cipenyu Beach (Pandeglang, 6.505361°S 105.641389°E), with a maximum of 12.6

m, similar to the other two previous field studies. They also commented that the three islands surrounding Anak Krakatau might reasonably have partially prevented the larger wave propagation along the Sunda Strait, considering their relatively big size with respect to Anak Krakatau.

The surveys by Borrero et al. (2020) reported runup heights of up to 85 m in the nearest islands to the Anak Krakatau volcano at a distance of approximately 5 km from the tsunami source. Heidarzadeh et al. (2020c) measured tsunami inundation distances of 18−212 m. They stated that properties and people located at a distance of at least 100 m from the coast were saved from the destructive tsunami waves.

To summarize, as inferred from the four field survey studies presented above, higher flow depth and runup values were observed in the Banten area (in Java Island) rather than the Lampung area (in Sumatra Island). Larger inundation was found in Serang on the northern coast of Banten (Figure 3.2) due to the flat topography in the inundation area. In the Lampung area (Figure 3.2), higher flow depth and runup values were reported in the Kunjir area, Kalianda district in South Lampung. Figure 3.2 shows the available highest flow depth, runup height, and inundation distance measurements, as well as the locations mentioned above gathered from the field survey studies.

3.2 Numerical Simulations

In the near-field area, the flank failure was modeled as a combination of subaerial and submarine mass movements by applying the TWO-LAYER model (Imamura and Imteaz 1995). It was originally structured to simulate the motion of a mass movement in two layers, where the bottom layer is the sliding mass, and the upper layer is the responding fluid flow. The model solves the depth-averaged non-linear shallow water wave equations using the finite difference technique within two interfacing layers with appropriate kinematic and dynamic boundary conditions at the seabed, interface, and water surface (Imamura and Imteaz, 1995; Yalciner et al.,

2002; Kawamata et al., 2005; Heidarzadeh, Krastel and Yalciner 2014, Latcharote et al. 2016). The governing equations of the 2D TWO-LAYER model are written as follows. Figure 3.3 also shows the working principle of the TWO-LAYER landslide model which treats the moving mass layer like the flow of another fluid with a different density (ρ_2).

$$\frac{\partial \eta_1 - \partial \eta_2}{\partial t} + \frac{\partial M_1}{\partial x} + \frac{\partial N_1}{\partial y} = 0 \tag{3.1}$$

$$\frac{\partial M_1}{\partial t} + \frac{\partial}{\partial x}\left(\frac{M_1^2}{D_1}\right) + \frac{\partial}{\partial y}\left(\frac{M_1 N_1}{D_1}\right) + gD_1\frac{\partial \eta_1}{\partial x} = 0 \tag{3.2}$$

$$\frac{\partial N_1}{\partial t} + \frac{\partial}{\partial x}\left(\frac{M_1 N_1}{D_1}\right) + \frac{\partial}{\partial y}\left(\frac{N_1^2}{D_1}\right) + gD_1\frac{\partial \eta_1}{\partial y} = 0 \tag{3.3}$$

$$\frac{\partial \eta_2}{\partial t} + \frac{\partial M_2}{\partial x} + \frac{\partial N_2}{\partial y} = 0 \tag{3.4}$$

$$\frac{\partial M_2}{\partial t} + \frac{\partial}{\partial x}\left(\frac{M_2^2}{D_2}\right) + \frac{\partial}{\partial y}\left(\frac{M_2 N_2}{D_2}\right) + gD_2\left(\alpha\frac{\partial D_1}{\partial x} + \frac{\partial \eta_2}{\partial x} - \frac{\partial h}{\partial x}\right) + \frac{\tau_x}{\rho_2} = 0 \tag{3.5}$$

$$\frac{\partial N_2}{\partial t} + \frac{\partial}{\partial x}\left(\frac{M_2 N_2}{D_2}\right) + \frac{\partial}{\partial y}\left(\frac{N_2^2}{D_2}\right) + gD_2\left(\alpha\frac{\partial D_1}{\partial y} + \frac{\partial \eta_2}{\partial y} - \frac{\partial h}{\partial y}\right) + \frac{\tau_y}{\rho_2} = 0 \tag{3.6}$$

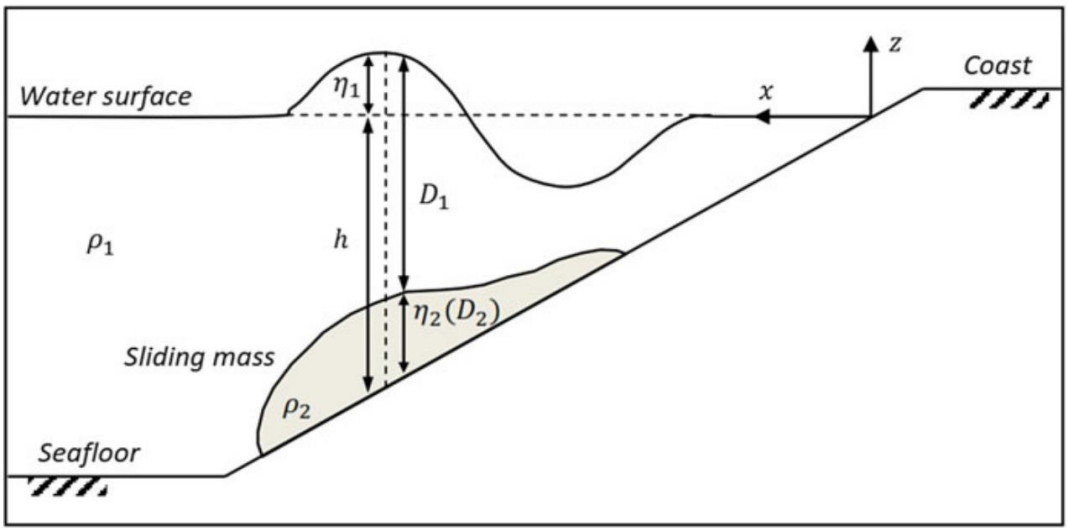

Figure 3.3 Sketch showing the two-layer landslide model working principle (retrieved from Heidarzadeh et al. 2014)

For the far-field propagation of the waves, the NAMI DANCE model, which solves the nonlinear form of shallow water equations using the water surface disturbances as the inputs and simulates propagation and coastal amplification of long waves, is employed. The governing equations of NAMI DANCE are given in Equations (3.7)-(3.9). The equations were solved using a staggering leapfrog scheme numerical solution procedure in nested domains with rectangular structured mesh.

$$\frac{\partial \eta}{\partial t} + \frac{\partial M}{\partial x} + \frac{\partial N}{\partial y} = 0 \tag{3.7}$$

$$\frac{\partial M}{\partial t} + \frac{\partial}{\partial x}\left(\frac{M^2}{D}\right) + \frac{\partial}{\partial y}\left(\frac{MN}{D}\right) + gD\frac{\partial \eta}{\partial x} + \frac{\tau_x}{\rho_w} = fN \tag{3.8}$$

$$\frac{\partial N}{\partial t} + \frac{\partial}{\partial x}\left(\frac{MN}{D}\right) + \frac{\partial}{\partial y}\left(\frac{N^2}{D}\right) + gD\frac{\partial \eta}{\partial y} + \frac{\tau_y}{\rho_w} = -fM \tag{3.9}$$

The subscripts 1 and 2 in Equations (3.1)-(3.6) represent the water layer (upper layer) and the sliding mass (lower layer), respectively. η_1 is the wave height of the ocean water and η_2 is the sliding mass thickness, ρ_1 and ρ_2 represent the densities of the water layer and the sliding mass, g is gravitational acceleration, M_1, M_2 and N_1, N_2 are discharge fluxes in the horizontal plane along x and y coordinates, α is the density ratio $\frac{\rho_1}{\rho_2}$. η is the water surface elevation, t is time, x and y are the horizontal coordinates in zonal and meridional directions, $D = h(x,y) + \eta$ is the total water depth, $h(x,y)$ is the undisturbed basin depth, ρ_w is seawater density, f is the Coriolis parameter with $f = (2\omega sin\emptyset)$ where ω is the angular velocity of the Earth, and ∅ is the y-coordinate in degree. M and N, the discharge fluxes in the x and y directions, are calculated from

$$M = \int_{-h}^{\eta} u dz = u(h+\eta) = uD, \qquad N = \int_{-h}^{\eta} v dz = v(h+\eta) = vD \tag{3.10}$$

τ_x and τ_y are the bottom shear stresses in the horizontal plane along x and y directions where the Manning law is used for the bottom friction with coefficient n, also given in the following.

$$\frac{\tau_x}{\rho} = \frac{gn^2}{D^{7/3}} M\sqrt{M^2+N^2} \tag{3.11}$$

$$\frac{\tau_y}{\rho} = \frac{gn^2}{D^{7/3}} N\sqrt{M^2+N^2} \tag{3.12}$$

The Manning's coefficient n is calculated by

$$n = \sqrt{\frac{f_b(\eta+D)^{1/3}}{2g}} \tag{3.13}$$

where f_b denotes the bottom friction, which is taken as 0.015 as a representative value for concrete, asphalt, sand and graveled surfaces based on Table 8.9.1 of Mays (2011), which suggests different n values for different covers of flow plane.

The offshore boundary condition in NAMI DANCE is defined by setting the total derivative of water surface elevation (Equation 3.14) constant, either equal to zero for open (outgoing) boundary and to one for reflective boundary.

$$\frac{D\eta}{Dt} = \frac{\partial\eta}{\partial t} + u\frac{\partial\eta}{\partial x} + v\frac{\partial\eta}{\partial y} \tag{3.14}$$

Here the velocities u and v can be taken as $\sqrt{gD}$.

For defining the boundary condition on the shore, the wave front condition is determined by locating the wave front between the dry and submerged cells and a cell is taken as dry or submerged depending on the condition of the total water depth at the cell.

$$if\ D = h + \eta > 0, \quad submerged\ cell \tag{3.15}$$

$$if\ D = h + \eta \leq 0, \quad dry\ cell \tag{3.16}$$

If the ground elevation in the dry cell is lower than the water level in the submerged cell, the discharge across the boundary between the two cells is carried out. Otherwise, the discharge is taken as zero. In the runup case, as the water moves up and down the land, it is not easy to express this moving boundary condition and an approximation is needed (Imamura et al. 2006). In the leap-frog numerical scheme

of NAMI DANCE, grid points are alternatively located for velocity and water level assuming that the water level is already computed as a computational cell. If the water level is higher than the latter, the water may flow into the landward cell.

The dispersion effect on the landslide generated waves was examined theoretically in Mirchina & Pelinovsky (1982) and Glimsdal et al. (2013) by developing a parameter, dispersion time, which is given by $\tau_d = \frac{6*h^2*L}{\lambda^3}$, where h is the water depth in the source area, L is the distance traveled and λ is the wavelength or source length (width of the landslide source). They investigated several previous tsunami events by applying the approach and found out that for a $\tau_d > 0.1$ value, the dispersion is significant, whereas for $\tau_d < 0.01$, it can be neglected. For the GAK case, τ_d can be calculated as 0.06 for average values of $h = 75$ m ($0 - 150$ m depth range in the source area), $L = 75$ km (coastlines ~50-100 km from the source) and $\lambda = 3.5$ km. Therefore, the dispersion effect was neglected within the scope of this study as it is more important for the propagation of short waves generated by landslides at farther distances rather than such a case (Glimsdal et al., 2013; Heidarzadeh et al., 2020a).

3.2.1 Data and Methods

The satellite imagery and aerial photography from different angles before and after the event reveals the flank failure above sea level. The satellite images taken before and after the event indicate that a large part of the upper cone of the volcano does not exist anymore, which is one of the reasons for the creation of the tsunami (Figure 3.4b and Figure 3.4c). As can be seen in Figure 3.4a, the volcano peak that had measured about 300 meters was missing after the collapse. However, the submarine part of the landslide is also another essential parameter for the estimation of sliding volume, which is one of the key parameters in simulating the tsunami.

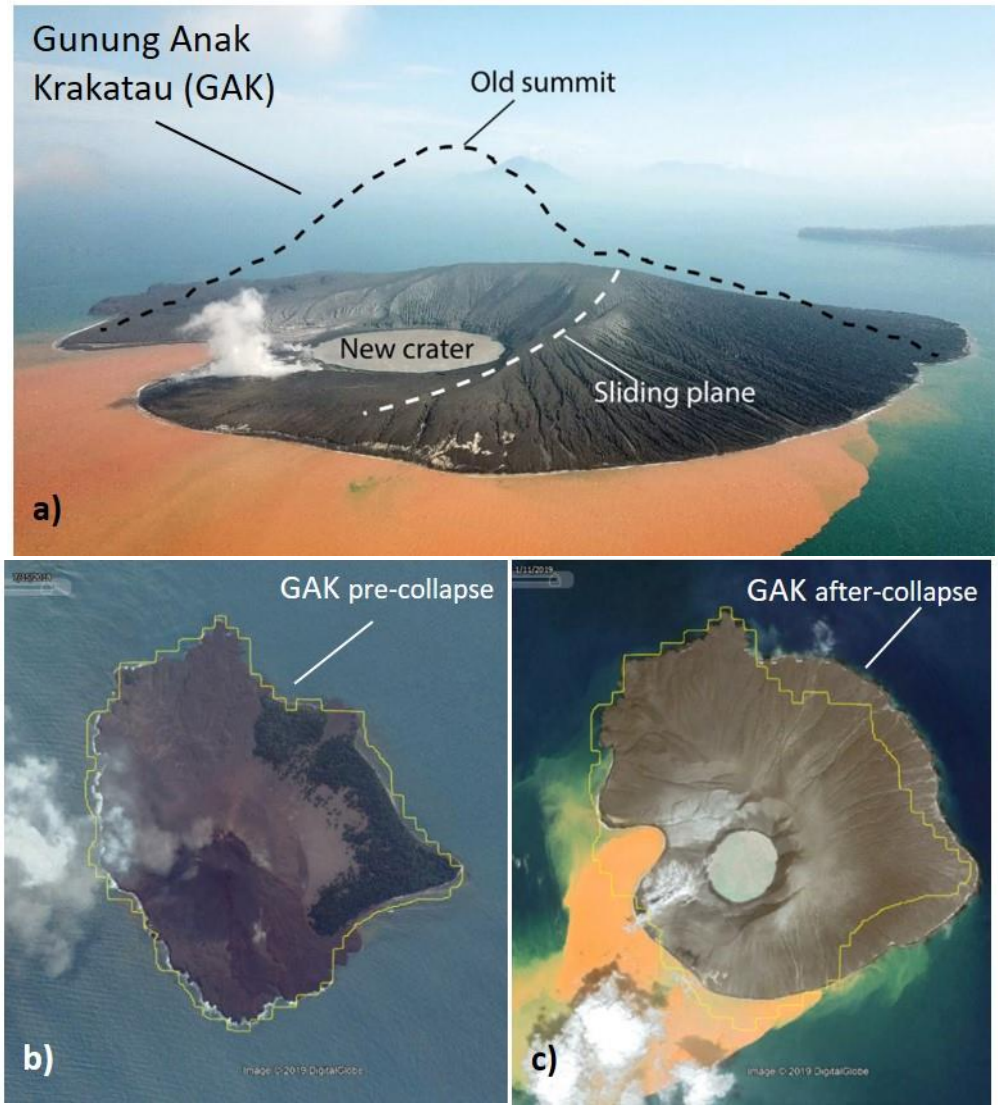

Figure 3.4 a) A Drone image of two weeks after the flank collapse (Source: German Research Centre for Geosciences GFZ, Potsdam, from https://phys.org/news/2019-10-early-heralded-fatal-collapse-krakatau.html) after-collapse. Aerial images of GAK b) pre-collapse (July 2018) and c) after-collapse (January 2019) of GAK. The yellow line is the 10 m resolution coastline in our database.

3.2.1.1 Volumetric Calculations

The volumetric calculations for the flank failure of this event are on a quite wide range starting from 0.104 km^3 (Williams et al., 2019) to 0.326 km^3 (Heidarzadeh et

al., 2020a). Williams et al. (2019) indicated volumes of 0.004 km^3 for the subaerial failure of GAK and in the order of 0.1 km^3 for the submarine failure. Paris et al. (2020) suggested that the AK tsunami was created by a flank collapse with a volume of 0.15 km^3. Similarly, Omira and Ramalho (2020) proposed a volume of 0.135 km^3 for the AK collapse occurring as a sequence of two failures. Giachetti et al. (2012) previously modeled a hypothetical lateral landslide of GAK with a collapsing volume of about 0.28 km^3. Heidarzadeh et al. (2020a) presented volumes of 0.175 km^3 and 0.326 km^3 for their best two models. Moreover, Grilli et al. (2019) also presented their most likely scenario with a volume of 0.27 km^3. Walter et al. (2019) also concluded a volume change of ~0.1 km^3 estimated from simple DEM subtraction, which was very conservative and could increase to 0.23 km^3. They found that value was still conservative and might have been accompanied by a submarine loss of the same order of magnitude.

3.2.1.2 Bathymetry/Topography Data

The bathymetry and topographical data of 10 m resolution for the GAK surrounding area (Figure 3.2, rectangle in brown wave line), whereas 205 m resolution data for the whole Sunda Strait area (Figure 3.2) are used. The data was compiled by Indonesian experts from BATNAS, which stands for BATimetri NASional (National Bathymetry) produced by Indonesia Geospatial Information Agency (Badan Informasi Geospasial, BIG in Indonesia). For the submarine part, the bathymetric data obtained before the event (in 2016) and a post-collapse one (after the post-event survey in 2018) with a resolution of 90-140 m (provided from BPPT, Indonesia) in the southwestern proximity of GAK, was employed (Figure 3.5). The pre-event data was gained in 2016 from Geospatial Information Agency (BIG in Indonesia), and the post-event bathymetric data was provided by BPPT from the survey campaign a month after the event in 2018. The data has not been published yet. This survey was conducted for the installation of the Ocean Bottom Unit (OBU) to support Indonesia Tsunami Early Warning System (InaTEWS) Project. The difference between pre and

post-event data shows a maximum of ~200m shoaling and a maximum of ~50m deepening within the surveyed area (Figure 3.5). The difference is much higher along the slopes and decreases as reaching the flat (deeper) part (a). Hence, there is a bathymetry change in the area, verified by the measurements, indicating submarine slope failures in the southwestern proximity of GAK. The effect of this phenomenon should be investigated on the generated tsunami either individually or combined with other topographic changes.

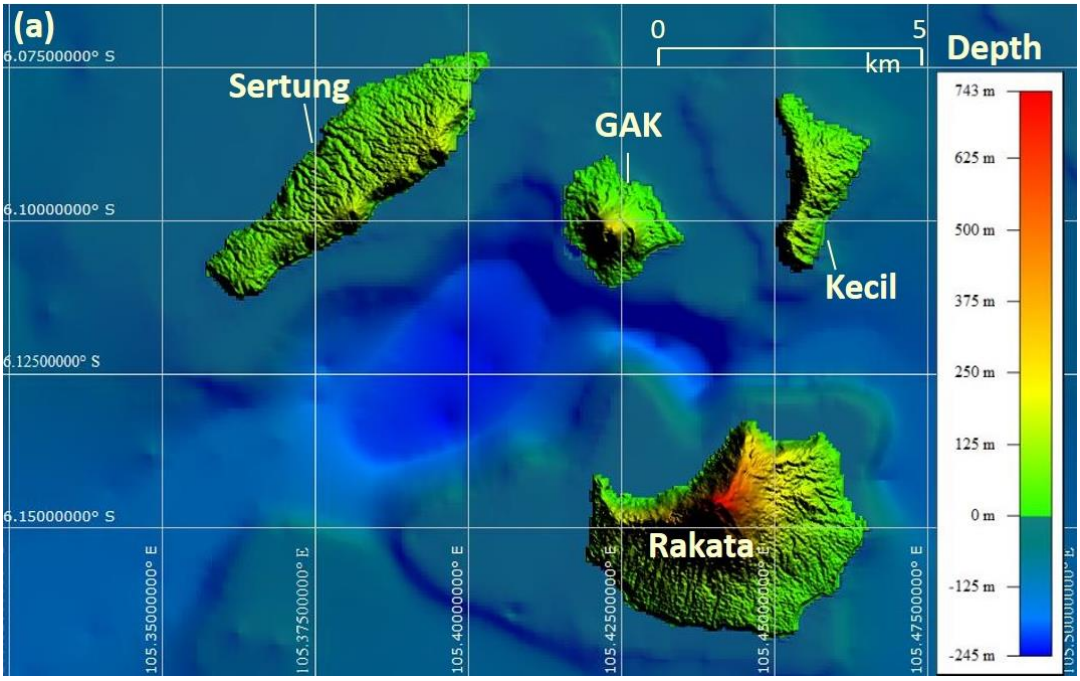

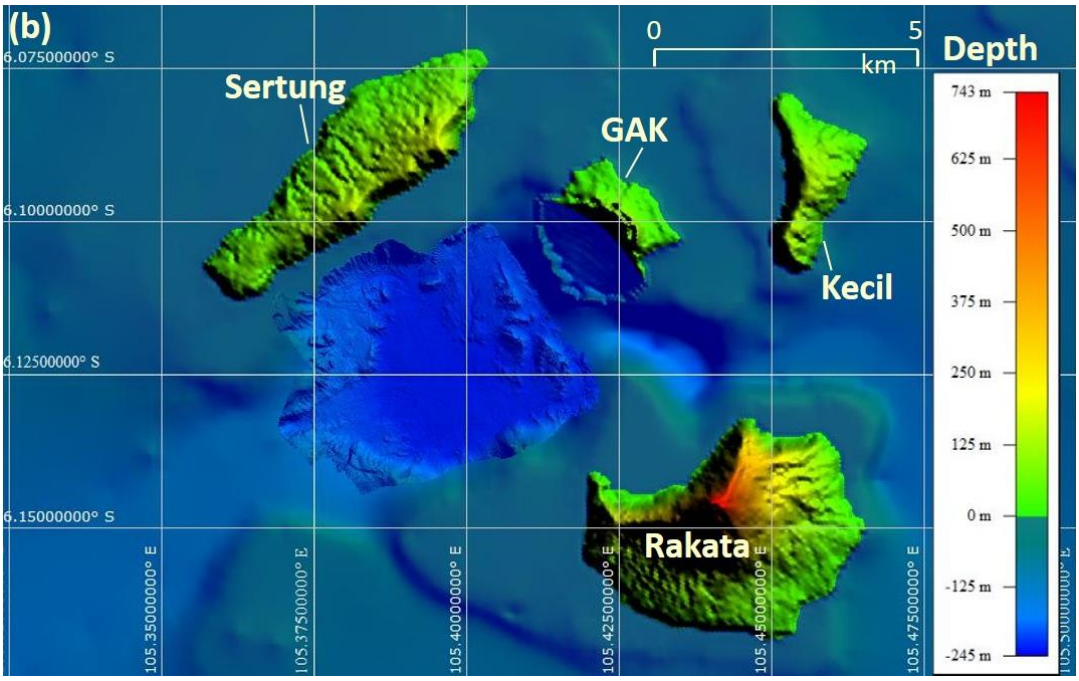

Figure 3.5 a) Pre-event and b) post-event bathymetry-topography in the southwestern proximity of GAK. The post-event topography of GAK shows the hypothesized flank collapse used in the simulations. The bathymetry before the event was obtained in 2016, and the post-event bathymetry was provided by BPPT, a month after the 22 December 2018 event. The difference between pre and post-event data shows a maximum of ~200m shoaling and a maximum of ~50m deepening as bathymetry change within the surveyed area.

A single uniform grid of 80 m grid size was applied in the simulations. The submarine mass movements, as well as the flank collapse, are simulated for 420 seconds duration in the TWO-LAYER model. The water surface elevation and momentum fluxes in x and y directions computed from the TWO-LAYER model are inputted to NAMI DANCE. Then, the wave propagation and inundation are modeled by using NAMI DANCE for a total duration of 180 min with a 0.25 sec time step. The premise behind this approach is the computational demand, i.e., the very long computational time needed to perform the same simulation in the two-layer model. Furthermore, after the landslide stops at a certain time (generally in 6-7 minutes), tsunami propagation can be solved by a single layer nonlinear shallow

water (NLSW) model (Grilli et al., 2019; Latcharote et al., 2016; Yalciner et al., 2014). Therefore, NAMI DANCE, capable of simulating NLSW equations very fast in the GPU environment, was used after 420 seconds.

3.2.1.3 Tide Gauge Records

Four available tide gauge measurements in the Sunda Strait are utilized in addition to the field survey data to compare our numerical modeling results. Kota Agung Tide Station (KTAG) and Pelabuhan Panjang Tide Station (PANJ) are located on Sumatra Island (Figure 3.2), and Serang Tide Station (SERA) and Ciwandan Tide Station (BNTN) are located on Java Island (Figure 3.2). The mareogram data recorded the tsunami of GAK came from these tide stations owned by Indonesia Geospatial Information Agency. Those can be downloaded freely from http://ina-sealevelmonitoring.big.go.id/ipasut/. The de-tided surface elevation data, recorded at 1 min intervals and de-tided by using a band-pass filter of FFT to remove the astronomical tide, is given in Figure 3.6.

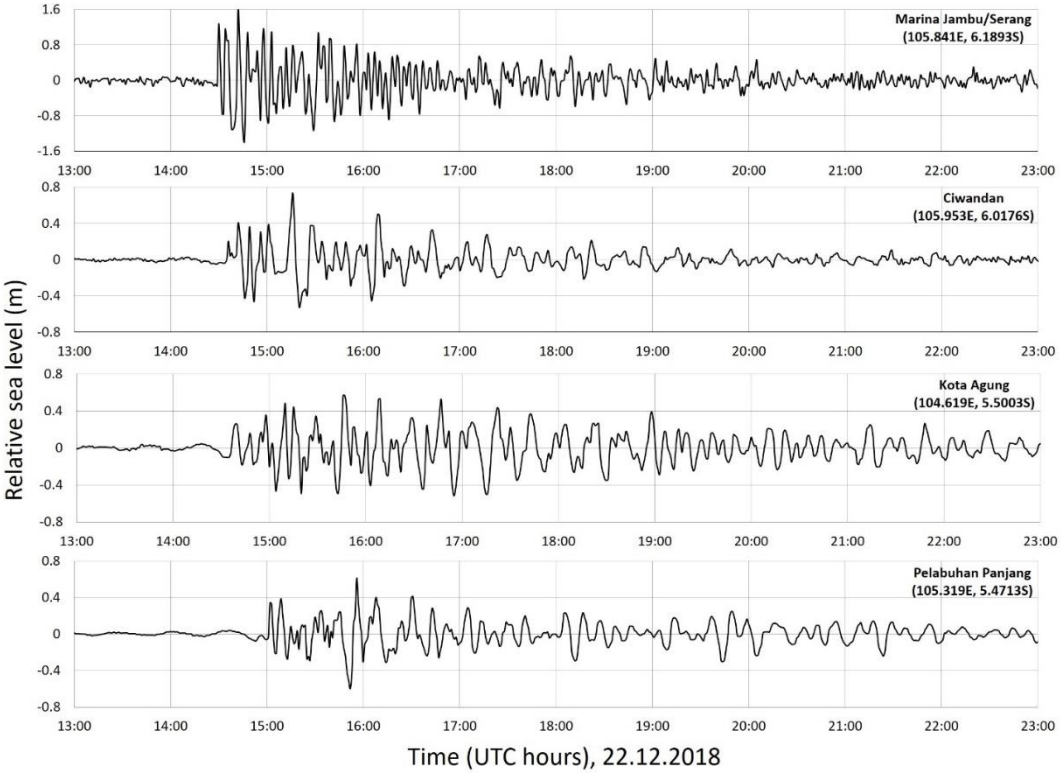

Figure 3.6 The detided tide-gauge records of December, 22 2018 Sunda Strait tsunami at four stations

3.3 Source Scenarios

Based on the available data and information presented above, a *flank collapse scenario* was hypothesized with a volume of 0.25 km^3 as a combination of different submarine and subaerial mass movements as the major source scenario of the December 22, 2018 Sunda Strait tsunami. This model assumes a 260 m maximum initial amplitude at 105.42245^{o}E 6.10208^{o}S (at the cone center), following a heterogeneous distribution in an elliptical shape with a 2.0 km major axis in the southwest direction and a 1.5 km minor axis in the northwest direction. Figure 3.7a shows the bathy/topo change within the collapse area, where it shows a maximum elevation of ~266m in the cone part of the volcano in the database before the event and this part expired after the collapse (also given in Figure 3.7b). Tsunami

generation was simulated via TWO-LAYER model for up to 420 seconds. The simulated water surface elevations at different time steps are shown in Figure 3.7c for 140, 280 and 420 seconds. After the landslide stopped, tsunami propagation was solved by NAMI DANCE.

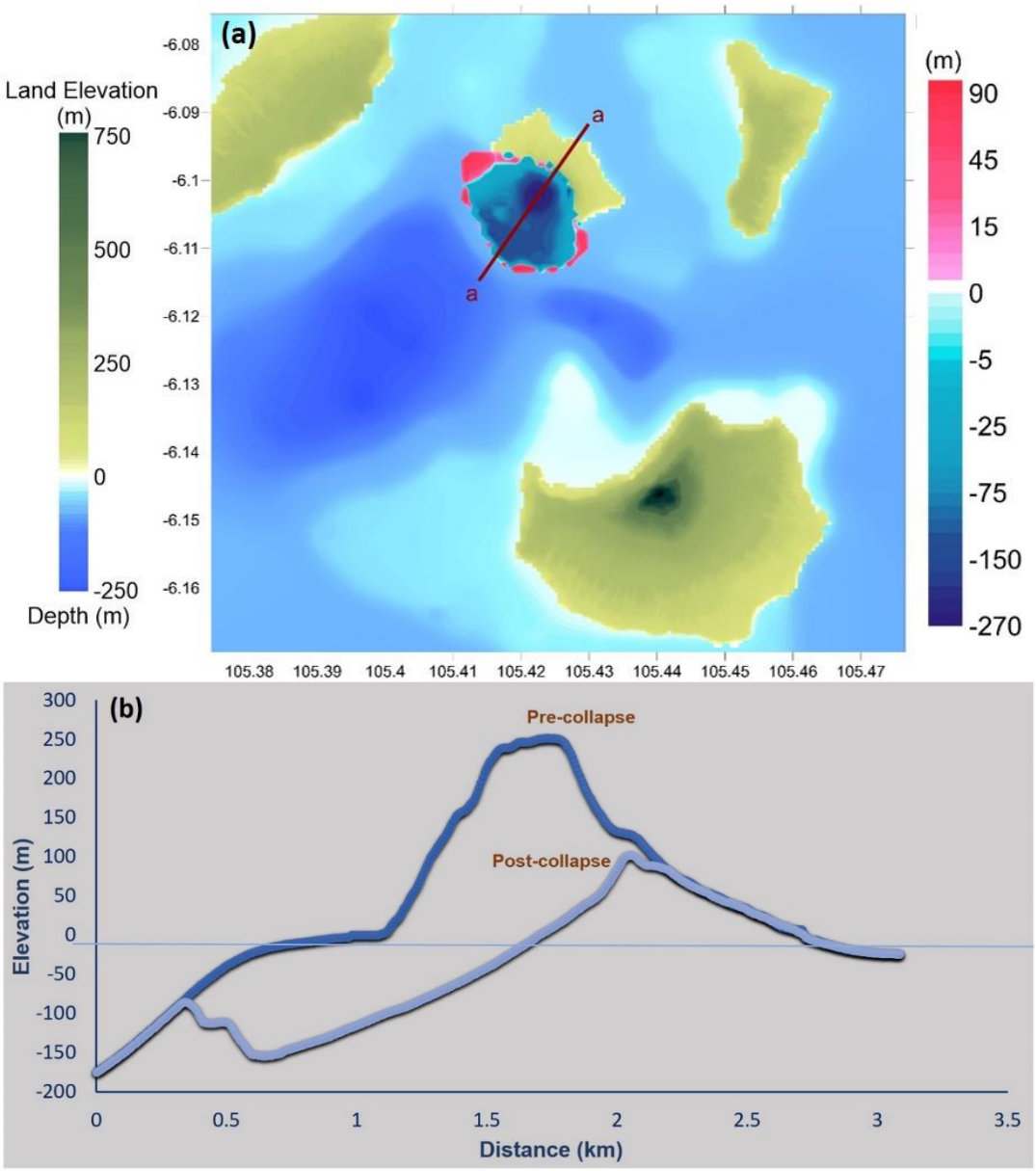

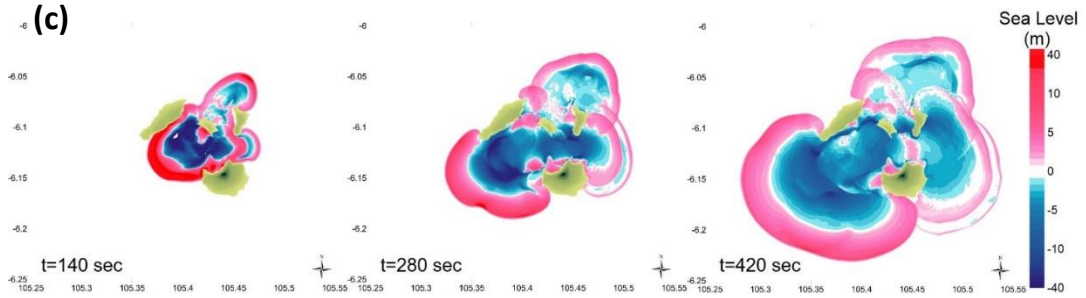

Figure 3.7 Configuration of modeled flank collapse of GAK for a 0.25 km^3 volume scenario showing bathy/topo change within the collapse area considered as a combination of subaerial and submarine landslide input for tsunami generation using TWO-LAYER model (Refer to Figure 3.5b for the post-event bathy/topo of GAK), b) profile of section a-a for pre-collapse and post-collapse cases, c) simulated water surface elevations with two-layer at different time steps for 140, 280 and 420 seconds.

In addition to the flank collapse scenario, a bathymetric dataset through pre- and post-event analyses was employed, demonstrating clear evidence of submarine slope failures in the southwestern proximity of GAK. Hence, two additional scenarios of elliptical landslide sources on the slopes of the bathymetry change area were considered and simulated, searching for the possible effects of the tsunami that might be generated by these submarine landslides. The rationale behind this selection is to show the resulting amplitudes if these failures occurred like a single event or in the form of a series of landslides (could be triggered by seismic motion/volcanic eruption). These two scenarios of possible submarine slope failures were also simulated by TWO-LAYER model for 420 seconds for the tsunami generation (Figure 3.8c and Figure 3.8d) and NAMI DANCE was applied for the propagation part.

Scenario 1 includes *one pair of elliptical sources* (Figure 3.8a) in the area of pre and post-event bathymetric changes. The location of the source was specified considering a relatively steep slope and high bathymetry change area. Each ellipse has dimensions of 5 km on the major axis and 0.6 km on the minor axis directions.

The maximum amplitudes were assumed as ±200 m with interpolated cubic Hermite shapes considering the difference between pre and post-event data, which shows a maximum of ~200m shoaling and a maximum of ~50m deepening within the surveyed area (Figure 3.5).

Scenario 2 includes *two pairs of elliptical sources* (Figure 3.8b) in the area of pre and post-event bathymetric changes adopted rather than one pair to cover different possible slope failure areas. All ellipses were assumed to have dimensions of 3 km on the major axis. Each southwestern ellipse has a 0.5 km minor axis, whereas the southeastern ones have 0.6 km. The cubic Hermite shape was used with maximum amplitudes of ±150 m and ±200, respectively.

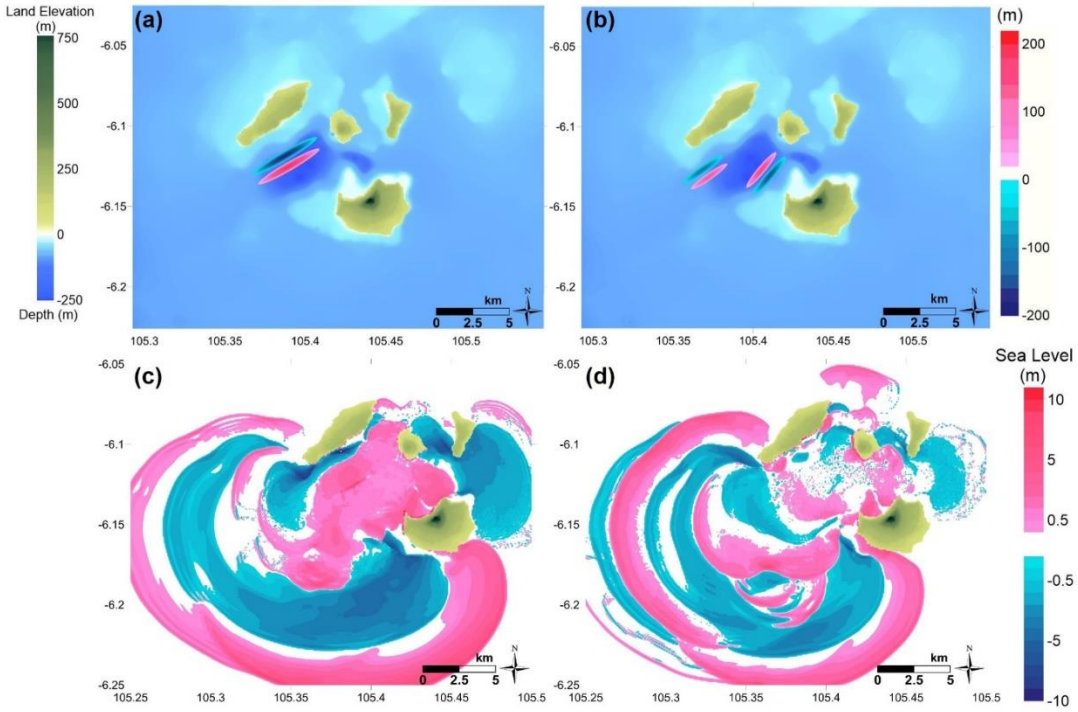

Figure 3.8 Simulated two different scenarios of submarine mass movements in the southwestern proximity of GAK a) Scenario 1: one elliptical source (uplift and subsidence) in the pre and post-event bathymetric change area, b) Scenario 2: two elliptical sources (uplift and subsidence) in the pre and post-event bathymetric change area. Blue color represents the sliding area, whereas reddish color represents the deposition area in (a) and (b).

3.4 Results and Discussion

The simulation results consist of the distribution of computed maximum water levels in the study domain as well as the time histories of water levels at the tide gauge stations for the suggested flank collapse and two scenarios of submarine landslides as well. A comparison table was also prepared (Table 3.1), including the computed tsunami amplitudes and flow depths with observed/measured flow depths, runup heights, and inundation distances from different field surveys summarized in Chapter 3.1. Based on tide gauge data comparison, the simulation results show an overall good agreement with the measurements for the flank collapse scenario, indicating that the suggested configuration and volume are capable of producing the measured amplitudes. Although there are some discrepancies in tide gauge record comparison (Figure 9a-d), the first three-four waves are well captured by taking into account the measurement interval of the time series at the gauges and their locations inside harbors or enclosed basins.

The distribution of computed maximum surface elevations both in the proximity of GAK and in the Sunda Strait (Figure 3.9a and Figure 3.9b) seem quite similar to other published models (Grilli et al. 2019), which considered a similar collapse volume; and slightly larger than Paris et al. (2020) and Omira and Ramalho (2020) which considered smaller collapse volumes. Our model also produced 22-30 m surface elevations in the southwestern locality of GAK (Figure 3.9b), which agree with the estimated runup heights of 25-30 m on the Rakata and Sertung islands (Paris et al. 2020). The results also show a good agreement with the observations from the national survey team, Muhari et al. (2019), and Takabatake et al. (2019) in the locations where maximum coastal amplitudes were observed. Furthermore, Table 3.1 indicates that the suggested source scenario can better produce the observed flow depths at the southern part of Pandeglang in 6.40^{o}S–6.55^{o}S where the cliff-type beaches are present. However, we cannot notice the expected inundation in the simulation results, as observed in the flat type coastal topography in Serang. That is most probably due to the synthetic objects (peaks) in the topographic data

(originating from the 205 m resolution data, which was resampled to 80 m in the simulations) obstructing the flow in the model.

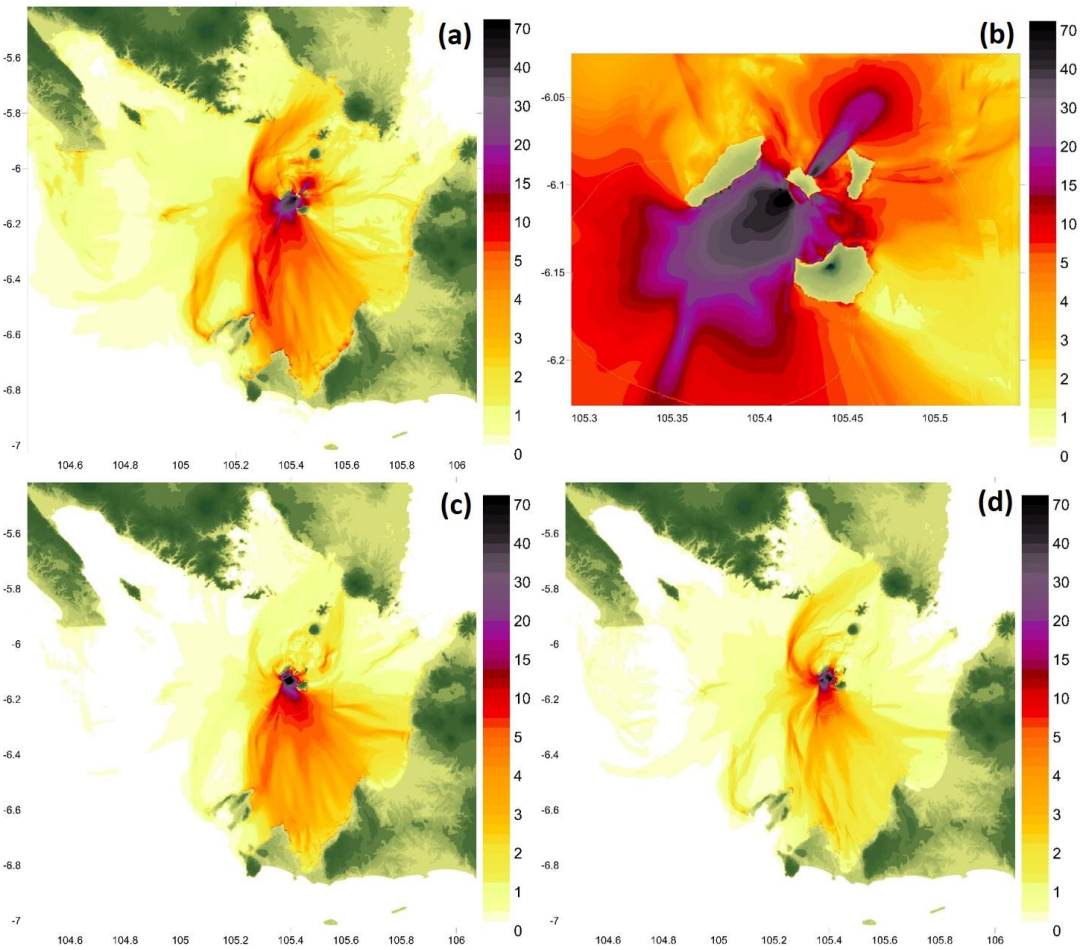

Figure 3.9 Computed maximum water surface elevations in Sunda Strait with NAMI DANCE during 180 min simulation according to a) flank collapse scenario, b) flank collapse scenario in the near-field area of GAK, c) Scenario 1, and d) Scenario 2. Units are in meters.

A sliding volume of 0.25 km^3 is presented in the best source scenario (flank collapse), which gives a maximum positive initial amplitude of 260 m and 22-28 m high leading waves in the near-field region of GAK. The source dimensions and produced maximum initial amplitudes and the computed surface elevations are compatible with the results of Heidarzadeh et al. (2020a) and Grilli et al. (2019) in the near-field area of GAK. Grilli et al. (2019) presented a volume of 0.27 km^3 for

their most likely scenario, which resulted in more than 30 m surface elevation in the near-field area. Heidarzadeh et al. (2020a) suggested slide volumes of 0.175 km^3 and 0.326 km^3 for their best two models, which produced 100 m and 150 m initial amplitudes, respectively. As our model follows a heterogeneous distribution in the sliding area, it is expected that our model has a higher maximum initial amplitude than Heidarzadeh et al. (2020a) for the suggested 0.25 km^3 slide volume.

According to the simulation results of the two submarine failure scenarios, Scenario 1 shows a similar distribution of maximum water level in the study domain with the flank collapse scenario (Figure 3.9c). However, if Scenario 1 had been triggered by the December 22 eruption and occurred as a rapid failure (as assumed), it could create remarkable subsequent waves that would contradict the coastal observations. On the other hand, it remains questionable if the slope failures considered in Scenario 2 occurred as a single event since they did not produce significant coastal amplitudes on the Java and Sumatra Islands, if measured accurately (Figure 3.9d and Figure 3.12). The large difference with the measurements in terms of wave arrival times at the four tide gauge locations, given in Figure 3.11, also suggests that these scenarios based on the bathymetric change in the nearfield area of GAK were not accompanied by December 22 GAK event.

Table 3.1 Observed/measured flow depths (F.D.), runup heights (R.H.) and inundation distances (I.D.) from Muhari et al. (2019), Syamsidik et al. (2019) and Takabatake et al. (2019) compared with computed maximum tsunami amplitudes (T.A) including arrival times (A.T.).

Place	Region	Coordinate		Observed/Measured			Computed		
		Lon	Lat	F.D. (m)	R.H. (m)	I.D. (m)	F.D. (m)	T.A. (m)	A.T. (min)
Karang Suragak	Serang	105.85474[2]	-6.15339[2]	3.00[2]	-	249[2]	0.93	1.73	31.4
Bulakan	Serang	105.83619[1] 105.83655[2]	-6.20232[1] -6.19960[2]	3.75[2]	5.8[1]	131.2[1*] 330[1**]	1.32	2.13	35.3
Tangkolo, Suka Ramai	Labuan, Pandeglang	105.82924[1] 105.82924[2] 105.82944[3]	-6.26258[1] -6.26251[2] -6.26461[3]	2.30[1] 2.30[2] 1.01[3](I.H.)	-	-	0.25	1.65	36.9
Caringin Beach	Labuan, Pandeglang	105.82223[2]	-6.35841[2]	3.15[2]	-	-	1.66	2.16	37.6
Labuan Port	Labuan, Pandeglang	105.82255[2]	-6.37293[2]	1.10[2]	-	-	1.34	2.24	40.8
Lantera	Labuan, Pandeglang	105.8231[3]	-6.37628[3]	3.36[3](I.H.)	-	-	2.14	2.54	40.6
Labuan	Pandeglang	105.82153[1]	-6.37886[1]	1.20[1]	-	-	1.29	2.09	40.8
Tanjung Lesung	Pandeglang	105.65436[1] 105. 65472[2]	-6.48011[1] -6. 48006[2]	1.55[1] 2.30[2]	-	-	1.86	2.96	25.6
Tanjung Lesung	Pandeglang	105.65939[1]	-6.48078[1]	-	7.07[1]	-	1.91	2.05	26.6
Cipenyu Beach	Pandeglang	105.63815[1] 105.6414[3]	-6.50781[1] -6.50536[3]	-	8.51[1] 12.58[3]	-	4.31	4.88	25.9
Cipenyu Beach	Pandeglang	105.64101[1] 105.64146[2]	6.50466[1] -6.50419[2]	2.24[1] 2.56[2]	-	-	1.58	3.90	26.1
Cipenyu Beach	Pandeglang	105.64043[2] 105.6408[3]	-6.50380[2] -6.50416[3]	6.60[2] 11.28[3](I.H.)	-	-	4.77	4.91	25.7
Tanjung Jaya	Pandeglang	105.62888[1] 105.62841[2]	-6.52415[1] -6.52690[2]	-	10.94[1] 11.14[2]	159[1**]	3.58	4.49	26.4
Tanjung Jaya	Pandeglang	105.62356[1] 105.62436[3]	-6.54209[1] -6.54508[3]	1.54[1] 5.39[3](I.H.)	-	-	1.36	3.36	28.3
Kunjir	Kalianda, South Lampung	105.65678[1] 105.65998[2] 105.65161[3]	-5.83513[1] -5.83589[2] -5.83592[3]	2.90[1] 3.33[2] 4.21[3](I.H.)	-	160[2]	0.94	3.41	34.7

I.H. Inundation Height

*average, **maximum

Superscripts: [1]Muhari et al. (2019), [2]Syamsidik et al. (2019) and [3]Takabatake et al. (2019)

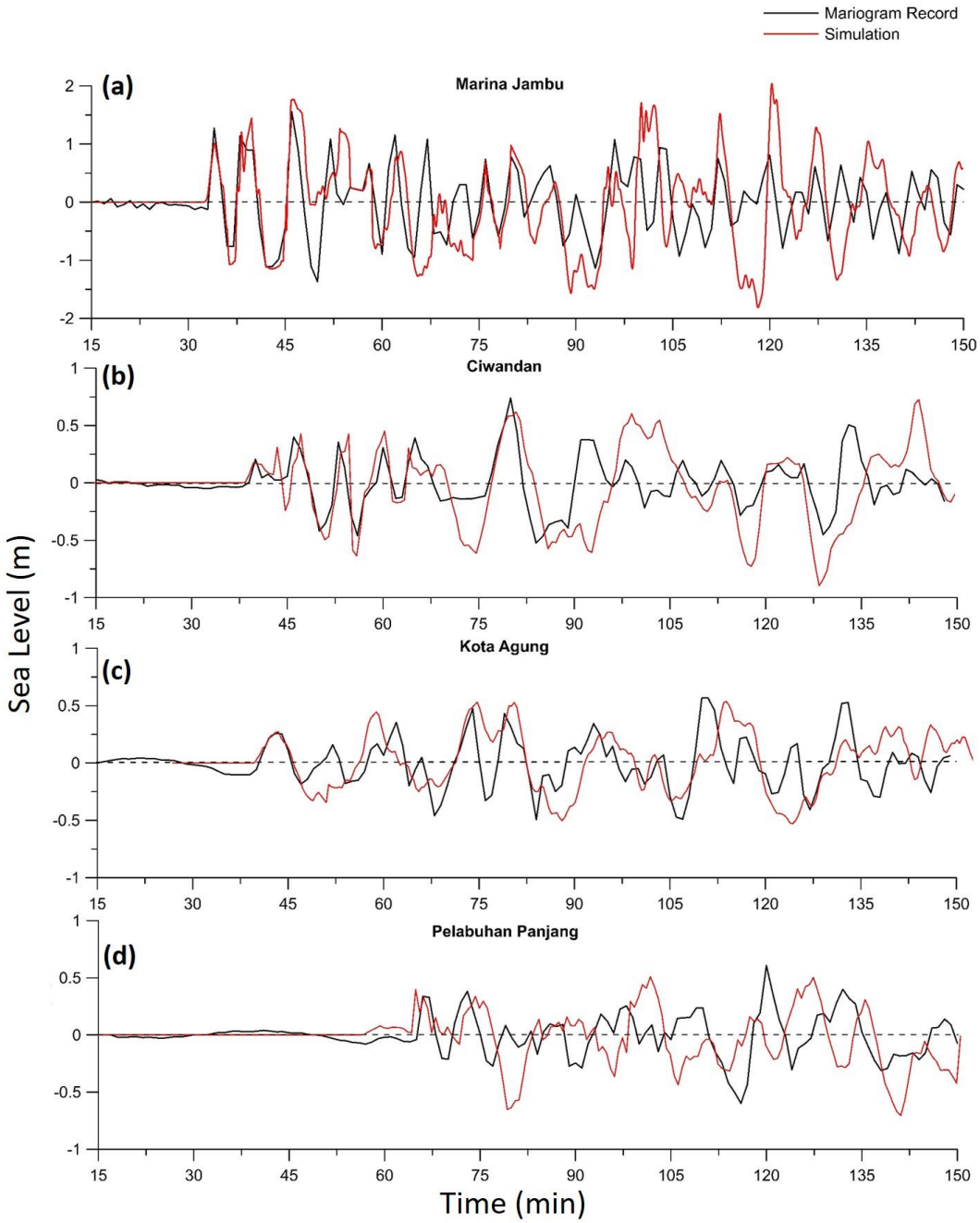

Figure 3.10 Comparison of recorded tide gauge data (in black) and computed water surface elevations (in red) for the flank collapse scenario for the December 2018 GAK tsunami at a) Marina Jambu, b) Ciwandan, c) Kota Agung, and d) Panjang stations. Time=0 is the estimated collapse time of 13:56 UTC.

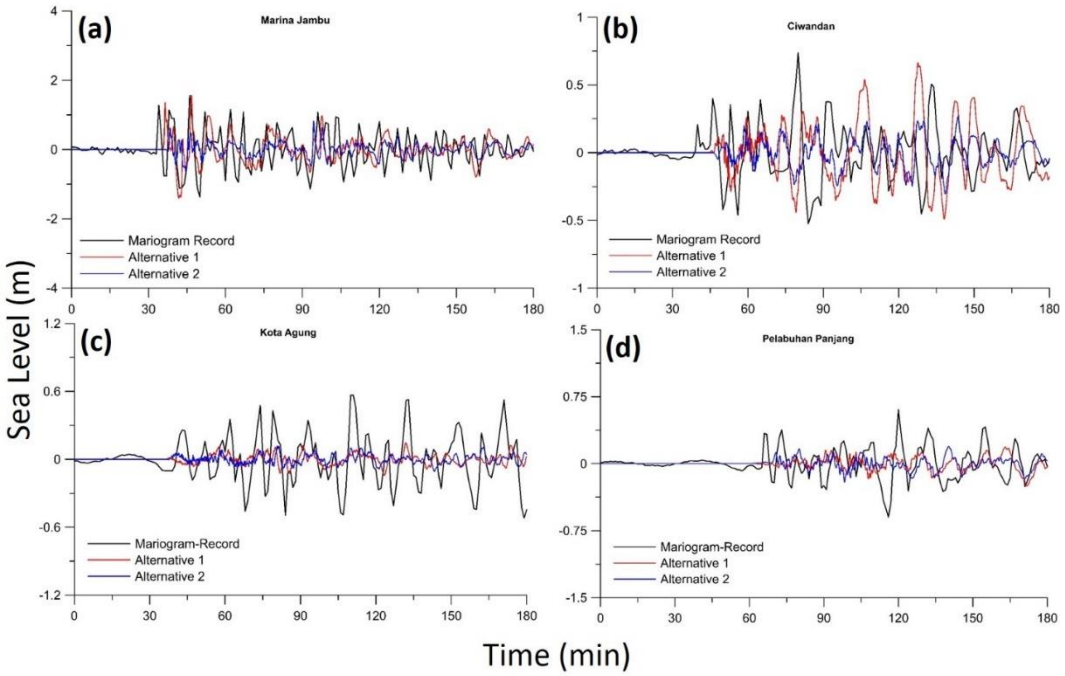

Figure 3.11 Comparison of recorded tide gauge data (in black) and computed water surface elevations (in colours) of two different submarine landslide scenarios (Scenario 1 and Scenario 2) at a) Marina Jambu, b) Ciwandan, c) Kota Agung and d) Panjang stations. Time=0 is the estimated collapse time 13:56 UTC.

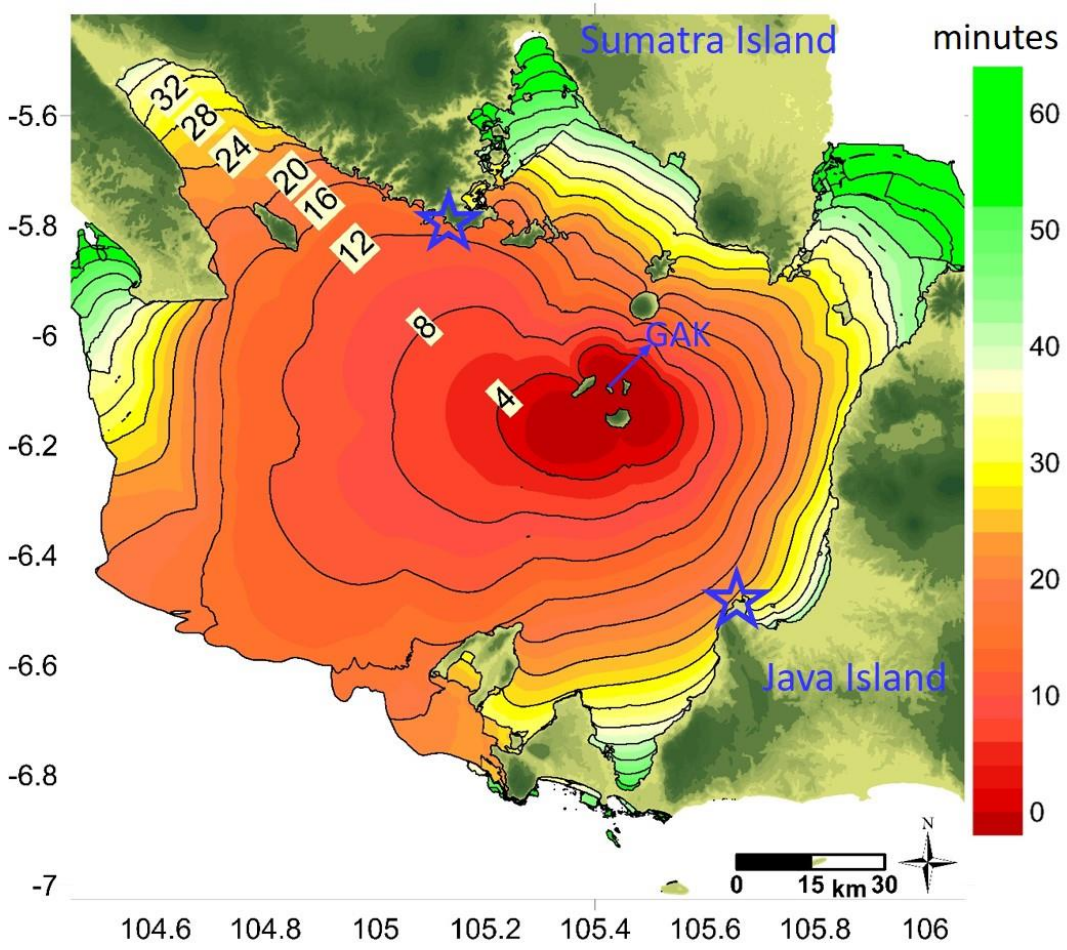

Figure 3.12 Estimated first wave travel times due to GAK flank collapse scenario in the Sunda Strait. The contour interval is four minutes. The origin time of the collapse is assumed to be 13:56 UTC. Fastest wave arrivals to the coast were found to be Tanjung Lesung in Pandeglang Regency (with a travel time of 24 minutes) and Kiluan/Kelumbayan Beach region in Tanggamus Regency (with a travel time of 13 minutes) at Java and Sumatra Islands, respectively. These locations are marked with blue stars.

Furthermore, despite the short arrival time characteristic of volcanic tsunamis, the possible fastest travel times and arrival locations can be identified by applying accurate numerical modeling approaches based on realistic scenarios. In this regard, a first wave travel time map in the Sunda Strait is prepared based on the flank collapse scenario and presented in Figure 3.12. The map shows that

Kiluan/Kelumbayan Beach area (Tanggamus Regency in Sumatra Island) and Tanjung Lesung area (Pandeglang Regency in Java Island) are the potential locations of fastest wave arrivals to the coast with travel times of 24 minutes and 13 minutes, respectively. Additionally, Table 3.1 includes the arrival times of computed maximum tsunami waves according to the flank collapse for main coastal places at Java and Sumatra islands.

CHAPTER 4

LONG WAVE GENERATION AND AMPLIFICATION DUE TO TRAVELING ATMOSPHERIC DISTURBANCES

An ocean model should capture both the offshore generation and resonant amplification of meteotsunamis, and the nearshore amplification of the tsunami-like waves by topography and harbor resonance (Rabinovich, 2009). The long wave generation and amplification induced by spatial and temporal changes of the atmospheric pressure disturbance were numerically solved by introducing atmospheric pressure and wind field terms to the nonlinear shallow water equations. Several numerical tests were conducted to compare against a new analytical solution for meteotsunami generation in water channels of quasi-parabolic shape (including triangular cross-section). Furthermore, the possible wave amplification factors, oceanographic and hydrodynamic, were investigated via more than 550 simulations based on different basin configurations and pressure field characteristics, prepared with the "isolation of parameter" principle in mind. The influence of the wind field characteristics, the other contributing forcing mechanism in meteotsunami generation but lacking sufficient coverage in literature, on the wave response was also examined with numerous numerical tests and has been discussed briefly. The simulations were performed with the new module of NAMI DANCE numerical code that solves the 2D nonlinear shallow water equations with the introduced air pressure and wind field forcing terms to simulate meteotsunamis (Dogan et al. 2021b).

4.1 Resonance by Coupling of Ocean Waves and Atmospheric Pressure Forcing

When the air pressure decreases gradually, the water level in the sea region rises in the order of 1 cm with respect to a 1 hPa pressure decrease, which is called the

inverse barometer law. However, the water level changes can be amplified significantly by the resonance when the ocean wave speed coincides with the speed of the atmospheric perturbation. This is why meteotsunamis are referred to as multi-resonant phenomena. The three most important resonance mechanisms are (i) Proudman resonance (Proudman, 1929), (ii) Greenspan resonance (Greenspan, 1956), and (iii) shelf resonance (Monserrat et al., 2006).

Proudman resonance is the main cause of meteotsunamis happening all over the world, as indicated by Pattiaratchi and Wijeratne (2015). Proudman resonance occurs when the velocity (V) of the atmospheric pressure movement coincides with the celerity (c) of the ocean wave, which denotes $V = c$. The changes in the water surface level due to air pressure disturbances depend on the Froude number (Fr). When $Fr \approx 1.0$, during the propagation of the ocean waves, atmospheric energy is actively absorbed and, therefore, strong amplification occurs. On the other hand, there are several essential assumptions on the oceanographic and atmospheric conditions for the Proudman resonance to be constructed: one-dimensional flat bottom basin with no background current component and one-dimensional atmospheric pressure with constant amplitude and moving speed (Proudman, 1929).

Greenspan resonance occurs where the air pressure velocity in the alongshore direction (V_l) is close to the propagation phase speed of j-th mode of edge waves (c_j). The generated edge waves amplify due to Greenspan resonance in relation to the amplitude and the propagation speed of the pressure disturbance and the beach slope.

The atmospheric pressure disturbance causes the initial change in water level, and water oscillations develop due to the shelf geometry such as length, water depth, topographic funneling, and bed slope. Shelf resonance occurs when the period or wavelength of the air pressure disturbance and the generated ocean waves coincide with the natural oscillation period of the continental shelf region (Monserrat et al., 2006).

The internal resonance mechanism has another important role in wave amplification inside enclosed basins and harbors since a double resonant mechanism (Rabinovich,

1993) can be expected from both interactions between the atmospheric forcing-ocean wave and ocean wave-harbor/bay basin. When the natural resonance frequency of a semi-enclosed basin coincides with the frequency of the incoming wave and/or forcing to the basin, strong amplification can be observed inside the basin. Yalciner and Pelinovsky (2007) presented a numerical method for determining periods of free oscillations in basins with irregular geometry and bathymetry. Bailey et al. (2014) stated that in long, narrow, and shallow bays, stronger oscillations occur as the system tends to have a low rate of energy dissipation, also reminding Miles and Munk's (1961) well known "harbor paradox" of the narrower entrance of the harbor, better protection of the harbor but the stronger long oscillations inside the harbor.

4.2 Problem and Method

4.2.1 Wave Generation and Propagation due to Atmospheric Pressure Disturbances

The energy transfer in the oceans is generally categorized according to the energy sources such as wind, fault rupture, submarine or subaerial landslides, meteorological disturbances, or solar and planetary attractions. Air pressure disturbances cause water level changes and hence generate long-period ocean waves. High atmospheric pressure causes a static water level drop and contrariwise, low atmospheric pressure causes a static water level rise. Due to the different water level changes at high pressure and low-pressure regions, the water level differences cause the wave generation in the sea and, consequently, propagation and coastal amplification in the ocean area.

On the other hand, bathymetry is a critical factor that may cause amplification of the long waves generated by atmospheric pressure disturbance. The speed of pressure disturbance (V) and wave celerity (c) are the two important parameters that govern the characteristics of the generated long waves. The speed of the ocean waves is controlled by the water depth and it may be faster or slower or equal to the speed of

pressure disturbance. Therefore, the shape and propagation of the generated ocean waves differ according to the different speeds of pressure disturbances as well as the magnitude and gradient of the pressure disturbance. In this part of the study, the effects of the speed of pressure disturbance on the generation, propagation and amplification of the ocean waves in the basins with different bathymetries were investigated.

Simple analytical solutions for long wave generation in a basin of constant depth (Proudman resonance) and a basin with a linear sloping bottom (Greenspan resonance) are given in their original papers (Proudman, 1929; Greenspan, 1956) and then reproduced in many papers. Here, the aim is to define the analytical solution of the linear shallow water model and compare the results with the numerical solution. Thereafter, analytical and numerical models were applied to certain test cases. This helps to interpret the verification of the numerical model and the wave generation and propagation mechanism due to the speed of pressure disturbances over different types of basins. As one major oceanographic factor influencing the wave amplification is the slope of the shelf during the passage of the pressure forcing, 23 different basins with shelf bathymetries were constructed with shelf slopes from 1:10 to 1:700. The numerical tests were also conducted for 13 different traveling speeds for each shelf bathymetry basin ranging from 7 m/s to 44 m/s. Furthermore, the generation and amplification of the ocean waves due to traveling wind fields were investigated by numerical modeling considering the three important hydrodynamic factors affecting wind speed (U_w), moving speed (S_w) and the drag coefficient (C_d).

4.2.2 Analytical Solution

The governing equations for tsunami wave generation by atmospheric disturbances in narrow bays and channels can be written similar to the 1D case studied for tsunami landslide generation (Tinti and Bertolucci, 2000; Tinti et al., 2001; Liu et al., 2003b; Pelinovsky, 2006; Didenkulova et al., 2010; Didenkulova and Pelinovsky, 2013):

$$\frac{\partial S}{\partial t} + \frac{\partial}{\partial x}(uS) = 0 \tag{4.1}$$

$$\frac{\partial u}{\partial t} + u\frac{\partial u}{\partial x} + g\frac{\partial H}{\partial x} = -\frac{1}{\rho}\frac{\partial P_{atm}}{\partial x} \tag{4.2}$$

where $H(x,t)$ is the water depth along the channel axis, $u(x,t)$ is the flow velocity averaged over a cross-section, g is the gravitational acceleration, $S(H,x,t)$ is the variable cross-section of the bay filled by water, $P_{atm}(x,t)$ is atmospheric pressure, ρ is the density of water, x is coordinate, and t is time. Resonant amplification of tsunami waves induced by moving landslides is studied in Didenkulova et al. (2011), Didenkulova and Pelinovsky (2012). Generated ocean waves and the atmospheric disturbance are assumed to be uniform over the cross-section.

In the important case of the quasi-parabolic channel, its cross-section is described by

$$z \sim |y|^{m_a} \tag{4.3}$$

where m_a is an arbitrary positive constant. In particular, $m_a = 1$ describes the triangular channel, $m_a = 2$ describes the parabolic channel, and $m_a \to \infty$ corresponds to the rectangular channel. As a result, we may compute a function $S(H)$:

$$S(H) = \int_{-y_0}^{+y_0} z(y)dy \sim H^{(m_a+1)/m_a} \tag{4.4}$$

For such channels, we have equations (4.1) and (4.2) for wave components:

$$\frac{\partial H}{\partial t} + u\frac{\partial H}{\partial x} + \frac{m_a}{m_a+1}H\frac{\partial u}{\partial x} = 0 \tag{4.5}$$

$$\frac{\partial u}{\partial t} + u\frac{\partial u}{\partial x} + g\frac{\partial H}{\partial x} = -\frac{1}{\rho}\frac{\partial P_{atm}}{\partial x} \tag{4.6}$$

The set of analytical solutions can be obtained if the atmospheric disturbance is weak. In this case, we may use the linear version of these equations:

$$\frac{\partial \eta}{\partial t} + \frac{m_a}{m_a+1}h\frac{\partial u}{\partial x} = 0 \tag{4.7}$$

$$\frac{\partial u}{\partial t} + g\frac{\partial \eta}{\partial x} = -\frac{1}{\rho}\frac{\partial P_{atm}}{\partial x} \tag{4.8}$$

Where $\eta(x,t) = H(x,t) - h$ is the vertical displacement of the water surface, and h is an unperturbed water depth along the longitudinal axis.

The system can be reduced to the wave equation:

$$\frac{\partial^2 \eta}{\partial t^2} - c^2 \frac{\partial^2 \eta}{\partial x^2} = \frac{c^2}{\rho g} \frac{\partial^2 P_{atm}}{\partial x^2} \tag{4.9}$$

Where

$$c = \sqrt{\frac{m_a}{m_a+1} gh} \tag{4.10}$$

Where c is the wave celerity in the channel. It is important to note that equation (4.9) has a universal form for waves in channels of any quasi-parabolic shape; the channel shape is described by the coefficient m_a in equation (4.10). Namely, this equation is studied to describe the Proudman resonance (Melinand, 2015).

By introducing

$$\zeta_a = \frac{P_{atm}}{\rho g} \tag{4.11}$$

Equation (3.9) can be rewritten in the following form

$$\frac{\partial^2 \eta}{\partial t^2} - c^2 \frac{\partial^2 \eta}{\partial x^2} = c^2 \frac{\partial^2 \zeta_a}{\partial x^2} \tag{4.12}$$

In particular, the response to the static atmospheric disturbance is described by the well-known “inverse barometer law”.

$$\eta = -\zeta_a = -\frac{P_{atm}}{\rho g} \tag{4.13}$$

It means that low atmospheric pressure can cause the sea level to rise, and high atmospheric pressure leads to depression in the mean sea level. If the pressure is moving, the resonance can occur when the pressure velocity is close to the wave celerity. Then, replacing

$$\eta = \zeta - \zeta_a \tag{4.14}$$

Equation 3.12 can be transformed to

$$\frac{\partial^2 \zeta}{\partial t^2} - c^2 \frac{\partial^2 \zeta}{\partial x^2} = \frac{\partial^2 \zeta_a}{\partial t^2} \tag{4.15}$$

In this form, Equation 4.15 coincides with those used for tsunamis generated by landslides (Tinti et al., 2001; Liu et al., 2003b; Pelinovsky, 2006; Didenkulova et al., 2010; Didenkulova and Pelinovsky, 2013).

Initial conditions for the shallow water system (4.7)-(4.8) are applied to both $\eta(x,t)$ and $u(x,t)$. If at the initial moment the ocean rests, it can be transformed into conditions for the function $\eta(x,t)$

$$\eta(x,0) = 0, \qquad \frac{\partial \eta}{\partial t}(x,0) = 0. \tag{4.16}$$

The linear equation (4.15) with initial conditions (4.16) can be solved using the Duhamel's integral

$$\eta(x,t) = \frac{c}{2\pi} \int_0^t d\tau \int_{x-c(t-\tau)}^{x+c(t-\tau)} dy \frac{\partial^2 \zeta_a(y,\tau)}{\partial y^2}, \tag{4.17}$$

Which can be integrated once

$$\eta(x,t) = \frac{c}{2\pi} \int_0^t d\tau \left(\frac{\partial \zeta_a[x+c(t-\tau),\tau}{\partial x} - \frac{\partial \zeta_a[x-c(t-\tau),\tau}{\partial x} \right). \tag{4.18}$$

This solution can be used for the control of numerical computations. If the atmospheric disturbance moves with a constant velocity, V, the solution (4.18) becomes algebraic

$$\eta(x,t) = \frac{Fr^2}{Fr^2-1} \zeta_a(x - Vt) - \frac{Fr^2}{2(Fr-1)} \zeta_a(x - ct) + \frac{Fr^2}{2(Fr+1)} \zeta_a(x + ct), \tag{4.19}$$

Where

$$Fr = \frac{V}{c} \tag{4.20}$$

is the Froude number. The wave celerity varies with depth, and Fr varies with the speed of the pressure disturbance and the generated waves.

The response to the moving disturbance represents three waves. The first term in equation (4.19) describes the forced wave, which propagates together with the

atmospheric disturbance. The forced wave can have different polarities depending on the regime of the disturbance motion. Assuming ζ_a is positive, the forced wave is positive in the super-critical regime ($Fr > 1$) and negative in the sub-critical regime ($Fr < 1$). The second term describes a free wave, which propagates with its own speed *c*. As the forced wave, it can also be of different polarities: negative in the super-critical regime and positive in the sub-critical regime; opposite to the forced wave. The last term corresponds to a smaller free wave of positive polarity.

For practice, it is useful to compare the amplitudes of waves moving in the same direction with the atmospheric disturbance. The ratio of the amplitude (*Q*) of the free wave (second term) to the amplitude (*P*) of the forced wave (first term) is

$$\frac{Q}{P} = \frac{Fr+1}{2}. \tag{4.21}$$

The general sectional view of long waves generated by moving constant atmospheric pressure is shown in Figure 1 for the case Fr < 1. The forced wave continuously interacts with the atmospheric pressure, propagates with the moving speed of the pressure and absorbs the atmospheric energy during the propagation. On the other hand, the free wave propagates with its own speed and after the generation by the initial impulse, the free wave does not draw additional external energy.

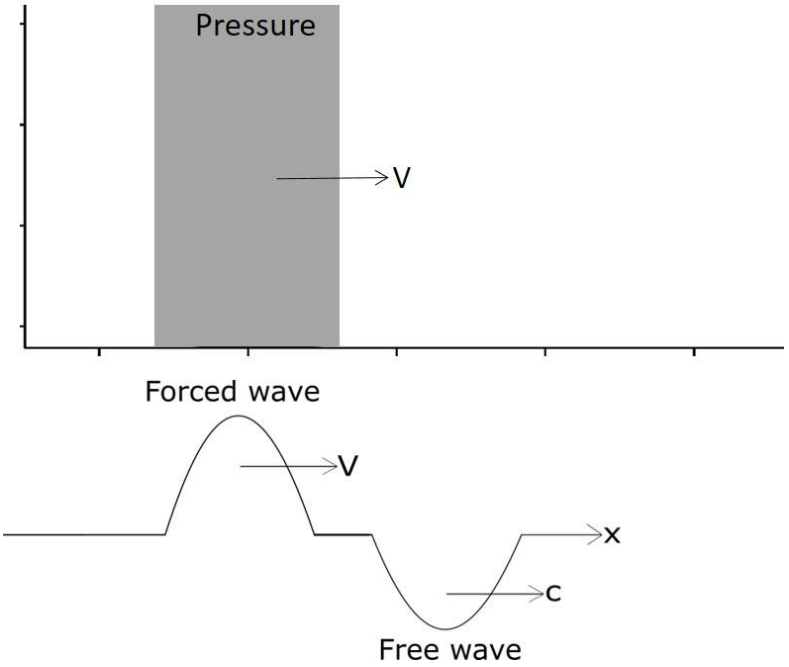

Figure 4.1 A schematic view of the moving constant low atmospheric pressure (plan view, top) and the general sectional view of long waves (bottom), propagating in the direction of the pressure.

Formula (4.21) is correct for any Fr. But for $Fr < 1$, it is the ratio of the front wave to the rear wave (forced wave is behind the free wave), as shown in Figure 4.1. For $Fr > 1$, the forced wave is in front of the free wave, and therefore, equation (4.21) gives the ratio of the rear wave to the front wave.

In the case of resonance ($Fr \to 1$), the solution (4.19) transforms into

$$\eta(x,t) = -\frac{t}{2}\frac{\partial \zeta_a(x-ct)}{\partial x} + \frac{1}{4}\zeta_a(x+ct) \tag{4.22}$$

which also indicates that wave amplitude increases with time.

4.2.3 Numerical Model

Three distinctions are important for the long waves induced by atmospheric pressure disturbances: i) generation of the wave, ii) propagation of the wave in deep water, and iii) propagation and coastal amplification in shallow water and on the shore.

Wave propagation in deep water can be explained by the linear shallow water equations. In contrast, in shallow water, wave dynamics is better described by the nonlinear shallow water equations, which also cover the surface and bottom stresses, Coriolis force, and shoaling (Eze et al., 2009). A full potential model or Boussinesq-type equations are even better in shallower regions. Several numerical models were tested and compared in Liu et al. (2008) and Lynett et al. (2017). Some of those numerical codes are COMCOT (Liu et al. 1994; 1995; 2008), TUNAMI-N2 (Imamura, 1996; Imamura et al., 2006; Liu et al., 2008), MOST (Titov and Synolakis, 1998; Liu et al., 2008; Lynett et al., 2017), NAMI DANCE (Liu et al., 2008; Kian et al., 2014; Sozdinler et al., 2015; Yalciner and Zaytsev, 2017; Metin, 2016; Lynett et al., 2017; Velioglu-Sogut and Yalciner, 2019), which use shallow water wave equations, while FUNWAVE (Kirby et al., 1998) and GEOWAVE (Watts et al., 2003) use Boussinesq-type equations. The aforementioned numerical models were developed for the numerical solution of co-seismic and/or landslide generated tsunamis without considering the atmospheric pressure disturbances.

In the present study, the nonlinear shallow water equations containing the air pressure forcing and wind field forcing terms are solved numerically to simulate generation, propagation and coastal amplification of long waves generated by the atmospheric pressure disturbances and wind field forcing. The set of two-dimensional equations with atmospheric pressure and wind field terms in Cartesian coordinates are given in equations (4.23)-(4.25):

$$\frac{\partial \eta}{\partial t} + \frac{\partial M}{\partial x} + \frac{\partial N}{\partial y} = 0 \tag{4.23}$$

$$\frac{\partial M}{\partial t} + \frac{\partial}{\partial x}\left(\frac{M^2}{D}\right) + \frac{\partial}{\partial y}\left(\frac{MN}{D}\right) + gD\frac{\partial \eta}{\partial x} + \frac{\tau_x}{\rho_w} + \frac{D}{\rho_w}\frac{\partial P_{atm}}{\partial x} - \frac{\rho_{air} C_D}{\rho_w} U_{w10}\sqrt{U^2{}_{w10} + V^2{}_{w10}} = 0 \tag{4.24}$$

$$\frac{\partial N}{\partial t} + \frac{\partial}{\partial x}\left(\frac{MN}{D}\right) + \frac{\partial}{\partial y}\left(\frac{N^2}{D}\right) + gD\frac{\partial \eta}{\partial y} + \frac{\tau_y}{\rho_w} + \frac{D}{\rho_w}\frac{\partial P_{atm}}{\partial y} - \frac{\rho_{air} C_D}{\rho_w} V_{w10}\sqrt{U^2{}_{w10} + V^2{}_{w10}} = 0 \tag{4.25}$$

where t is time, x and y are spatial coordinates in West-East and South-North directions respectively, η is the water surface elevation, ρ_w is the water density, ρ_{air}

is the air density, D is the water depth, M and N are the discharge fluxes in the x and y directions (Equation 3.10), τ_x and τ_y are the bottom shear stresses (Equations 3.11-3.12), P_{atm} is the atmospheric pressure in Pascal, U_{w10} and V_{w10} are the wind velocities at 10 m elevation in x and y directions, and C_D is the wind drag coefficient computed from the following equations:

$$C_D = (0.75 + 0.067(U_{w10} - u)) \cdot 10^{-3} \quad \text{for } U_{w10} \leq 26 \text{ m/s (Garrat, 1977)} \quad (4.26)$$

$$C_D = 2.18 \cdot 10^{-3} \quad \text{for } U_{w10} > 26 \text{ m/s (Powell et al. 2003)} \quad (4.27)$$

Since Coriolis force and friction are not included in the analytical solution, those were not included in the numerical tests for proper comparisons with the analytical solution.

In the numerical model, NAMI DANCE SUITE, in addition to standard inputs (bathymetry, initial water surface displacement, and fluxes if needed), the spatial distribution of the barometric pressure at the sea level in Pascal at one-minute intervals during the simulations was employed.

4.2.4 Verification of the Numerical Model

In order to verify the model to correctly calculate the long wave motion due to the effects of atmospheric pressure disturbances, the test simulations were conducted with a regular shaped flat bathymetry (200 km of distance between 0.9W to 0.9E longitudes, 195 km of distance between 0.885S to 0.885N latitudes and 200 m of constant depth). The North and South boundaries of the basin were used as solid impermeable boundaries in order to prevent the escape of waves through these borders. The East and West borders are open (outgoing) boundaries. The 16 km wide high pressure disturbance (98000 Pascal) propagating with a constant velocity from West to East was used in all simulations. The standard pressure over the basin was set as 100000 Pascal. The borders of the pressure disturbance were smoothed by the 2 km linear increase from and decrease to 100000 Pascal at the front and rear sides of the disturbance (Figure 4.2). The selected pressure disturbance band is an

exceptional case. The main reason for selecting this disturbance is to obtain higher water fluctuations for a better comparison of the simulation results.

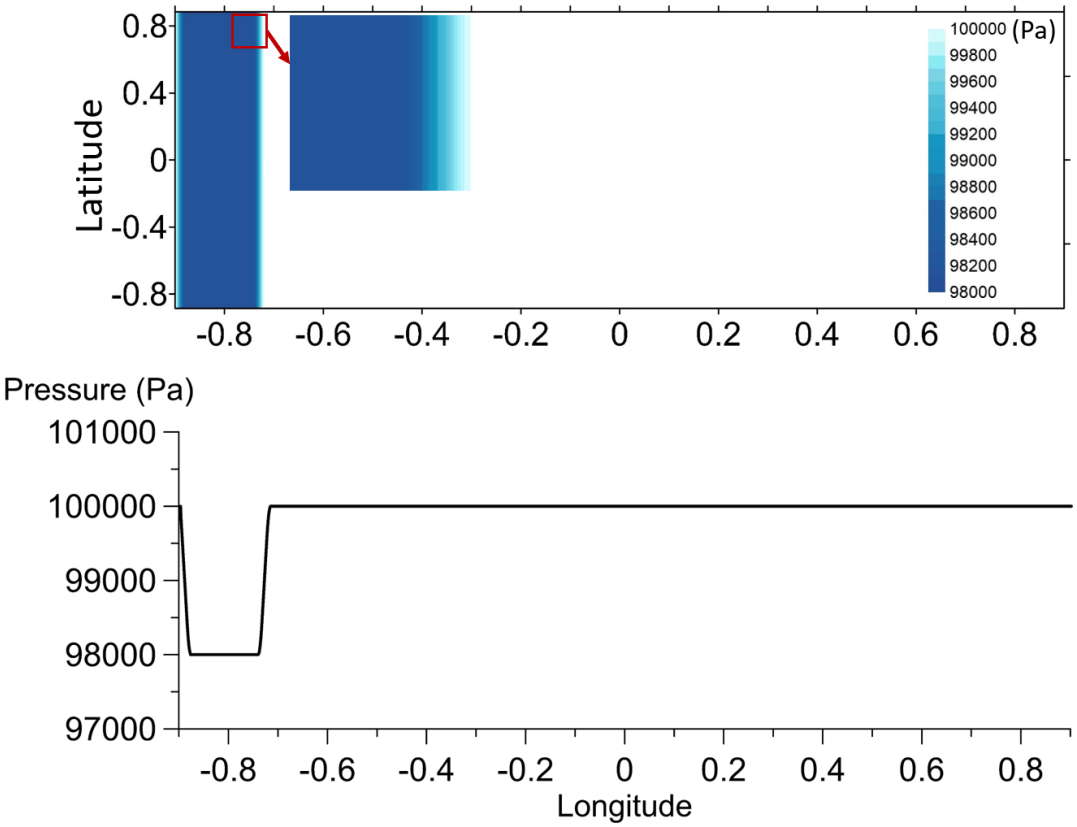

Figure 4.2 The top and sectional view of the pressure disturbance at the beginning of the simulation (t = 0).

For verification of the model, a flat bottom basin is selected where the wave celerity is constant and is equal to c = 44.3 m/s. Different constant speeds (V) of pressure disturbance are selected as 11 m/s, 22 m/s, 33 m/s, 44 m/s, 55 m/s, 66 m/s. Therefore, both sub-critical, critical and super-critical conditions defined by Equation 4.20 were used. The spatial grid size and time step were selected as 177 m and 1 s, respectively. The bottom friction, f_b, was selected as zero to satisfy the same friction condition with the analytical solution. The duration of each simulation was set according to the duration of the ocean wave and pressure disturbance propagation to leave the right boundary of the basin.

The distributions of water surface (sea states) and sectional views at zero latitude at selected time steps (t = 10 min, 20 min, 40 min and 60 min) over the flat bottom basin under pressure disturbance moving with 22 m/s, 44 m/s and 66 m/s speed are presented in Figure 4.3.

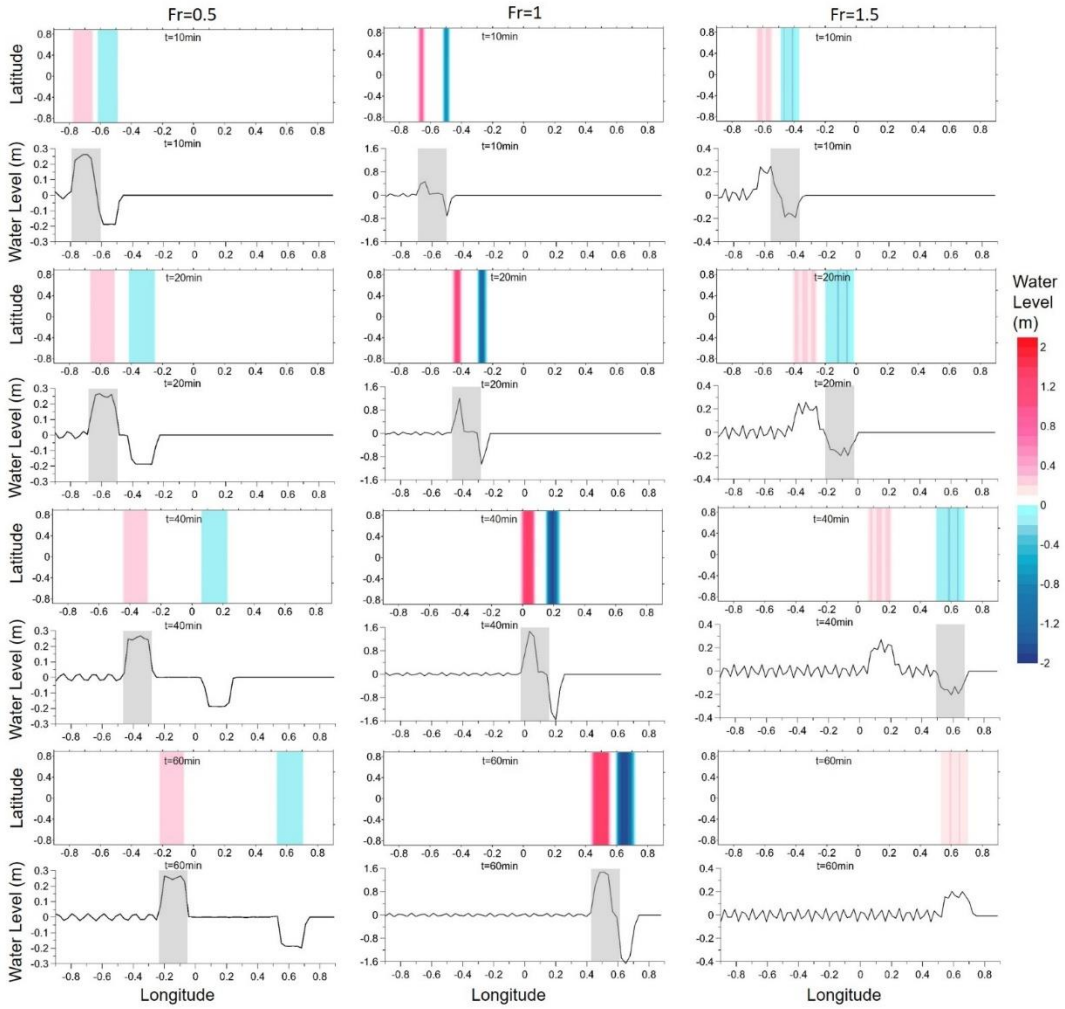

Figure 4.3 The sea state at t = 10 min, 20 min, 40 min, 60 min for the pressure disturbance moving with 22 m/s (left column), 44 m/s (middle column) and 66 m/s speed (right column) over 200 m deep flat bottom basin. Rows 1, 3, 5 and 7 show top view; rows 2, 4, 6 and 8 show the sectional view of the water surface at zero latitude (note, vertical scales of sectional views are different). The grey shaded area is the location of the pressure disturbance band at the respective time.

To verify the accuracy of the numerical model, the simulations were performed for six different Froude numbers. The ratios of the amplitude of the free wave (determined by the wave celerity) to the amplitude of the forced wave (determined by the speed of pressure disturbance) were computed and compared with the analytical predictions (Table 4.1). The comparisons show that the majority of the % Error (the ratio of the absolute difference between numerical results and the corresponding analytical results) for each Fr is less than 1%. Furthermore, the same simulations were performed using different grid sizes of 50 m, 100 m, 177 m, 354 m and 708 m for the sensitivity analysis due to the grid size. The numerical results for $Fr = 1$ indicated that no significant difference occurred with changing grid size in the range of used resolution with a % Error of less than 1.5%.

Table 4.1 Amplitude ratios (Q/P) of the numerical and analytical results for 200 m deep flat bottom basin ($c = 44.3$ m/s, grid size $dx = 177$ m and $f_b = 0$).

Speed of Pressure Disturbance V (m/s)	**Fr**	**Absolute ratio of the amplitudes of free wave to forced wave**		**% Error**
		Analytical	**Numerical**	
11	0.25	0.624	0.622	0.3%
22	0.5	0.748	0.752	0.5%
33	0.75	0.873	0.877	0.5%
44	1	1	0.999	0.1%
55	1.25	1.121	1.114	0.6%
66	1.5	1.245	1.272	2.1%

4.3 Numerical Tests for Different Types of Basins

The investigation of the long wave generation and propagation due to the moving pressure disturbance with a constant speed is important to understand considering the possible wave amplification at shallow regions in relation to bathymetric and morphologic conditions in basins and/or marine environment. In this direction, three different basins were selected for applications with different cross-sections in lateral or longitudinal directions with respect to directions of pressure disturbance and

ocean wave; (i) triangular lateral cross-section, (ii) stepwise shelf from 200 m to 20 m of depth on 1:10 slope in the longitudinal direction, and (iii) stepwise shelf from 200 m to 20 m of depth on 1:700 slope in the longitudinal direction. Additionally, similar stepwise shelf basins on slopes varying from 1:100 to 1:600 were simulated to expand the numerical tests over different slopes.

4.3.1 Simulations in the Basin with Triangular Cross-section

The basin with a triangular cross-section has a 200 m water depth at the center along the direction of pressure disturbance with 1:444 side slopes. The top and sectional views of the basin are given in Figure 4.4. According to Equation 4.10, the representative wave celerity of this basin becomes 31.3 m/s, which was calculated with a reference depth of 100 m and $m_a = 1$. Simulations were performed using three different speeds of the pressure disturbance (22 m/s, 31 m/s and 44 m/s) or Fr (0.7, 1, and 1.4) propagating over the basin with the triangular cross-section.

The distributions of water surface (sea states) and sectional views at zero latitude at selected time steps (t = 10 min, 20 min, 40 min and 60 min) under the moving pressure disturbance with 22 m/s, 31 m/s and 44 m/s speeds in the basin with triangular cross-section are presented in Figure 4.5.

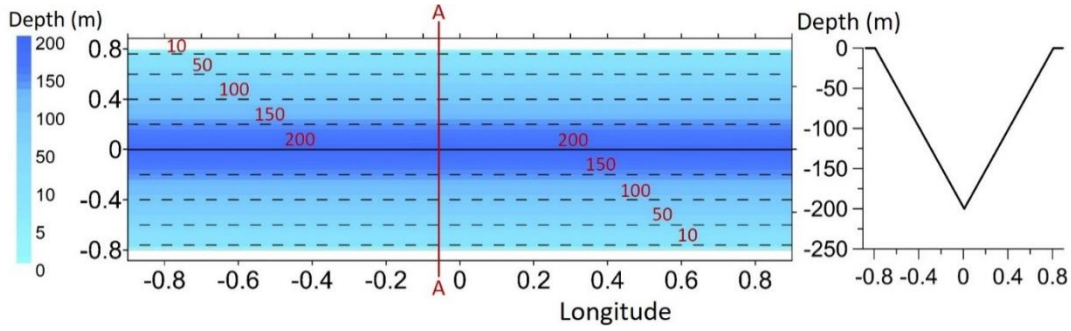

Figure 4.4 Top and sectional (along section A-A) views of the triangular basin.

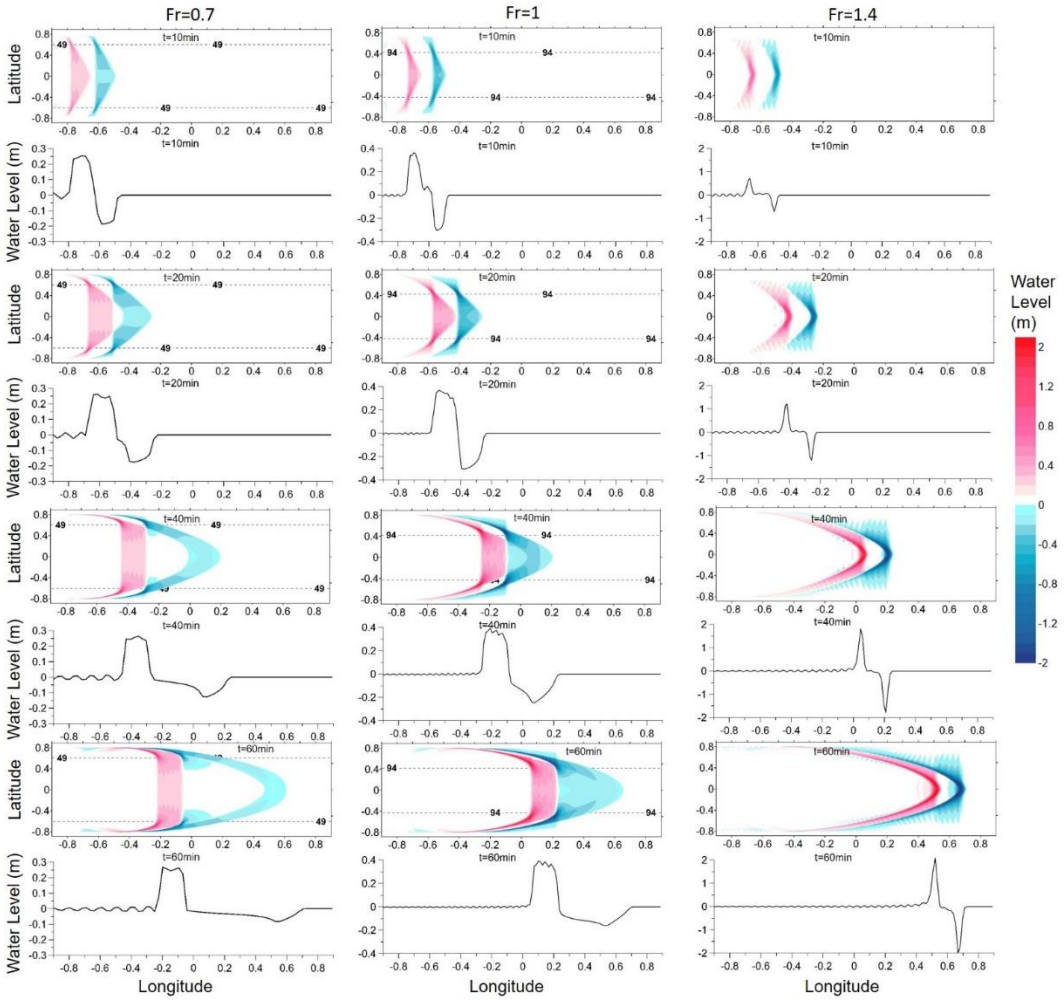

Figure 4.5 The sea state at t = 10 min, 20 min, 40 min, 60 min for the pressure disturbance moving with the speed of 22 m/s (left column), 31 m/s (middle column) and 44 m/s (right column) in the basin with the triangular cross-section. Rows 1, 3, 5 and 7 show top views; rows 2, 4, 6 and 8 show sectional views of the water surface at zero latitude (note, vertical scales of sectional views are different). The black dashed lines show water depths of 49 m in the first, 94 m in the second and 200 m in the last column.

For three different speeds of pressure disturbance, the maximum wave amplification was observed for the case of 44 m/s speed of pressure disturbance at 200 m depth, the deepest part (along the central axis) of the basin. A similar wave amplification was observed for the case of 31 m/s speed of the pressure disturbance, which

coincides with the corresponding speed of the free wave at about 94 m water depth. In the case of V = 22 m/s, the extrema of positive and negative amplitudes were less compared to the other two cases observed at a depth of ~49 m.

4.3.2 Simulations in the Basin with Shelf Bathymetry

Several different basins with stepwise shelf bathymetry were used for the other sets of simulations. The selected basins were composed of three parts as; i) 200 m deep (h_1) flat bottom, ii) a sloping connection from 200 m depth to 20 m depth, and iii) 20 m deep (h_2) flat bottom (Figure 4.8 and Figure 4.10). The slopes considered in section (ii) were selected as 1:10 and 1:700 for two different cases. As before, the basins at the Northern (top) and the Southern (bottom) boundaries were used as solid impermeable boundaries to prevent the lateral escape of energy from these boundaries. The East and West borders were open (outgoing) boundaries. The simulations were carried out using three different speeds of pressure disturbance (22 m/s, 31 m/s and 44 m/s) propagating over the basins with stepwise shelf bathymetry. The results for the two different basins are given in the following sections. In addition, six different slopes varying from 1:100 to 1:600 were also numerically tested for 31 m/s speed of pressure disturbance to elaborate on the effect of slope in section (ii) on wave amplification. The wave evolution, the water surface profile at zero latitude taken at different times along the x (propagation) direction in the flat bottom basin with the critical depth of 31 m/s moving pressure speed ($h_c = 100\ m$) is given in Figure 4.6 to provide a basis for the wave evolution at a constant depth. Here the wave amplitudes were normalized with the $\eta_0 = \Delta P/\rho g$ value which corresponds to the water level change due to static pressure gradient to obtain the dimensionless wave amplification. As can be seen in Figure 4.6, the wave amplitude increases up to a point and then reaches a nearly steady state.

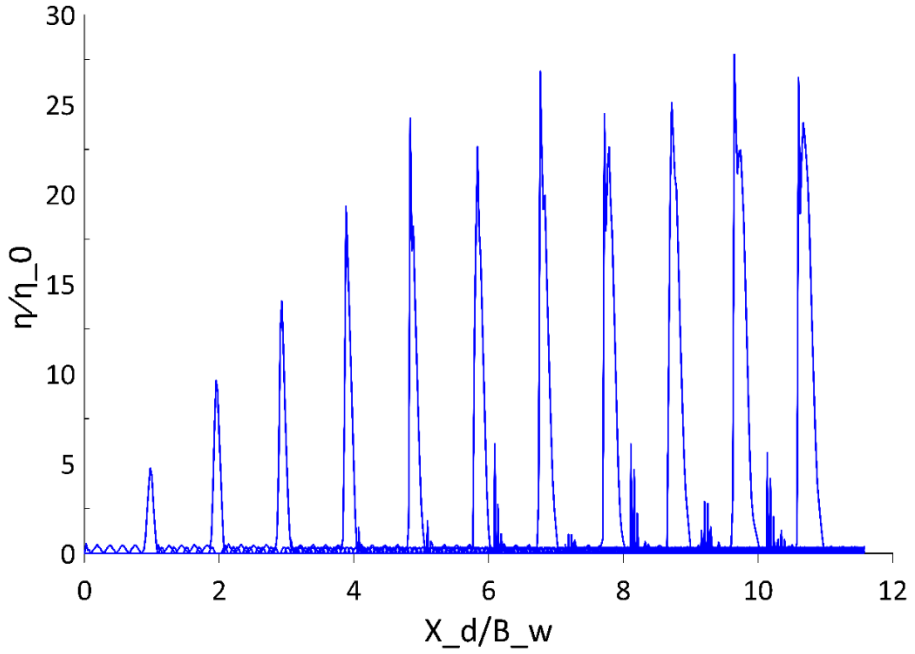

Figure 4.6 Normalised water surface elevation along zero latitude for $V = c = 31\ m/s$ in 100 m constant depth basin

The results of the simulations given in Table 4.2 show that as the slope becomes milder, there is an increase in the extrema of the positive and negative wave amplitudes during the 120 min simulation (the row indicated with a star symbol in Table 4.2). The amplification in the amplitudes of the depression (front part) and the elevation (rear part) waves is also higher for a milder slope but observed at different time steps of the simulation or different locations along the basin depending on the location of the slope. Then, the envelopes of the peak amplitudes, which show the variation of the maximum water elevation along the basin in the propagation direction, were plotted and presented in Figure 4.7. The peak amplitudes (η_{peak}) were normalised by the static pressure induced amplitude value (η_0) as it propagates along the basins with different shelf slopes, and presented with respect to the distance traveled by the pressure disturbance (X_d) normalised by the bandwidth of the disturbance (B_w), i.e., wavelengths traveled. As can be seen in Figure 4.7a, the Proudman resonant wave in the case of 100 m constant depth greatly differs from the other cases. The water level shows a steady response at 200 m depth to the

pressure disturbance traveling at a speed of 31 m/s, whereas the wave amplification is clearly observed in the case of the sloping section of the basin. There is a delay in the wave amplification as the slope goes milder, but the total amplification is higher in those cases. This situation was further investigated and the observations from additional numerical tests are discussed in Chapter 4.3.3.

Table 4.2 Negative and positive amplitudes of the wave at different time steps for different slopes (from 200 m to 20 m water depths) of the stepwise shelf bathymetry for the case of $V = 31$ m/s speed of pressure disturbance moving over the basin.

Time (min)	**Amplitude of the depression part of the wave (m)**							
	1:10	**1:100**	**1:200**	**1:300**	**1:400**	**1:500**	**1:600**	**1:700**
10	-0.377	-0.377	-0.377	-0.377	-0.377	-0.377	-0.377	-0.377
20	-0.612	-0.397	-0.386	-0.383	-0.382	-0.381	-0.380	-0.380
40	**-0.669**	**-0.742**	-0.696	-0.530	-0.477	-0.451	-0.436	-0.427
60	-0.605	-0.670	**-0.738**	**-0.874**	**-1.052**	**-1.118**	-0.977	-0.739
90	-0.621	-0.694	-0.698	-0.747	-0.743	-0.936	**-1.278**	**-1.463**
110	-0.613	-0.686	-0.696	-0.733	-0.723	-0.770	-0.862	-1.338
*	-0.675	-0.787	-0.794	-0.966	-1.141	-1.292	-1.396	-1.471
Amplitude of the elevation (peak) part of the wave (m)								
10	0.453	0.453	0.453	0.453	0.452	0.452	0.453	0.453
20	0.452	0.452	0.452	0.452	0.452	0.452	0.452	0.452
40	0.898	0.774	0.523	0.499	0.470	0.466	0.463	0.462
60	**1.063**	**1.178**	**1.254**	**1.419**	1.289	1.048	0.871	0.780
90	1.003	1.104	1.168	1.396	**1.652**	**1.918**	1.989	2.022
110	0.991	1.096	1.116	1.358	1.588	1.826	**1.990**	**2.079**
*	1.073	1.227	1.354	1.620	1.833	2.016	2.171	2.269

*Extrema of the positive and negative wave amplitudes during the 120 min simulation

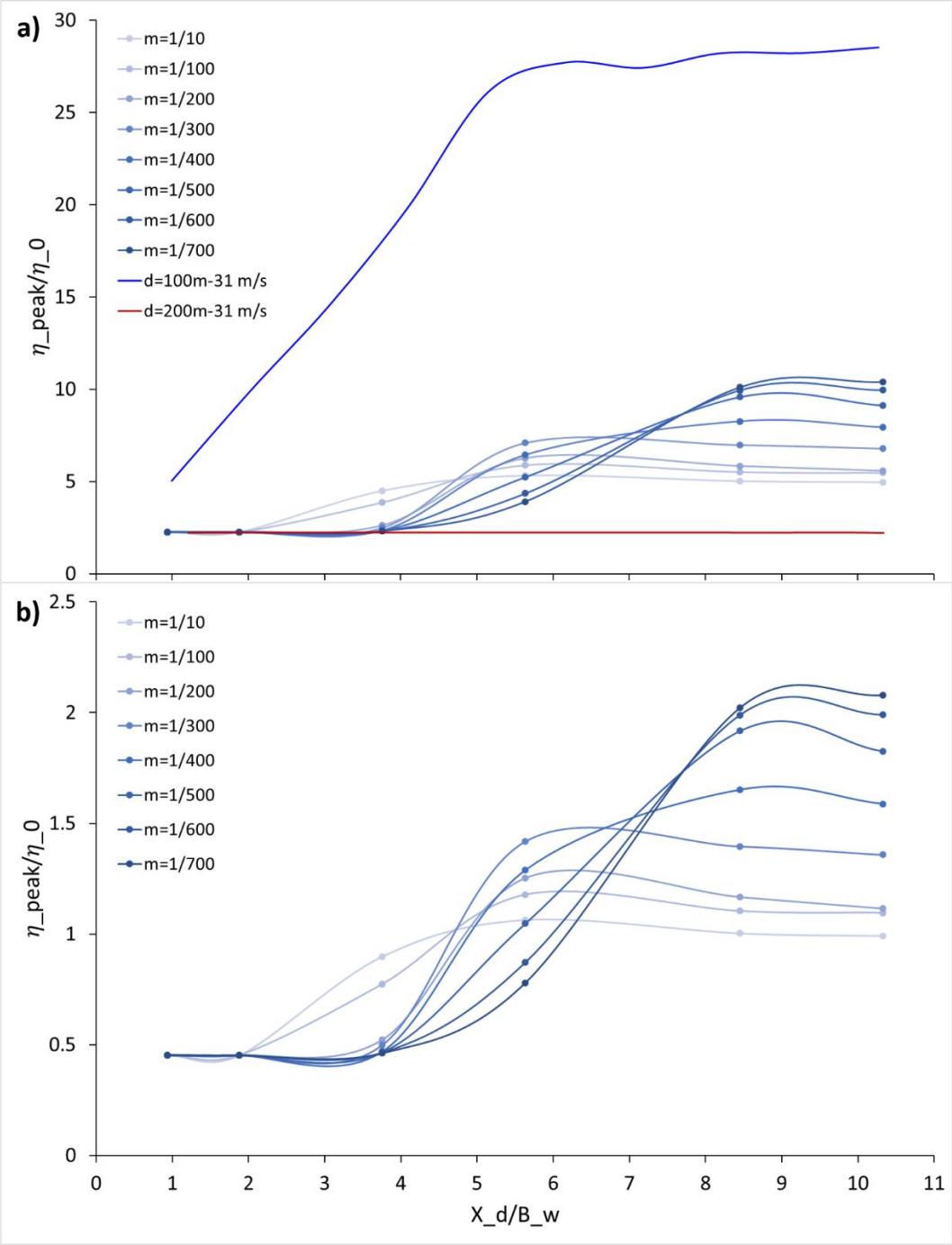

Figure 4.7 Normalised peak amplitudes as the distance traveled, computed from the simulations V = 31 m/s pressure speed moving over the basin with different shelf slopes, a) including the cases of flat bottom with 100 m constant depth (h_c for 31 m/s) and 200 m constant depth (h_1), b) closer view of the simulation results for shelf bathymetry basins with different slopes

4.3.2.1 Shelf Bathymetry with 1:10 Shelf Slope

The top and sectional views of the stepwise shelf bathymetry with 1:10 shelf slope are shown in Figure 4.8. The simulations were performed using three different speeds of pressure disturbance (22 m/s, 31 m/s and 44 m/s) propagating over this basin from the left (West) to the right (East).

The distributions of water surface (sea states) and sectional views at zero latitude at selected time steps (t = 10 min, 20 min, 40 min, 60 min and 90 min) for three different speeds of pressure disturbance moving over the stepwise shelf bathymetry with 1:10 shelf slope are presented in Figure 4.9.

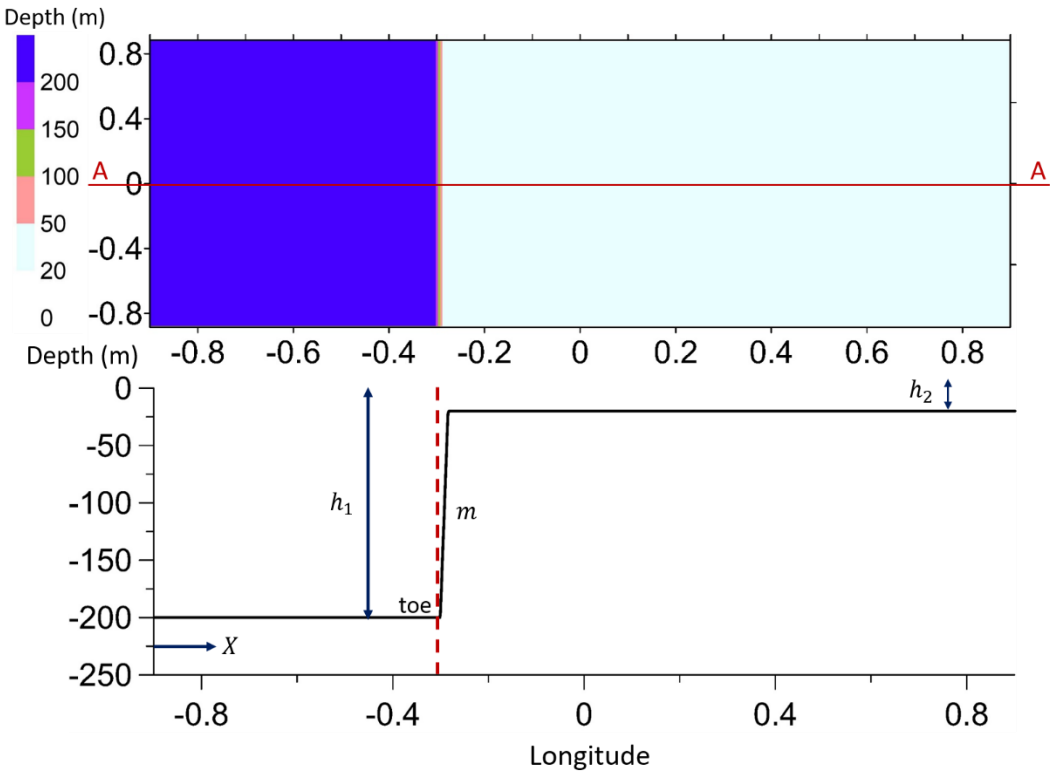

Figure 4.8 Top and sectional (section A-A) views of the stepwise shelf bathymetry with 1:10 shelf slope from 200 m (h_1) to 20 m (h_2) water depths.

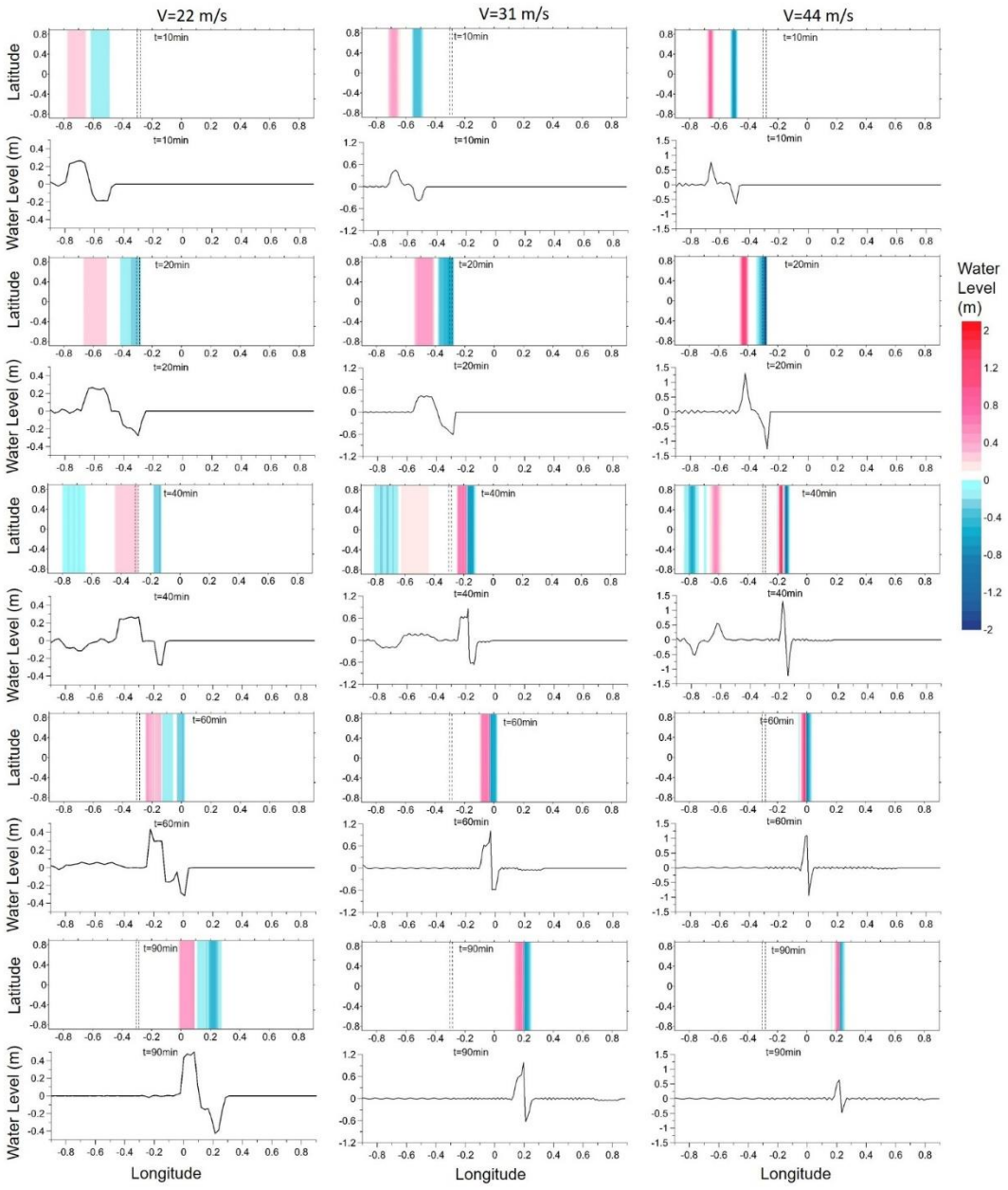

Figure 4.9 The sea state at t = 10 min, 20 min, 40 min, 60 min, 90 min for the pressure disturbance moving with the speed of 22 m/s (left column), 31 m/s (middle column) and 44 m/s (right column) over the stepwise shelf bathymetry with 1:10 shelf slope. The dashed lines show the sloping section of the basin. Rows 1, 3, 5, 7 and 9 show top view; rows 2, 4, 6, 8 and 10 show sectional views of the water surface at zero latitude (note, vertical scales of sectional views are different). Dashed lines indicate the location of the toe (left) and top (right) of the sloping section of the shelf.

Negative and positive amplitudes of the front and rear parts of the generated wave at different time steps for three different speeds of pressure disturbance are also given in Table 4.3.

Table 4.3 Negative and positive amplitudes of the wave at different time steps for three different speeds of pressure disturbance moving over the stepwise shelf bathymetry with 1:10 shelf slope from 200 m to 20 m water depths.

Time (min)	**Wave Amplitude (m)**					
	***V* = 22 m/s**		***V* = 31 m/s**		***V* = 44 m/s**	
	Depression, front part of the wave	Elevation, rear part of the wave	Depression, front part of the wave	Elevation, rear part of the wave	Depression, front part of the wave	Elevation, rear part of the wave
10	-0.188	0.268	-0.377	0.453	-0.795	0.832
20	-0.191	0.267	-0.612	0.452	-1.306	1.320
40	-0.232	0.277	-0.669	0.898	-1.217	1.280
60	-0.245	0.301	-0.605	1.063	-0.930	1.070
90	-0.420	0.521	-0.621	1.003	-0.533	0.596

The simulations for the case of V = 22 m/s speed of pressure disturbance (Figure 4.9 and Table 4.3) give a negative wave amplitude changing from -0.188 m to -0.420 m and a positive wave amplitude from 0.268 m to 0.521 m during the 90 min of wave propagation in the basin. In the case of V = 31 m/s, the negative amplitude of the wave changes from -0.377 m to -0.621 m and the positive amplitude of the wave changes from 0.453 m to 1.003 m for 90 min of wave propagation in the basin. Furthermore, the obtained values in the case of V = 44 m/s show that the negative amplitude of the wave changes from -0.795 m to -0.533 m, and the positive amplitude of the wave changes from 0.832 m to 0.596 m during the 90 min of simulation. However, at around 20 min, the negative amplitude shows the lowest minimum (-1.306 m) as the front of the wave arrives the shelf, and the positive amplitude shows the highest maximum (1.320 m) for V = 44 m/s, which satisfies the Proudman resonance in the deep (left) part of the basin while approaching the shelf slope.

4.3.2.2 Shelf Bathymetry with 1:700 Shelf Slope

The top and sectional views of the stepwise shelf bathymetry with 1:700 shelf slope are shown in Figure 4.10. The simulations were performed using three different speeds of the pressure disturbance (22 m/s, 31 m/s and 44 m/s) propagating over this basin from the left (West) to the right (East).

The distributions of water surface (sea states) and sectional views at zero latitude at selected time steps (t = 10 min, 20 min, 40 min, 60 min and 90 min) for three different speeds of the pressure disturbance, moving over the stepwise shelf bathymetry with 1:700 shelf slope from 200 m to 20 m water depths are presented in Figure 4.11. The negative and positive amplitudes of the front and rear parts of the generated waves at different time steps for three different speeds of the pressure disturbance are given in Table 4.4.

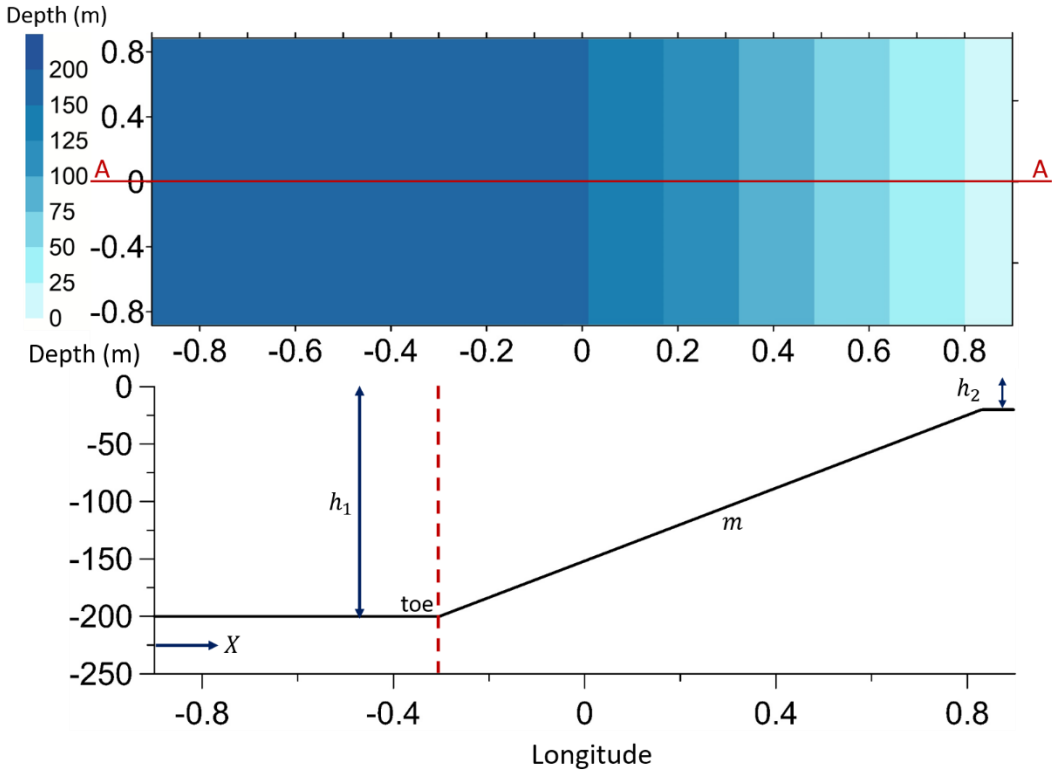

Figure 4.10 Top and sectional (section A-A) views of the stepwise shelf bathymetry with 1:700 shelf slope from 200 m (h_1) to 20 m (h_2) water depths.

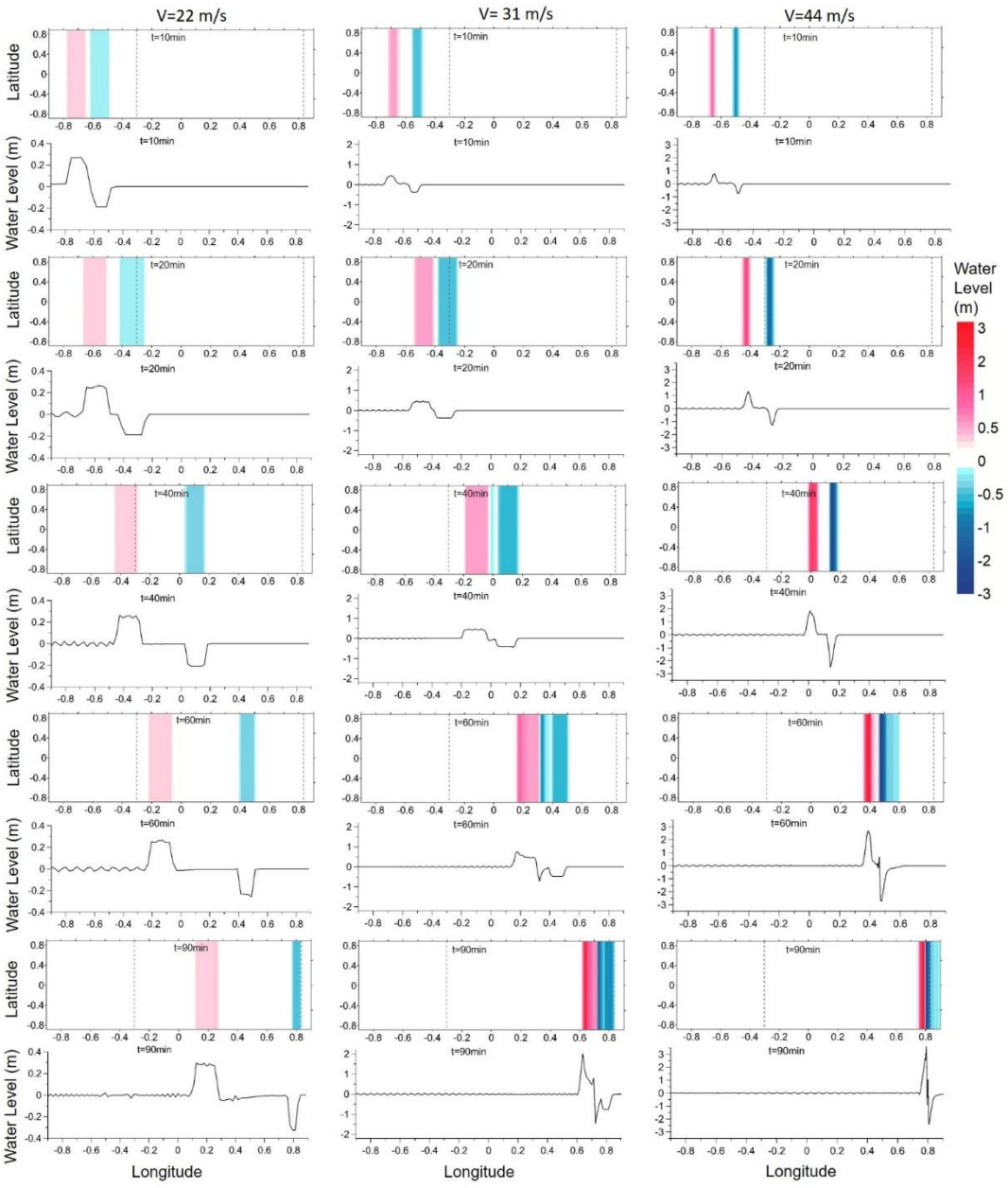

Figure 4.11 The sea state at t = 10 min, 20 min, 40 min, 60 min, 90 min for V = 22 m/s (left column), 31 m/s (middle column) and 44 m/s (right column) over the stepwise shelf bathymetry with 1:700 shelf slope. The dashed lines show the sloping section of the basin. Rows 1, 3, 5, 7 and 9 show top view; rows 2, 4, 6, 8 and 10 show sectional views of the water surface at zero latitude (note, vertical scales of sectional views are different). Dashed lines indicate the location of the toe (left) and top (right) of the sloping section of the shelf.

Table 4.4 The negative and positive amplitudes of the wave at different time steps for three different speeds of pressure disturbance over the stepwise shelf bathymetry with 1:700 shelf slope from 200 m to 20 m water depths.

Time (min)	**Wave Amplitude (m)**					
	***V* = 22 m/s**		***V* = 31 m/s**		***V* = 44 m/s**	
	Depression part of the wave	Elevation part of the wave	Depression part of the wave	Elevation part of the wave	Depression part of the wave	Elevation part of the wave
10	-0.186	0.253	-0.377	0.453	-0.780	0.828
20	-0.186	0.255	-0.380	0.452	-1.342	1.323
40	-0.208	0.251	-0.427	0.462	-2.480	1.825
60	-0.238	0.253	-0.739	0.780	-2.709	2.693
90	-0.320	0.281	-1.463	2.022	-2.385	3.552

The modeling results presented in Figure 4.11 and Table 4.4 show that in the case of $V = 22$ m/s speed of pressure disturbance, the negative amplitude of the wave changes from -0.186 m to -0.320 m and the positive amplitude of the wave changes from 0.253 m to 0.281 m during 90 min of the wave propagation in the basin. In the case of $V = 31$ m/s, the negative amplitude of the wave changes from -0.377 m to -1.463 m, and the positive amplitude of the wave changes from 0.453 m to 2.022 m. The results obtained for the case of $V = 44$ m/s also indicate a negative wave amplitude changing from -0.780 m to -2.385 m and a positive wave amplitude changing from 0.828 m to 3.552 m. In this case, at around 60 min, the negative amplitude exhibits the lowest minimum (-2.709 m), whereas the positive amplitude has the highest maximum at around 90 min (3.552 m). In the stepwise shelf bathymetry with a 1:700 slope basin, the maximum wave amplification was observed for the case of $V = 44$ m/s, which satisfies the Proudman resonance in the deep (left) part of the basin while approaching the shelf slope. In other words, the same speeds of pressure disturbance and the wave celerity in the deep (left) part of the basin caused larger amplification of the wave before arriving at the shelf. Furthermore, a higher wave amplification was observed as the wave reached the top (end) of the sloping section in the East direction. In the stepwise shelf bathymetry with a 1:700

slope basin, the resulting amplitude change was not significant in the case of 22 m/s speed of pressure disturbance.

When the results given in Table 4.3 and Table 4.4 are compared, it can be roughly inferred that the milder shelf slopes can cause higher wave amplification.

4.3.3 Wave Amplification in the Basin with Shelf Bathymetry

For further investigation of wave amplification in basins with shelf bathymetry, the effect of one of the major oceanographic factors, the shelf slope, and the hydrodynamic factors, the average traveling speed of the atmospheric pressure were examined by expanding the number of numerical tests. The available studies have considered constant depth or uniform shore slope cases, but in reality, the basins have a nearly flat part in the deep ocean where the wave grows and amplifies depending on the location and path of the atmospheric system, a following shelf slope where the wave further amplifies and again a very mild slope or nearly flat part before the landing. Therefore, the basins with shelf bathymetry (explained in Chapter 4.3.2) with 23 different slopes (m) of 1:10 to 1:700 to cover a range of slopes from steep to mild ones were considered in the numerical tests. The basin length was taken as 250 km in total, 60 km of which was before the sloping section. The average traveling pressure speeds (V) were selected as 7.0, 9.9, 14.0, 17.2, 19.8, 22.1, 27.1, 31.3, 32.8, 35.7, 38.4, 40.8 and 44.3 m/s to cover a wide range of corresponding critical depths ($h_c = {V^2}/{g}$), which can be defined as the depth where the Proudman resonance condition is achieved, i.e., Froude number is equal to 1. The numerical tests were performed for each shelf slope-pressure speed pair with a grid size of 100 m and the pressure drop of 20 hPa (ΔP) having a 20 km bandwidth (B_w) was inputted at every minute (Figure 4.2).

First, the variation of the maximum water elevations, i.e., the envelopes of the instantaneous peak amplitudes, along the basins in the propagation direction (East) for the selected eight shelf slopes (represented by lines with different colors) is

presented in Figure 4.7. The graph clearly shows the larger wave amplification achieved in milder slopes with increasing local maximum. The local maximum of the envelopes tends to occur after the sloping section in the steeper slopes up to $m{\sim}1{:}\,300$. Then, the location of the maximum changes to occur in the sloping section, much farther (earlier) from the sloping end as the slope is milder. The primary factor affecting the observed waveforms is the separation point of the forcing and the wave as the instantaneous peak amplitudes decrease after the separation from the pressure disturbance. Here, the local water depth decreases from 200 m to 20 m over the sloping section and the wave celerity decreases with the shallower depths and reaches 14 m/s after the sloping section. However, the pressure travels at 44.3 m/s and Fr increases from 1 to 3.16, whereas the Proudman resonant wave would show a huge amplification approaching the end of the basin, as shown with the black line in Figure 4.12. However, the global maximum is smaller, which was obtained as $\eta_{peak}/\eta_0 = 18.6$ for $m = 1{:}\,700$ at $Fr = 1.8$, or depth of 62.2 m, revealing that the condition of $Fr = 1$ may not be the simple prediction method for the maximum amplification in basins with shelf bathymetries.

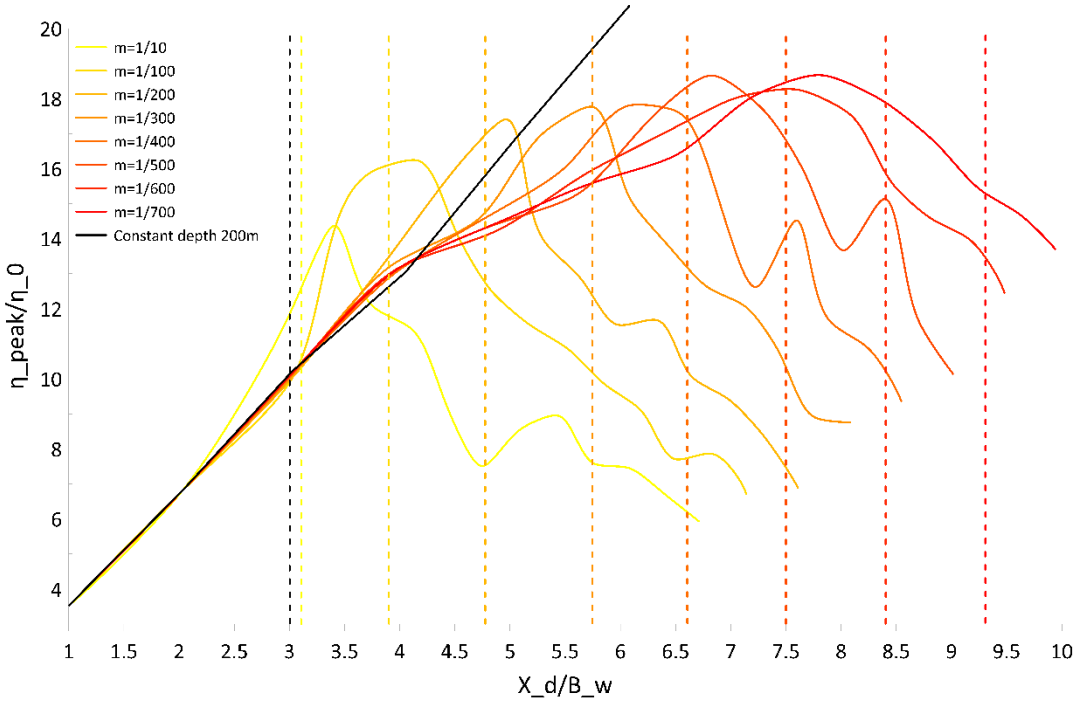

Figure 4.12 Normalised peak amplitudes as the distance traveled over the shelf bathymetries with different slopes, computed from the simulations with $V = 44.3\, m/s$ pressure speed moving over the basin. The black line shows the flat bottom case with 200 m depth (h_c).

Then, the maximum positive wave amplitude, η_{max}, attained in each simulation was extracted and normalized with η_0 which corresponds to the envelopes of the local extrema of the curves given in Figure 4.12. Figure 4.13 shows the wave amplification in the basins with different shelf slopes for each traveling pressure speed. As the graphs imply, the highest amplification is achieved in the case of the largest pressure speed, 44.3 m/s, which is due to the more favorable Proudman resonance conditions achieved earlier than the other speed cases, i.e., longer traveling distance or sufficient time for the wave growth and amplification. At the two lowest speeds, the slope effect on the wave amplification is almost negligible. The reason is the resonance conditions have never been reached for those two cases. For the other cases, as the speed increases, the wave amplification increases, except in the case of 14 m/s. The reason why the 14 m/s traveling speed shows an opposite pattern is the large wave

amplification in the post-slope part of the basin, 20 m depth, due to achieving the Proudman resonance condition at this depth which is equal to h_c. For this case, the wave arrives at h_c earlier in the steeper slopes and the resonant wave grows more than in milder slopes. A similar pattern can also be observed in the case of 17.2 m/s because it also undergoes a Proudman-like resonance condition, although the resonance condition is not strictly ensured. Here, the results reveal that the two parameters, the water depths before (h_1) and after (h_2) the sloping section (Figure 4.10) are as important as the shelf slope. Hence, a dimensionless parameter, h_1/h_2, should be considered and tested for a good number of tests for a more holistic analysis. However, this issue has been left as an open question for further research.

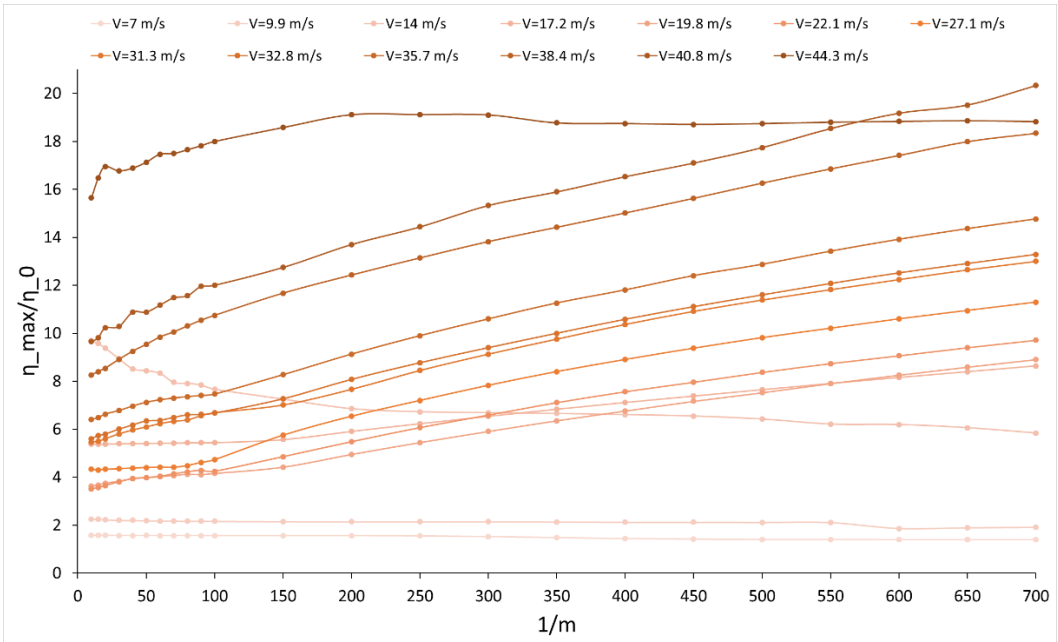

Figure 4.13 Normalized maximum positive wave amplitude with respect to the shelf slope (from 200 m to 20 m) obtained from simulations for different traveling pressure speeds.

Another important process affecting the observed wave amplitudes is the wave reflection from the shelf slope. In other words, before examining the maximum amplitude attained in any simulation, evaluating the situation at the toe of the sloping section can be considered. In this regard, simulations performed for the pressure

speeds of 7-44.3 m/s in the flat bottom basin with a depth of 200 m were taken as the basis. The black curve in Figure 4.14a show the normalized maximum wave amplitude obtained for different pressure speeds at the corresponding grid of the toe location in the flat bottom basin (Figure 4.10). The amplitudes obtained from the simulations of the basins with different shelf slopes differ more than the base case (flat bottom) as the pressure speed increases. Furthermore, the values converge to the base case as the shelf slope becomes milder; that is why the values for milder slopes than 1:300 is not plotted in Figure 4.14a, whereas the steeper slopes show larger deviation due to more reflection, as expected. To quantify this, Root Mean Square Errors with respect to the base case were calculated for each slope and pressure speed and the results are presented in Figure 4.14b and Figure 4.14c.

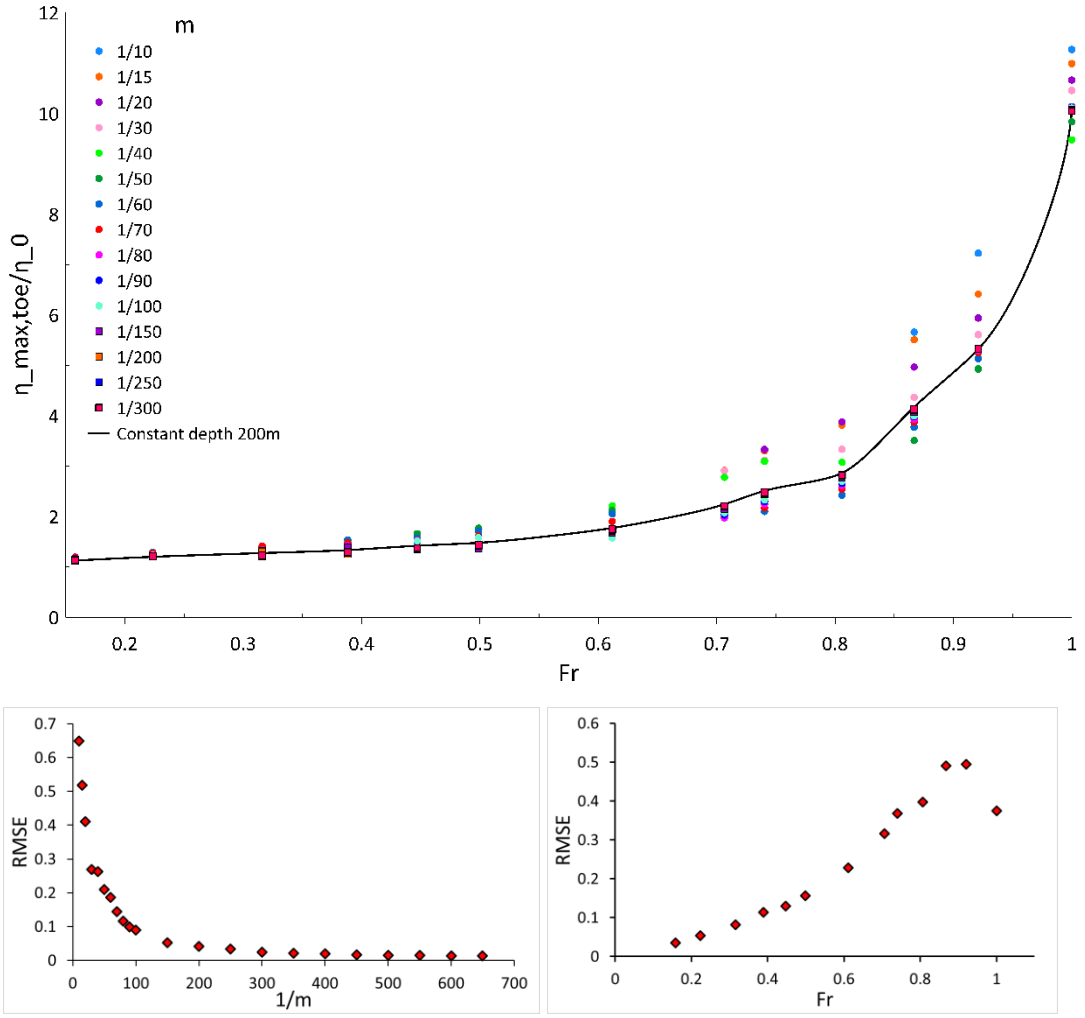

Figure 4.14 a) Normalised maximum positive amplitudes computed at the toe of the sloping section (pre-slope) for different shelf slopes changing with Fr, b), and c) RMSE values calculated for each slope and each pressure speed, respectively. Each Fr refers to a moving pressure speed, calculated based on 44.3 m/s which corresponds to the critical water depth of 200 m, the depth at the pre-slope section of the basin. The black line in (a) is the computed curve for different pressure speeds in the flat bottom basin with a constant depth of 200 m.

Then, the curves for the maximum wave amplitudes attained in each simulation normalized by the amplitudes computed at the toe of the sloping section for different pressure speeds are presented in Figure 4.15, changing with the shelf slope. The graph shows that the complexity is higher in the steeper shelf slopes, while the curves show a more stable trend after $m{\sim}1:200$. It is important to note that those curves and calculated values are valid for certain conditions, ${h_1}/{h_2} = 10$, ${X_{toe}}/{B_w} = 3$, $\Delta P = 20$ hPa, and $X_{max}/B_w = 12.5$ (maximum wavelengths traveled), but still can be useful for similar settings or can be much further expanded.

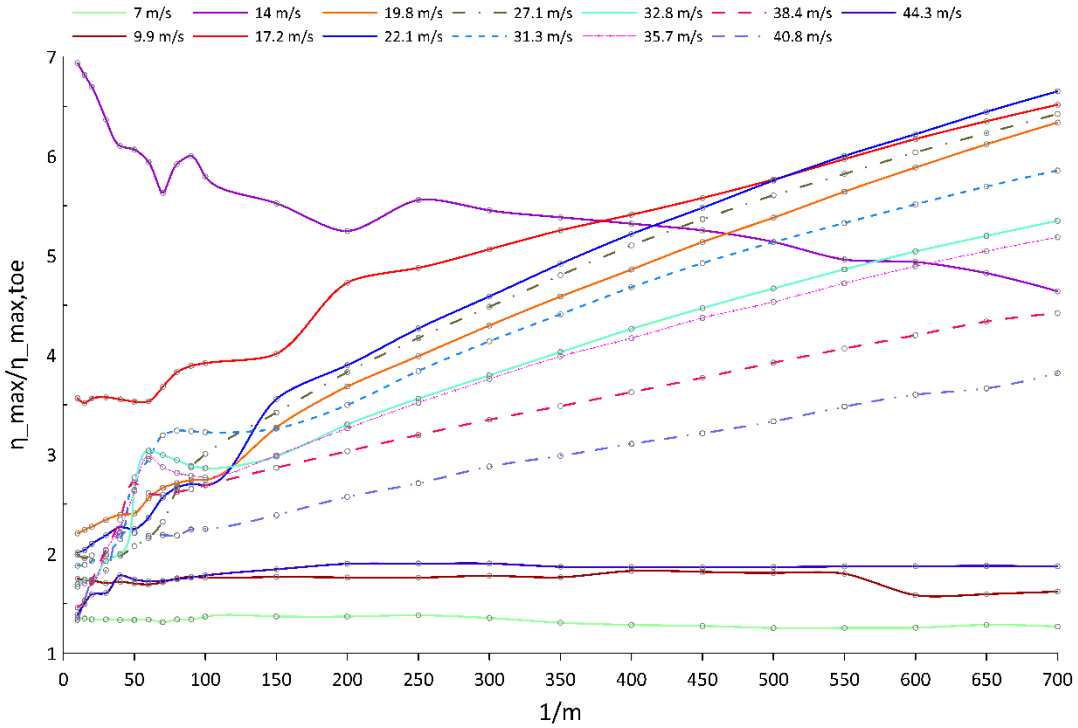

Figure 4.15 Maximum amplitude curves normalized by the maximum amplitudes at the toe of the sloping section for different pressure speeds changing with shelf slope.

4.4 Effect of Wind Parameters in Wave Amplification

Wind gusts accompanying the atmospheric pressure variations during the passage of cyclones, squall lines and such extreme events are the other contributing forcing mechanism in meteotsunami generation and may produce coastal amplification and inundation in coastal areas. A good amount of research can be found regarding the atmospheric pressure disturbances, whereas much less research has been put on the wind forcing and possible wave amplification factors. Therefore, in this part, I focused on the examination of the moving wind fields and related long wave generation and the possible hydrodynamic factors to understand their contribution on the wave amplification, thinking it is worth providing a small discussion on that issue.

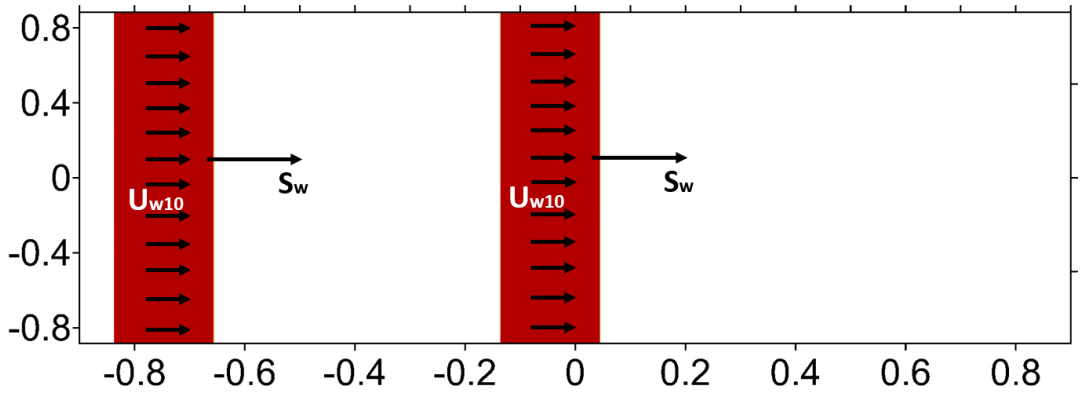

Figure 4.16 Moving wind fields in the flat bottom basin with a 50 m depth

There can be at least three main features of the moving wind fields affecting the generation and amplification of coastal waves; wind speed (U_{w10}), the average moving speed of the wind field (S_w), and wind drag coefficient (C_d). More than 200 numerical tests were conducted in a 50 m depth flat basin to investigate the generated wave response to a moving wind field of 20 km width and rectangular cross-sectional area (Figure 4.16). First, the wind speed (U_{w10}) was taken as constant for five different values of 11 m/s, 22.1 m/s, 33.2 m/s, 44.3 m/s and 55.4 m/s, and the moving wind speed was varied from 4.4 m/s to 66 m/s for 17 different values.

Figure 4.17 shows the maximum wave amplitude attained in each simulation (normalized with the water depth) changing with the moving speed of the wind field for five different wind speed values. Here, two options appear to calculate Fr: i) the ratio of the moving speed of the wind field and the long wave phase speed at 50 m water depth which is equal to 22.1 m/s ($Fr_S = {S_w}/{c}$), and ii) the ratio of the wind speed and the long wave phase speed ($Fr_U = {U_{w10}}/{c}$). As can be inferred from Figure 4.17, the local maximum for each case occurs at $Fr_S \sim 1$, regardless of the wind speed. On the other hand, the local maximum increases with the increasing wind speed up to 44.3 m/s but then decreases, which means that the global maximum was obtained at $Fr_U \sim 2$.

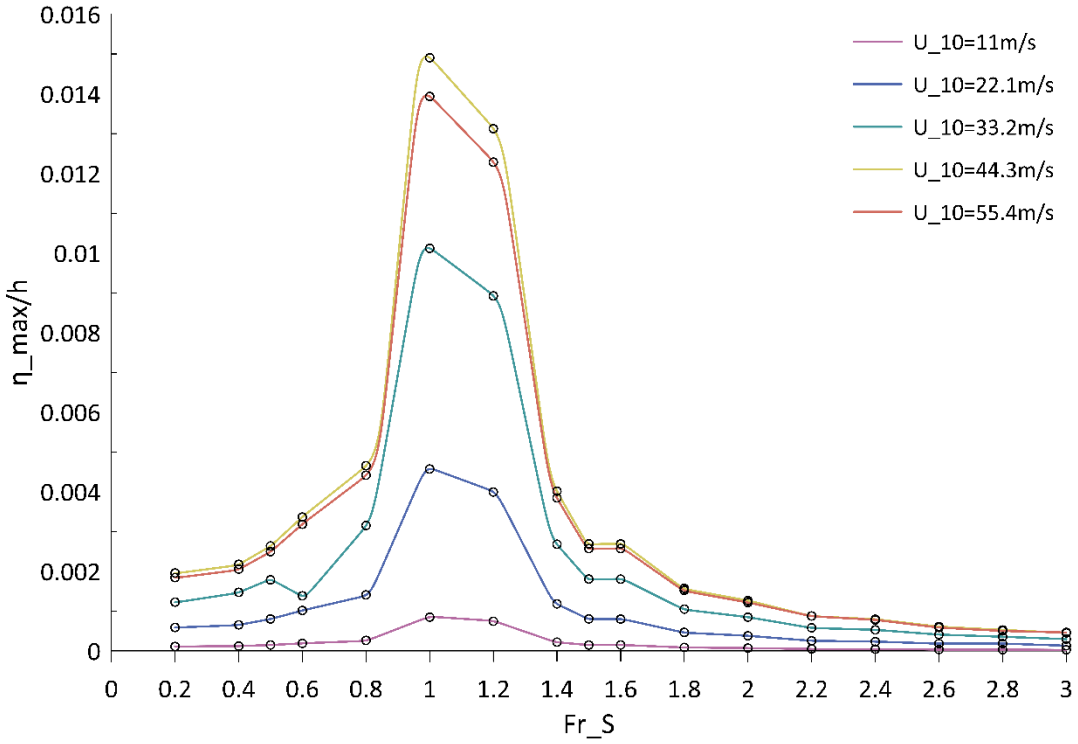

Figure 4.17 Maximum wave amplitude changing with Froude number (Fr_S) for different constant wind speed (U_{w10}) cases

Second, the moving wind speed was taken as $S_w = 22.1$ m/s ($Fr_S = 1$) and the wind speed (U_{w10}) was varied between 4.4 m/s and 66 m/s, which corresponds to different Fr_U values from 0.2 to 3. These tests were conducted for three different wind drag coefficient formulations available in the literature to examine the effect of the wind drag coefficient (C_d) on the sea level response and the simulation results are presented in Figure 4.18. As the graphs imply, the computed water levels are highly dependent on the wind drag coefficient formulation, which changes the observation of the global maximum occurring at $Fr_U \sim 2$, as speculated previously, because the model uses the C_{d1} formulation as default. The suppression of the maximum wave amplitude after $Fr_U \sim 2$ (black dots in Figure 4.18) obtained by using the C_{d1} formulation seems directly related with the wind drag coefficient approach. But in the other two cases, the maximum amplitude increases as the wind speed increases at different rates. This reminds us that the wind drag coefficient approach used in the

modeling is significant and shares the dominance with the wind speed for a constant moving speed case. Applications of real cases to draw a conclusion on the performance of the three approaches on the wave amplitudes would be the ideal option, leaving it here as a point of further research.

The three different wind drag coefficient approaches utilized in the numerical tests are given in the following.

1. C_{d1} based on Garratt (1977) and Donelan (2004),

$$C_{d1} = \left(\min\left((0.75 + 0.067U_{10}), C_{d_{max}}, \max(4.34 - 0.061U_{w10}, 0.5)\right)\right) * 10^{-3} \tag{4.28}$$

where $C_{d_{max}} = 2$.

2. C_{d2} based on Garratt (1977) and Powell (2003; 2007)

$$C_{d2} = (0.75 + 0.067U_{w10}) * 10^{-3} \; for \; U_{w10} \leq 26 \; m/s \tag{4.29}$$

$$C_{d2} = 2.18 * 10^{-3} \; for \; U_{w10} > 26 \; m/s \tag{4.30}$$

3. C_{d3} the empirical formulation used in DELFT3D software based on Smith and Banke (1975).

$$C_{d3} = \begin{cases} C_d^A, \; U_{10} \leq U_{10}^A, \\ C_d^A + (C_d^B - C_d^C)\frac{U_{10} - U_{10}^A}{U_{10}^B - U_{10}^A}, \quad U_{10}^A \leq U_{10} \leq U_{10}^B, \\ C_d^B + (C_d^C - C_d^B)\frac{U_{10} - U_{10}^B}{U_{10}^C - U_{10}^B}, \quad U_{10}^B \leq U_{10} \leq U_{10}^C, \\ C_d^C, \quad U_{10}^C \leq U_{10}, \end{cases} \tag{4.31}$$

where the default values of the coefficients A, B, and C are as follows.

Table 4.5 Default values of the coefficients A, B, and C in DELFT3D

Breakpoints	**Drag coefficient C_{d3}**	**Wind speed U_{10} (m/s)**
A	0.00063	0
B	0.00723	100
C	0.00723	100

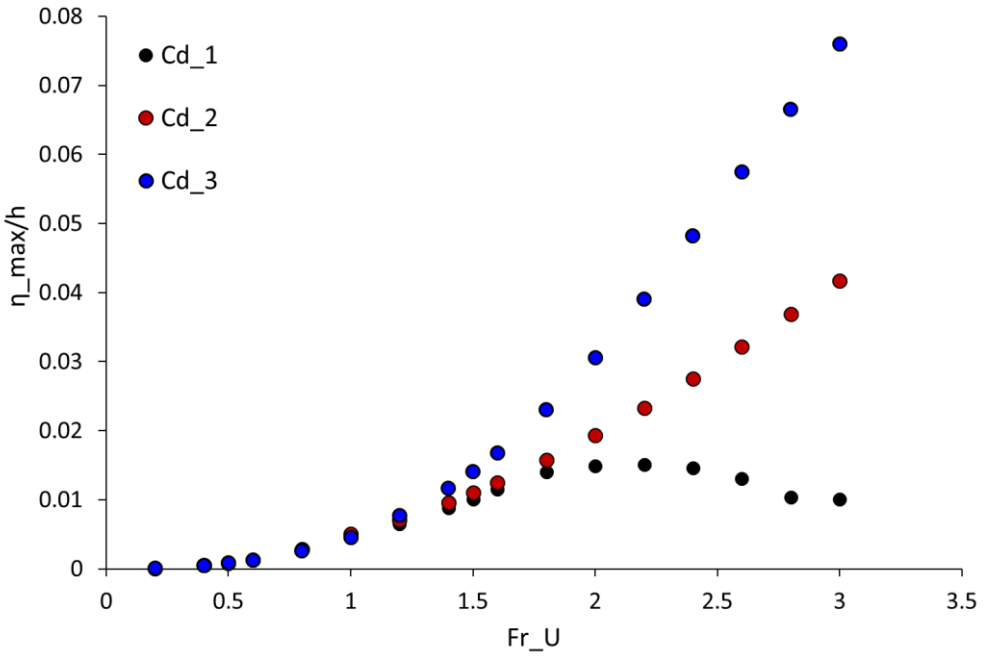

Figure 4.18 Maximum wave amplitude (normalized with water depth) changing with Froude number (Fr_U) for three different wind drag coefficient formulations applied

Furthermore, the effect of the shape of the moving wind field area (the input meteorological forcing function) was investigated. In most real cases, the wind speed reaches a peak value within a transition zone which can be assumed as a trapezoidal/rectangular forcing area, but there is an observation of almost triangular wind field observation for the 1954 Lake Michigan meteotsunamis (Figure 4.19, Bechle and Wu, 2014). Therefore, test simulations were performed for 12 different cases of $S_w = U_{w10}$ (from 5.5 m/s to 66.4 m/s) and $Fr = 0.25 - 3$. The simulation results are presented in Figure 4.19. In each case, the maximum wave amplitude was

reached in $Fr{\sim}1$ condition, which shows that in case of $S = U_{w10}$, the maximum wave amplification may depend on the Proudman resonance condition. The rectangular wind forcing resulted in higher wave amplitudes as expected, but there is not a constant ratio between the resulting amplitudes of the two different input forcing; the difference follows a similar trend.

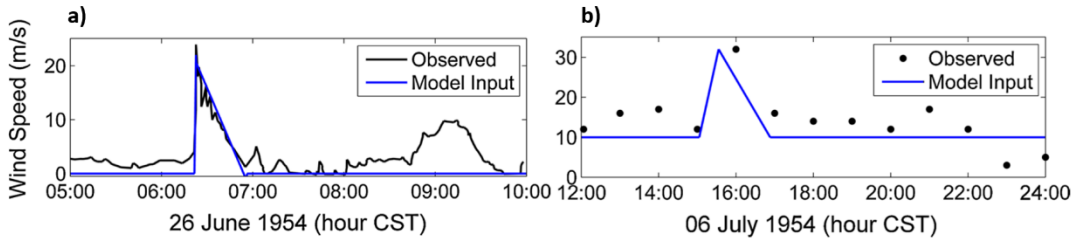

Figure 4.19 Observed wind records during a) June 26, 1954 at Wilson Avenue Crib station (taken from Platzman, 1958) and b) July 6, 1954 at Glenview Naval Air, IL station (taken from Donn and Ewing, 1956) and corresponding functions of meteorological forcing input for the hydrodynamic model of Bechle and Wu (2014).

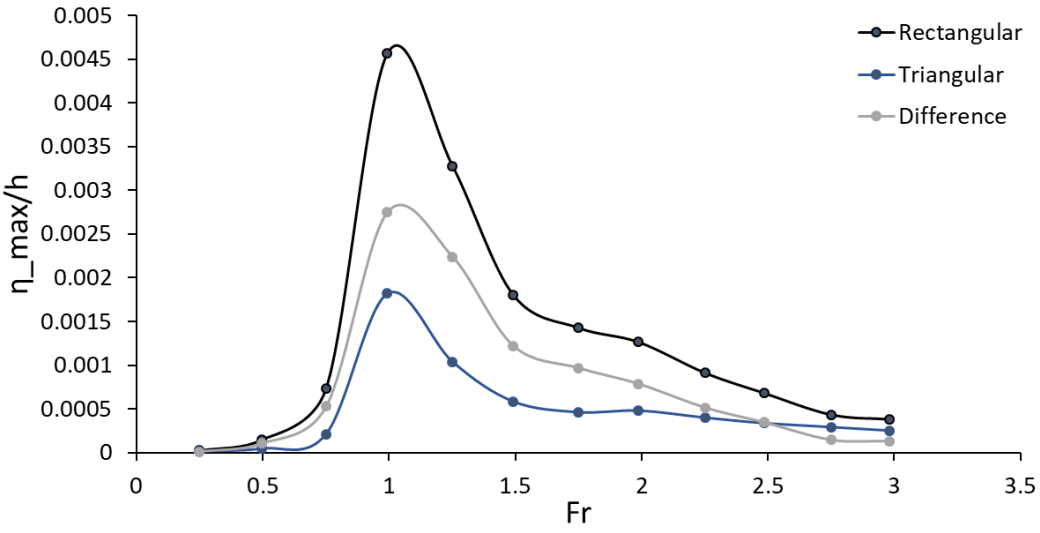

Figure 4.20 Maximum wave amplitude (normalized with water depth) changing with Fr for varying $S_w = U_{w10}$ conditions for rectangular and triangular wind input functions. The difference value for each maximum amplitude was calculated by $\frac{(\eta_{max,rectangular} - \eta_{max,triangular})}{h}$.

CHAPTER 5

GLOBAL PROPAGATION OF AIR PRESSURE WAVES AND CONSEQUENT TSUNAMI DUE TO 2022 TONGA VOLCANIC ERUPTION

The air pressure waves generated by the January 15, 2022 Hunga-Tonga Hunga Ha'apai (HTHH) eruption contained different wave categories according to their frequency and arrival time which are Lamb wave, acoustic wave and gravity wave (Nishiwaka et al. 2022). However, the Lamb wave, which is a long wave and the most prominent among those waves with the largest amplitude, is the main responsible for the generation of the pressure induced tsunami waves in the 2022 Tonga event. In the aftermath of the HTHH eruption, the early arrival of the relatively small leading ocean waves before the primary tsunami, as theoretically expected, revealed the atmosphere-ocean dynamic coupling in the Pacific Basin and also produced unusual transoceanic waves observed globally.

In this part of the study, the global propagation of the atmospheric pressure oscillations induced by the January 15, 2022 Hunga Tonga-Hunga Ha'apai volcanic eruption and the consequent ocean waves in the Pacific Ocean, the Caribbean and the Mediterranean were numerically solved. The research carried out in this part involves two major parts: the development of a synthetic pressure forcing model based on barometric measurements from different parts of the world and the application of the nonlinear shallow water theory using a hydrodynamic model to simulate the global propagation of the atmospheric pressure waves. Both cases were implemented for the first and second pressure waves, the second wave reaching a location from the antipodal point. Then, the hydrodynamic model, NAMI DANCE SUITE (Chapter 4.3.2), was forced with the pre-produced pressure fields to compute the corresponding sea levels at selected locations in the Pacific, Caribbean and the Mediterranean. The comparison of the modeling results with both the barometric

measurements and the sea level measurements at selected DART buoys and coastal tide gauges shows that the atmospheric pressure induced tsunami generated by the January 2022 HTHH eruption is fairly well reproduced by the presented approaches. A comprehensive analysis of the event from the atmospheric pressure wave propagation to the ocean waves in a global manner, including novel modeling approaches for the atmospheric pressure, considering the varying speed, amplitude and altitude of the pressure wave, is highlighted (Dogan et al. 2022).

5.1 Data and Methods

5.1.1 Pressure Data

The barometric measurements utilized for the amplitude and arrival time of the first and second pressure pulses where the second corresponds to the wave reaching from the antipodal point were collected from different regions of the world (Figure 5.1), Japan (42 stations), Turkey (15 stations), New Zealand (3 stations from Auckland, Cape Reinga and Lower Hutt), the US (Florida and Anchorage in Alaska), Australia (Coober Pedy), Indonesia (Yogyakarta), Malta (Marsaxlokk), Italy (Ispra) and Germany (Stuttgart). The temporal resolution of the measurements is 1 min in Japan, Turkey, Indonesia and Malta and 10 min in Italy. Other measurements were obtained by digitization and their original temporal resolution is unknown. However, since they were able to capture the general shape of the pressure pulse and therefore provide valuable data for different regions, it is appropriate and worth using them for comparison.

The pressure records in Japan were obtained from the Weathernews Inc. barometric pressure data measured by Soratena Weather Sensors (https://global.weathernews.com/news/16551/). The data from Turkey was obtained from the Turkish State Meteorological Service (https://mgm.gov.tr/); records from both regions were obtained by special request for research. The barometric data of Indonesia was obtained from Indonesian authorities via personal communication.

The pressure record of Malta was obtained from the University of Malta. The pressure time series were filtered by using a bandpass filter in Matlab with a cutoff period of 2.4 hours as the Lamb wave has a period of ~1 hour.

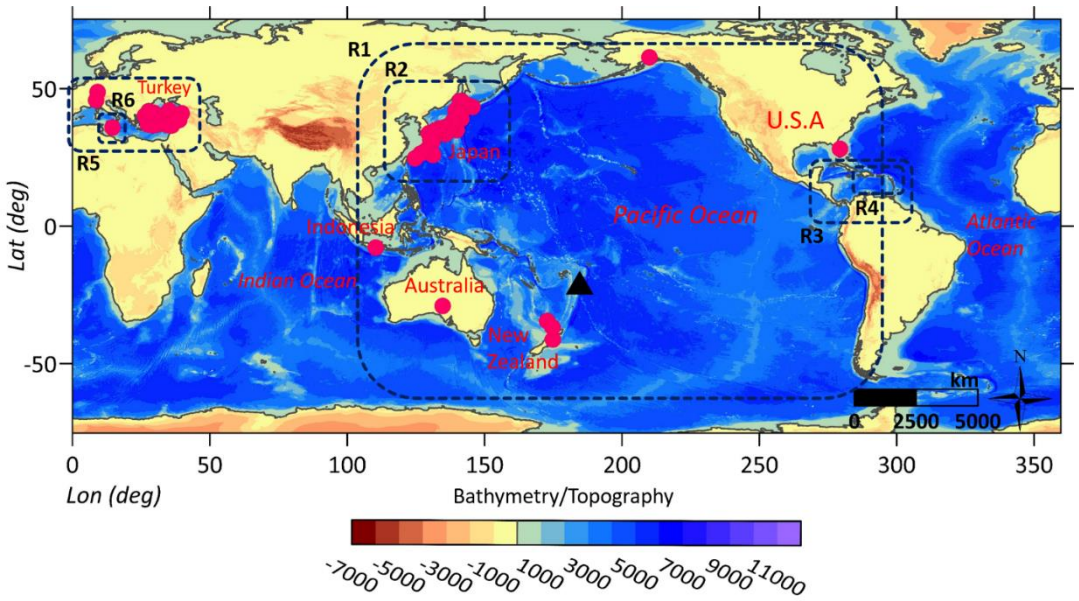

Figure 5.1 Bathymetry/topography of the global domain used in the numerical simulations. Pink dots show the locations of the barometric stations. The black triangle is the location of the HTHH volcano. Upon the global domain, the numerical simulations are focused on the specified regions, R1: Pacific Ocean, R2: Japan, R3: Caribbean Sea, R4: Caribbean Islands, R5: the Mediterranean Sea and R6: Malta.

5.1.2 Sea Level Data

The sea level time series used in this study are obtained from the following data sources: DART (Deep-ocean Assessment and Reporting of Tsunamis) buoy data in the Pacific Ocean from NOAA National Data Buoy Center (https://www.ndbc.noaa.gov/obs.shtml), New Zealand DART buoy data digitized from Gusman & Roger (2022) and tide gauge records in Japan, the Mediterranean and the Caribbean from the UNESCO IOC Sea Level Station Monitoring Facility (https://www.ioc-sealevelmonitoring.org/) and European Commission World Sea

Levels (https://webcritech.jrc.ec.europa.eu/SeaLevelsDb) databases. The DART buoy data from NOAA have different sampling rates as 15 min before the detection of an event and 1 min and 0.25 min after and was detided by using a highpass filter function in Matlab with a cutoff period of 4 hours. The tide gauge data has a constant sampling rate of 1 min, which was also detided by a bandpass filter. The selected gauge locations where the sea level measurements were processed and used for the comparison of modeling results are shown in Figure 5.2.

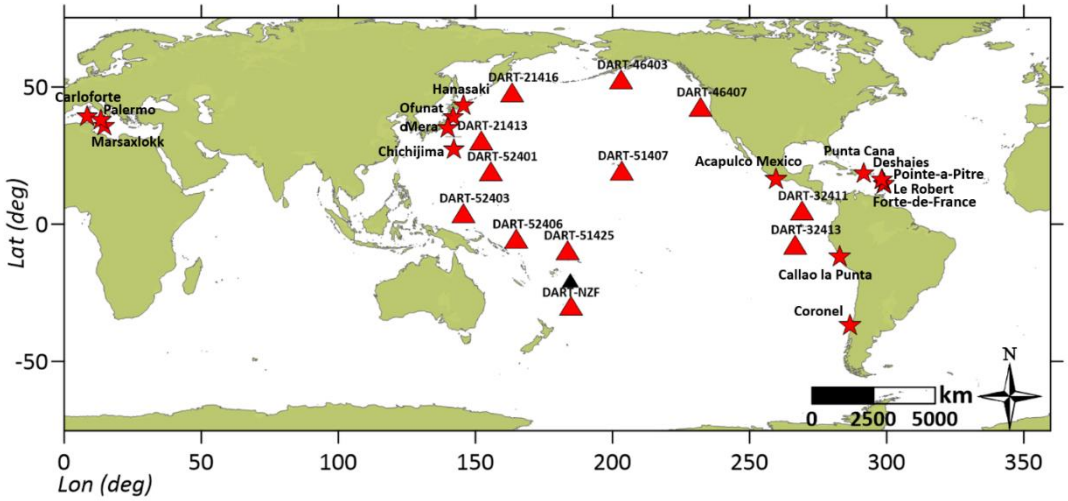

Figure 5.2 Numerical gauge points used for sea level comparison; DART Buoys in the Pacific Ocean (red triangles) and tide gauges (red stars) in Japan and other Pacific Coast, the Caribbean Sea and the Mediterranean Sea.

5.2 Atmospheric Pressure Wave Modeling

The atmospheric pressure wave propagation for the first cycle (first two pressure pulses) around the globe was solved by two different modeling approaches. The first approach is developing a synthetic pressure model by empirical relationships based on the traveling speed and the amplitude of the pressure wave obtained from barometric measurements. The second approach is applying a hydrodynamic model to simulate the pressure wave propagation with an initial disturbance, representing the Earth's surface as the "bathymetry" of the atmospheric layer where the pressure

wave traveled. Those approaches are explained in the following two subsections in detail.

5.2.1 Synthetic Pressure Model based on Measurements

The synthetic air pressure modeling was performed based on the available barometric measurements explained in Chapter 5.1.1. First, the arrival times of the first peaks of the pressure wave were extracted from the data with respect to 04:15 UTC as the event origin time. Based on the arrival times and the distances from the volcano, the average traveling speeds for the pressure wave were derived. When I classified the scattered speed data as the westward and eastward propagation of the pressure wave with respect to the volcano, I observed that the westward propagation was faster than the eastward propagation. In addition, the traveling speed behavior in the area closer to the volcano, approximately up to ~2.5 hr, and after that time was different. It seems that the speed is linearly increasing but with a lower acceleration after some point, reaching a more stabilized state. Two linear functions for the first ~2.5 hr (Equation 5.1), and after, were applied based on the gathered pressure speed data and data given in Ramirez-Herrera et al. (2022) for the Mexico and the Caribbean Sea regions. The linear functions after the 2.5 hr also differ for the eastward (Equation 5.2a) and westward (Equation 5.2b) propagation (Figure 5.3), representing the pressure waves circling over one side and the other side of the globe with respect to HTHH. A possible reason can be the Earth's rotation for such an observation. We suggest the following linear relations for the average traveling speed of the pressure wave after slight modification according to the preliminary sea level comparisons.

$$V(t) = 278.2 * t + 385 \qquad if\ 0.5 < t \leq 2.467\ hr \tag{5.1}$$

$$V(t) = 2.84 * t + 1065 \qquad if\ 2.467 < t < 36\ hr \tag{5.2a}$$

$$V(t) = 1.98 * t + 1063 \qquad if\ 2.467 < t < 36\ hr \tag{5.2b}$$

where t is time from the explosion in hours and $V(t)$ is the time-dependent average traveling speed of the pressure wave in km/hr. It is also important to note that our study does not focus on the early phase of the explosion and the resulting shockwave, which was thought to be effective in the immediate vicinity (~5 km) of the volcano (Lynett et al. 2022). In addition, suggested average traveling speed values for the pressure wave by different researchers have a quite wide range. Burt (2022) suggested an average traveling speed of ~315 m/s (~1134 km/hr) for the pressure wave reaching the British and Irish Isles. On the other hand, Nishiwaka et al. (2022) presented a speed of 200-220 m/s, which corresponds to 720-792 km/hr in the Pacific Ocean. Carvajal et al. (2022) also analyzed the arrival time of the leading ocean waves based on coastal tide gauge records from around the world. Their analysis based on time correspondence between the atmospheric pressure pulse and leading tsunami wave indicated a travel speed of 307 m/s ~1105 km/hr. However, my preliminary simulations of ocean waves using different constant traveling pressure speeds showed great discrepancies between the measured and computed values of the arrival time in different regions of the world.

The maximum peak and trough values from the pressure time series were extracted to derive a relation for the amplitude of the pressure wave as a function of distance from the volcano. A power function following the pressure wave amplitude-distance analysis of Scorer (1950) was fitted to the amplitude data up to the antipodal point, where the function was taken as symmetrical after halfway to the antipodal point (~10020 km) (Figure 5.4a and 5.4b). In Figure 5.4a, additional pressure peak amplitude data gathered from different studies are also plotted to show that my relation is compatible with other measurements. Equation 5.3 and Equation 5.4 are the suggested relations for the peak and trough amplitudes of the pressure wave, where d is the distance from the volcano in km, a_{peak} and a_{trough} are the peak and trough amplitudes of the pressure wave and c_{peak}, c_{trough}, c_1 and c_2 are empirical constants determined as 135.3, 441.7, -0.5 and -0.7, respectively.

$$a_{peak}(d) = c_{peak} * d^{c_1} \tag{5.3}$$

$$a_{trough}(d) = c_{trough} * d^{c_2} \tag{5.4}$$

where $d = d\ for\ 0 < d < {}^{\pi R}/_{2}$, $d = \pi R - d\ for\ {}^{\pi R}/_{2} < d < \pi R$ and R is the radius of the Earth.

Based on the traveling speed and amplitude relations given above, a sinusoidal signal (Equation 5.5 and Equation 5.6) with a bandwidth (B_w) of 600 km was produced for the pressure wave as in several other meteotsunami modeling studies (Williams et al. 2021; Vilibic, 2008) and as such pressure profile is commonly observed during meteotsunami events (Monserrat et al. 1991; Vilibic et al. 2004; Vilibic, 2008). The pressure signal to be inputted for the ocean wave simulations was produced every two minutes and the radial/spherical distances from the volcano were computed by applying the Haversine formula (Figure 5.5).

$$P(r,t) = a_{peak} \sin(kx) \quad if\ 0 < x < \frac{B_w}{2} \tag{5.5}$$

$$P(r,t) = -a_{trough} \sin(kx) \quad if\ \frac{B_w}{2} < x < b_w, \quad else\ P(r,t) = 0 \tag{5.6}$$

Where a_{peak} and a_{trough} are the pressure amplitudes calculated from Equation 5.3 and Equation 5.4, $k = {}^{2\pi}/_{B_w}$, $x = d_{point} - (r - \frac{B_w}{2})$, d_{point} is the radial distance of a point from the volcano in km, and r is the arc distance between the inflection point of the sinusoidal pressure band and the volcano. r was calculated from $r = V(t) * t$ where $V(t)$ was obtained from the empirical relationships given in Equation 5.1 and Equation 5.2, and t is the time spent from the explosion in hours.

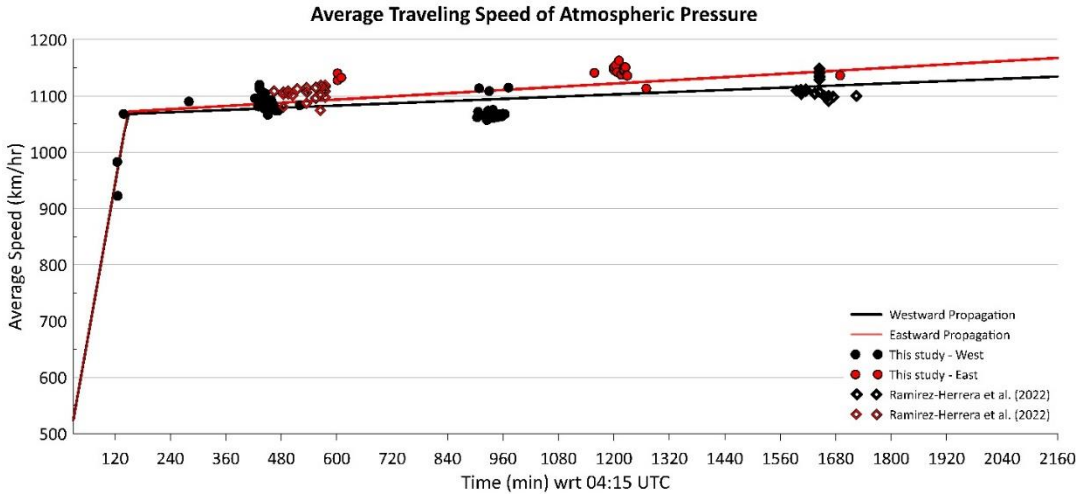

Figure 5.3 Linear fits (red and black lines) for the average traveling speed of atmospheric pressure wave as a function of time assumed in the synthetic model based on barometric measurements (red and black dots). Red and black colors represent the eastward and westward propagation with respect to HTHH.

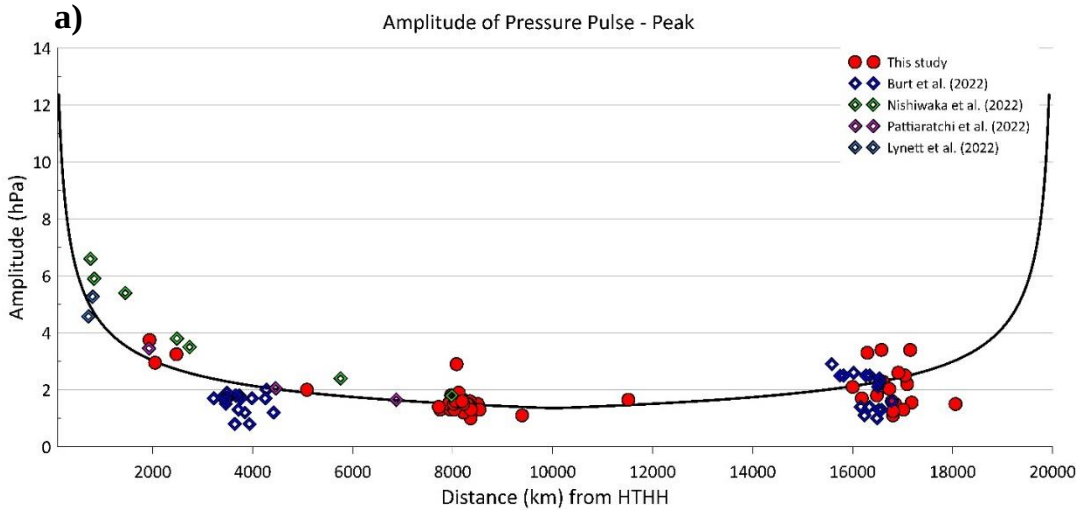

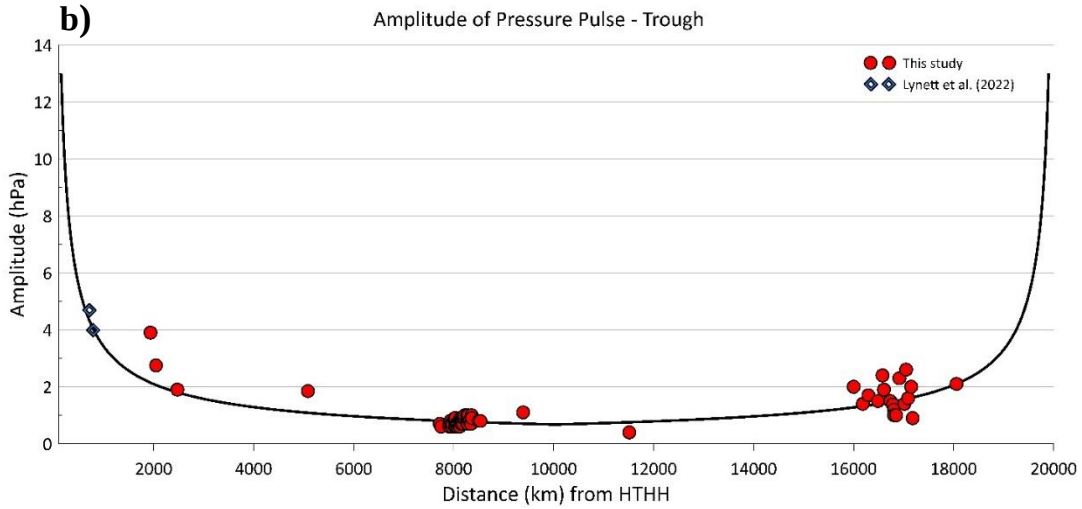

Figure 5.4 Curve fits (black lines) for the a) peak and b) trough amplitudes of the atmospheric pressure wave as a function of distance from HTHH assumed in the synthetic model based on barometric measurements (red dots). Other point data are extracted from different studies and are shown only for comparison.

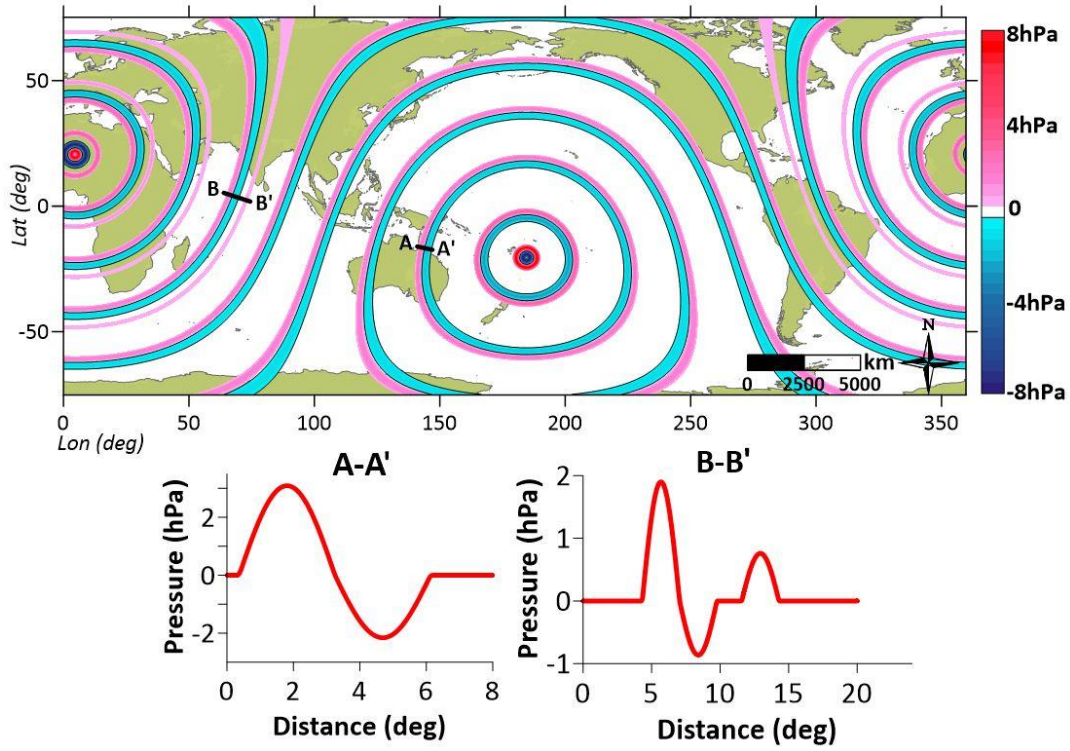

Figure 5.5 Map of computed pressure fields for every two hours based on the synthetic model.

5.2.2 Modeling of Pressure Waves by Hydrodynamic Simulations

In this part of the study, the propagation of the pressure wave for the first cycle around the globe was simulated by applying the nonlinear shallow-water theory using the numerical model, NAMI DANCE SUITE (Chapter 4.2.3). Nappo (2013) points out that air compressibility is generally insignificant in the lower atmosphere but becomes important in the upper and middle atmosphere due to the decreasing air density. They also find the linear theory robust and useful to be applied to the gravity waves in the middle and upper atmosphere. Therefore, in this approach, the atmospheric pressure waves were treated as shallow water waves and their global propagation was simulated by using a 2D hydrodynamic model on a global domain. The domain covering the surface of the Earth was set by assuming an initial elevation for the atmospheric pressure layer as 19.2 km on top of the sea surface and the topographic elevations were adjusted accordingly. In such a way, the atmospheric layer where the pressure wave had traveled was taken as the bathymetry, including the orography, i.e., the mountainous areas were the shallower areas of the domain (Figure 5.6). Then, the air temperature, which is another parameter affecting the speed of the waves, was taken into account by extracting the temperature equivalent depth values from the pre-set domain. The depth values were calculated by making use of the formula of the speed of the sound wave in air ($v_s = {\gamma R_a T}/{M_a}$) changing with atmospheric temperature. If it is assumed that the speed of the air pressure wave only changes with the temperature, as also suggested by Amores et al. (2022), the temperature equivalent depth values can be calculated by equating the phase speed of a shallow water wave ($C = \sqrt{g * h}$) to the speed of the pressure wave coming from $v_s = C = {\gamma R_a T}/{M_a}$ formula, where all the parameters in the equations are constant except the depth (h) and temperature (T). Therefore, the global distribution of atmospheric temperature at the atmospheric levels of 2 m and 100 hPa were obtained for every hour from ECMWF ERA5 reanalysis data and their average was taken by following the simplest approach as given by Amores et al. (2022). These

temperature values were converted to the temperature equivalent depth values by equating the two formulas given above ($\sqrt{g * h} = {\gamma R_a T}/{M_a}$), to be incorporated into the global domain. The bathymetric domain was updated every hour in the simulations to consider the temporal change of the temperature fields. Later, I simulated the propagation of the pressure waves like shallow-water waves by inputting an initial circular disturbance of 500 km in diameter with a maximum amplitude of 45 m following a Gaussian shape. The spatial sea level outputs of this simulation every 2 minutes were converted to pressure fields by applying the inverted barometer rule and were taken as inputs to solve the resulting ocean waves.

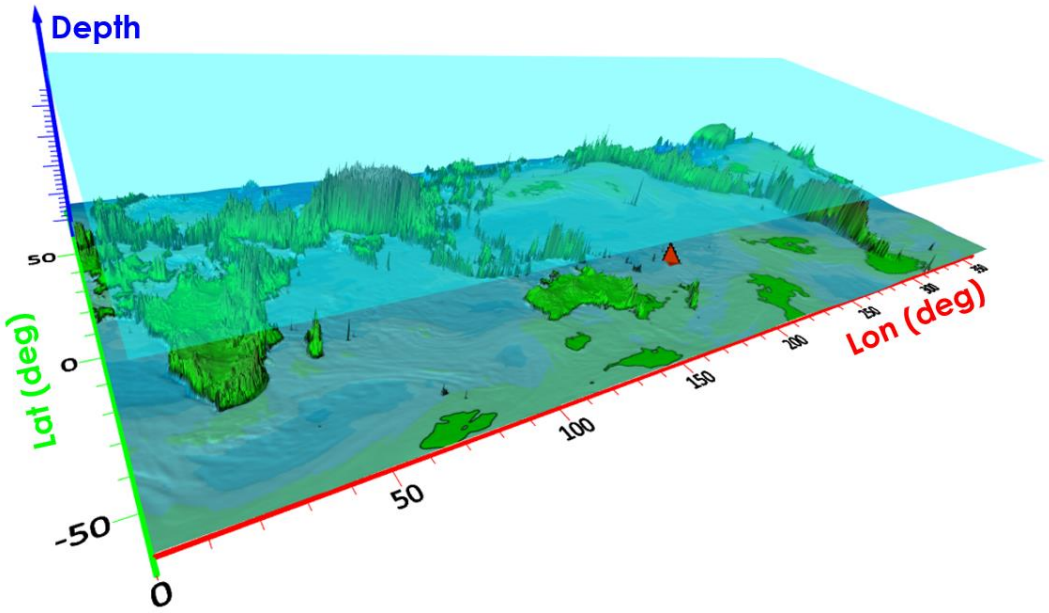

Figure 5.6 Schematic representation of the global domain developed for the simulation of global pressure propagation by hydrodynamic model. The depth values are based on orography and adjusted by temperature equivalent depth values at every hour. The red cone shows the location of the HTHH volcano.

5.3 Ocean Wave Modeling

The propagation, coastal amplification and inundation of the long ocean waves due to the input of water surface disturbances and/or spatial and temporal pressure and

wind fields can be represented by the nonlinear form of shallow water equations. The set of two-dimensional forms of those equations with atmospheric pressure and wind field terms in Cartesian coordinates are given in equations (4.23)-(4.27).

In this part of the study, the numerical model, NAMI DANCE SUITE, was forced with the produced atmospheric pressure fields to compute the consequent long ocean waves. In addition to standard inputs (bathymetry, initial water surface displacement, and fluxes if needed), the spatial distribution of the barometric pressure at the sea level in Pascal at specified intervals during the simulations was employed. The nonlinear forms of long-wave equations were solved using a staggering leapfrog scheme numerical solution procedure in nested domains with rectangular structured mesh by the code.

A global domain was set up with a grid size of 6950 m using GEBCO 2021 bathymetry data for the numerical simulations, as shown in Figure 5.1. The simulations of the pressure wave were carried out in this domain. For the simulations of the ocean waves, three different nested domains (R1&R2, R3&R4 and R4&R5 in Figure 5.1) were created upon this global domain to achieve finer grid sizes desired to capture the waveforms in the selected gauges. The grid sizes in the nested domains R1 and R2 were 3500 m and 300 m, respectively. 600 m and 240 m grid sizes were used for the R3 and R4 domains focusing on the Caribbean Sea. The grid sizes in the Mediterranean were 900 m and 25 m for R5 and R6, respectively. The simulations were performed for a 36-hour duration.

5.4 Results and Discussion

The comparison of the computed pressure profiles based on the synthetic model with the barometric records is given in Figure 5.7, which shows a nearly perfect agreement in Japan (Figure 5.7a) and other available locations (Figure 5.7c) and good agreement in Turkey (Figure 5.7b). Figure 5.13a and Figure 5.13c also show the Q-Q plots prepared for the arrival time and amplitude values of the measured and

computed peaks of the first pressure wave based on the synthetic model. While the agreement between the modeling results and the observations is excellent in terms of the arrival time, the same does not apply to the peak amplitudes. However, this is an inevitable consequence of producing synthetic pressure profiles based on empirical relations and it is hard to capture all the observed amplitudes as they show scatter even in a smaller region, i.e., Turkey, considering the whole globe. Despite this, the computed sea levels based on this approach in the R1&R2 regions (Pacific DART buoys and tide gauges and Japan tide gauges) well captured the observed waveforms until the regular tsunami arrived indicated by the blue dashed line in Figure 5.9. The modeled sea levels still show a nice trend even later as the fluctuations resulting from the pressure (free waves) continued to propagate in the region, and the waves were amplified at some locations by both factors. The modeling results in the Caribbean Sea and the Mediterranean Sea tide gauges (Figure 5.7) also show very good agreement with the measurements in terms of both the arrival time and the wave amplitudes. Therefore, the analysis indicates that the discrepancy in the pressure peak amplitudes is well tolerated in the computed ocean wave amplitudes.

The pressure profiles produced from the hydrodynamic simulations show nearly perfect agreement at all locations (Figure 5.8). The arrival times of the first pressure peaks are again well captured, and so are the ocean waves (Figure 5.13a and Figure 5.13b). The computed pressure peak amplitudes are larger in Japan region and lower in some locations at farther distances like Ispra-Italy and Stuttgart-Germany than the recorded values. One of the affecting factors is the assumed size of the initial disturbance in the simulations. Since the mechanism becomes more complex as the pressure wave travels farther distances, there may be other factors at specific locations that need to be considered in the model. Still, the model could achieve reasonable pressure amplitudes globally and the resulting sea levels show good agreement with the records in the Pacific, Caribbean and Mediterranean regions (Figure 5.10). The Q-Q plots for the arrival time (Figure 5.13b) and the amplitudes (Figure 5.13d) of the ocean wave show that the performance of the model is fairly

good. The only exception is Malta, where the arrival time of the ocean wave could not be captured in both approaches. In Malta, the first peak of the ocean wave arrived approximately 1.2 hrs later than the arrival of the first peak of the pressure wave. This is due to the free wave generation at a farther point and arriving at the station after going through the resonance mechanisms by traveling at their own speed. Although the model properly computed the forced and free waves in the Mediterranean basin with the given forcing, there should be some other local factors in the case of Malta, which are missing in the model and needs further investigation.

In addition, a careful analysis of the simulation results based on different bandwidths (wavelength) of the pressure showed that not only the wave period but also the computed sea levels at some specific locations were affected by the bandwidth parameter. Figure 5.11 shows the comparison of computed sea levels based on the synthetic pressure model with 600 km, 450 km and 300 km bandwidths at selected gauges, NZF DART buoy and two tide gauges in Japan, indicating larger amplification at smaller wavelengths. Those gauge points have a common feature; they are located near deep trenches, which is not surprising due to the relation between the length of the slope and the width (wavelength) of the pressure disturbance through the resonance mechanism. Therefore, the wavelength of the disturbance should also be adequately estimated for the accurate prediction of sea levels for such air-sea coupled tsunami generation systems.

As a further point, a world map with the corresponding Froude numbers (Fr) which were calculated for a constant speed propagation of pressure with 300 m/s ≈ 1080 km/hr sourcing from the Hunga Tonga-Hunga Ha'apai volcano explosion, is prepared and presented in Figure 5.14. In Figure 5.14, areas with Fr ≈ 0.9-1.1 can be considered where Proudman-like conditions are likely to occur, which explains the observation of higher wave amplitudes at some locations like the southeast coast of the Pacific, Japan and the Caribbean.

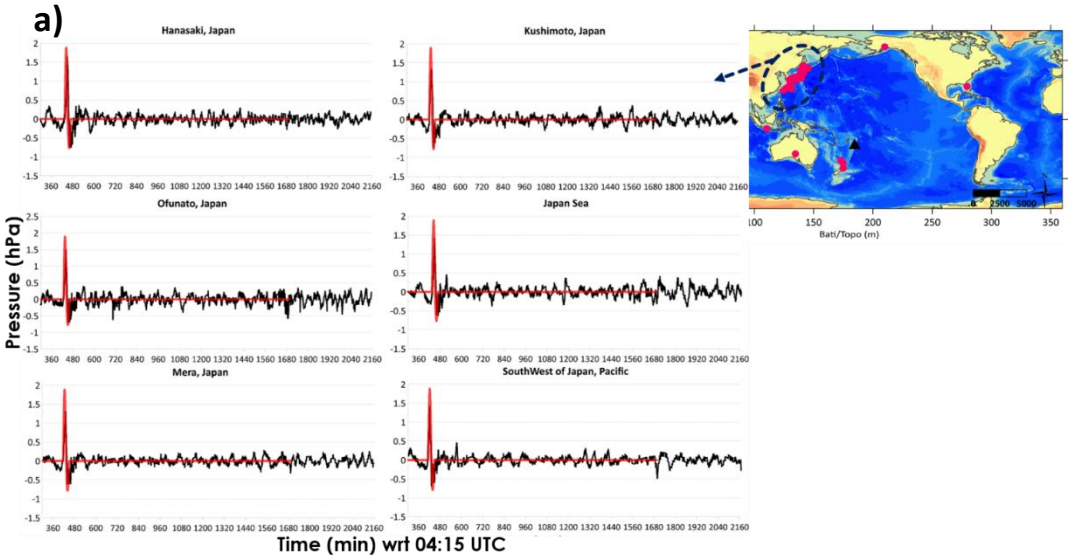
a)
Hanasaki, Japan
Kushimoto, Japan
Ofunato, Japan
Japan Sea
Mera, Japan
SouthWest of Japan, Pacific
Pressure (hPa)
Time (min) wrt 04:15 UTC
Bati/Topo (m)

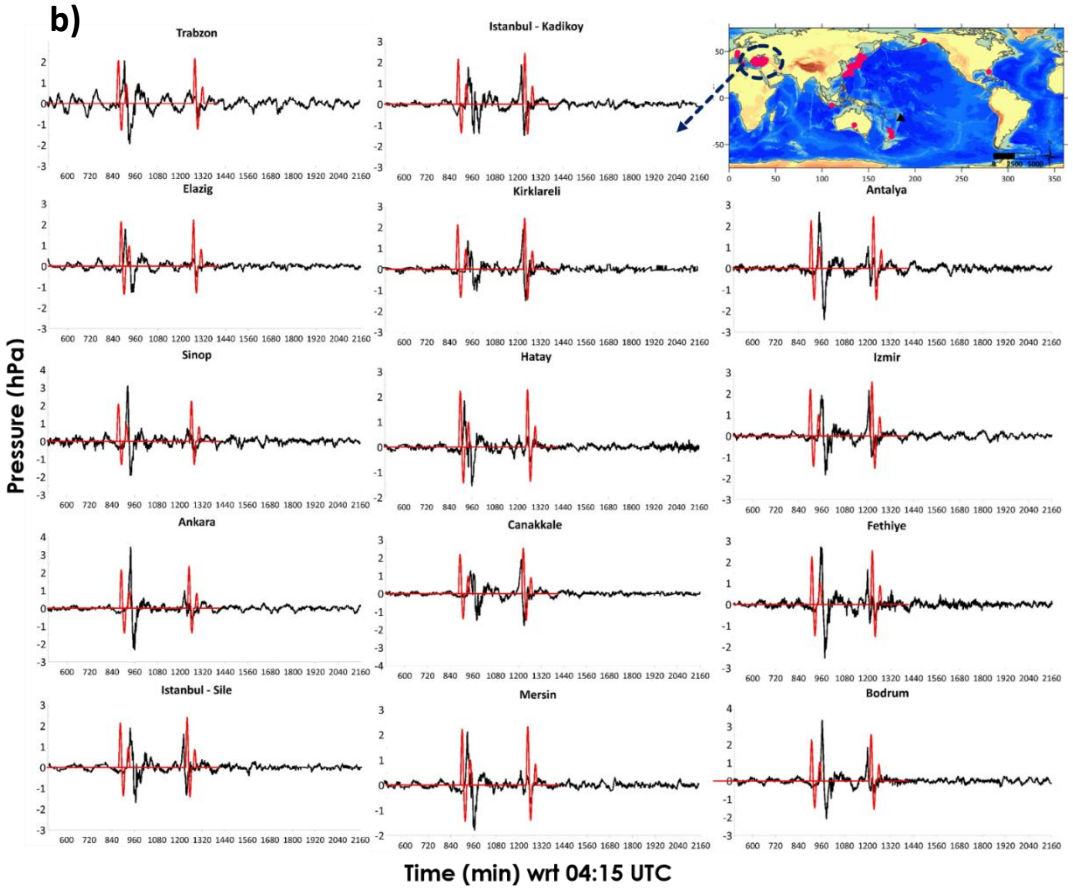
b)
Trabzon
Istanbul - Kadikoy
Elazig
Kirklareli
Antalya
Sinop
Hatay
Izmir
Ankara
Canakkale
Fethiye
Istanbul - Sile
Mersin
Bodrum
Pressure (hPa)
Time (min) wrt 04:15 UTC

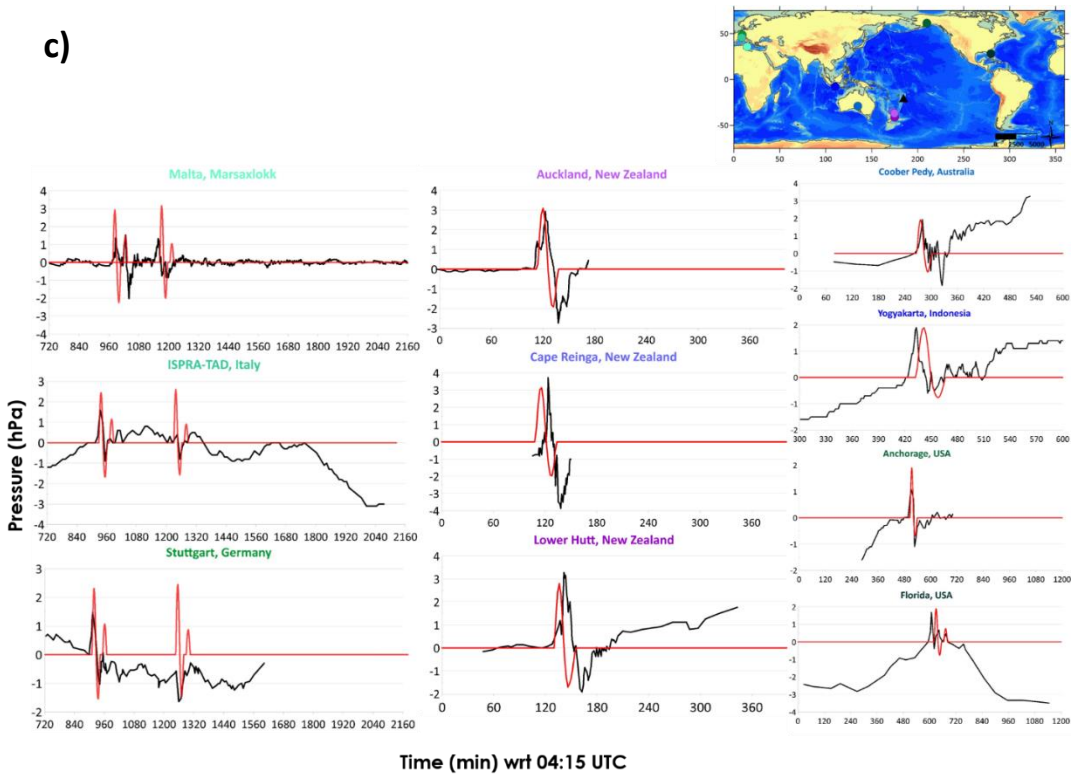

Figure 5.7 Comparison of pressure waves from the synthetic model (red) with the measurements (black) at selected gauges a) in Japan, b) in Turkey, and c) in other locations.

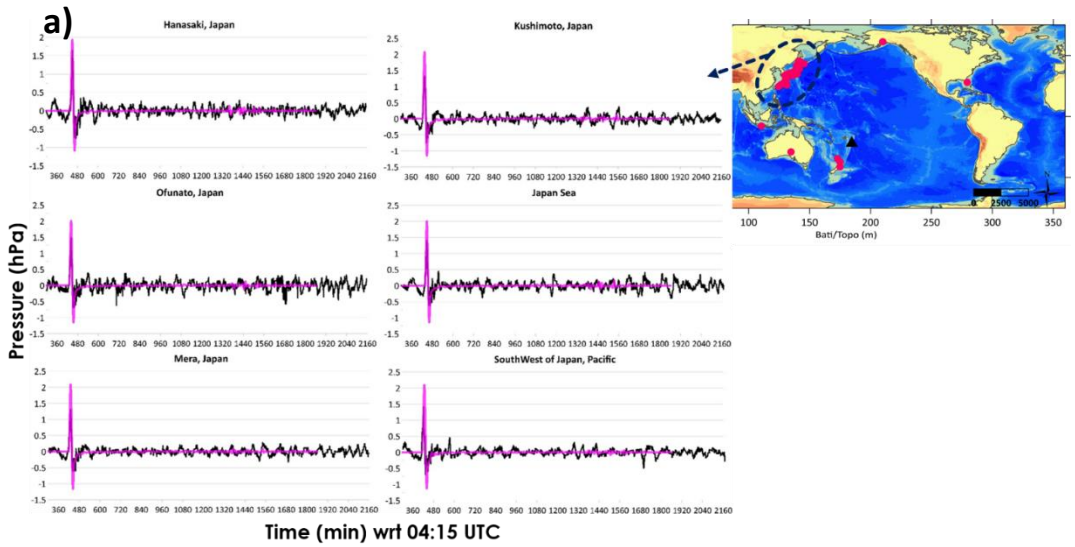

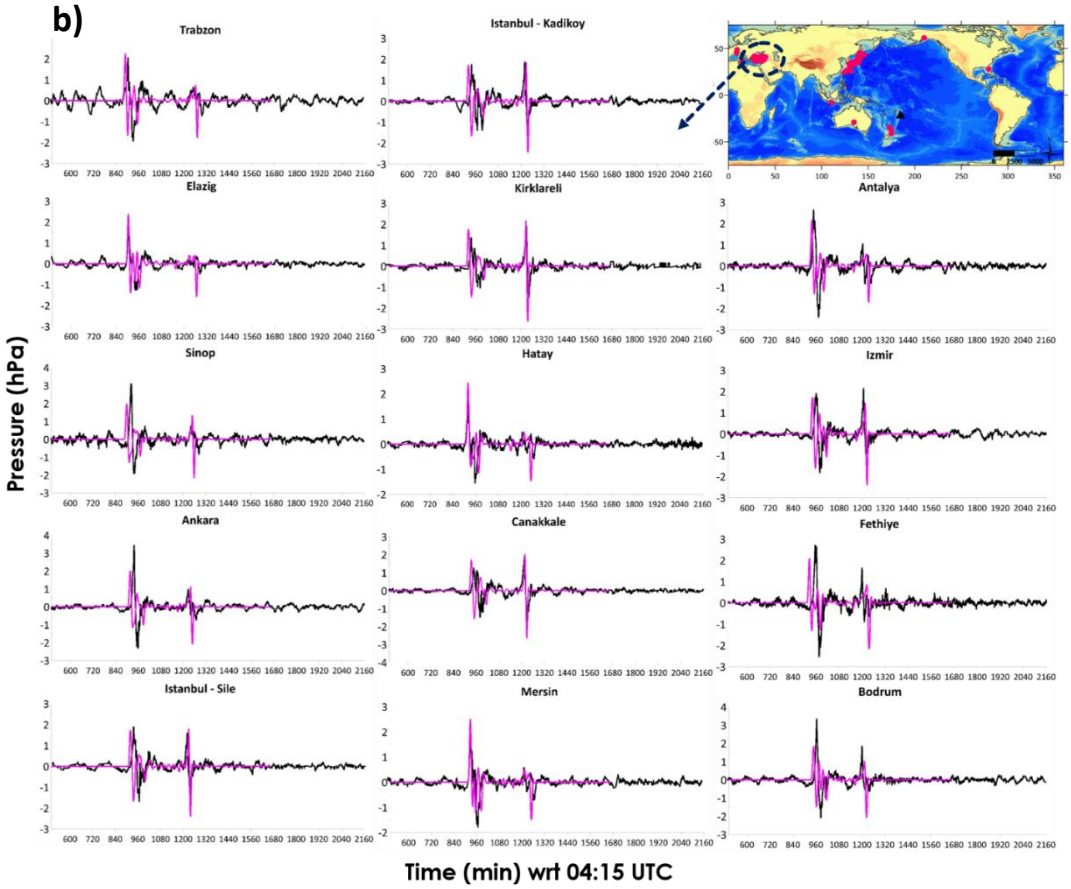
b)
Trabzon
Istanbul - Kadikoy
Elazig
Kirklareli
Antalya
Sinop
Hatay
Izmir
Ankara
Canakkale
Fethiye
Istanbul - Sile
Mersin
Bodrum
Pressure (hPa)
Time (min) wrt 04:15 UTC

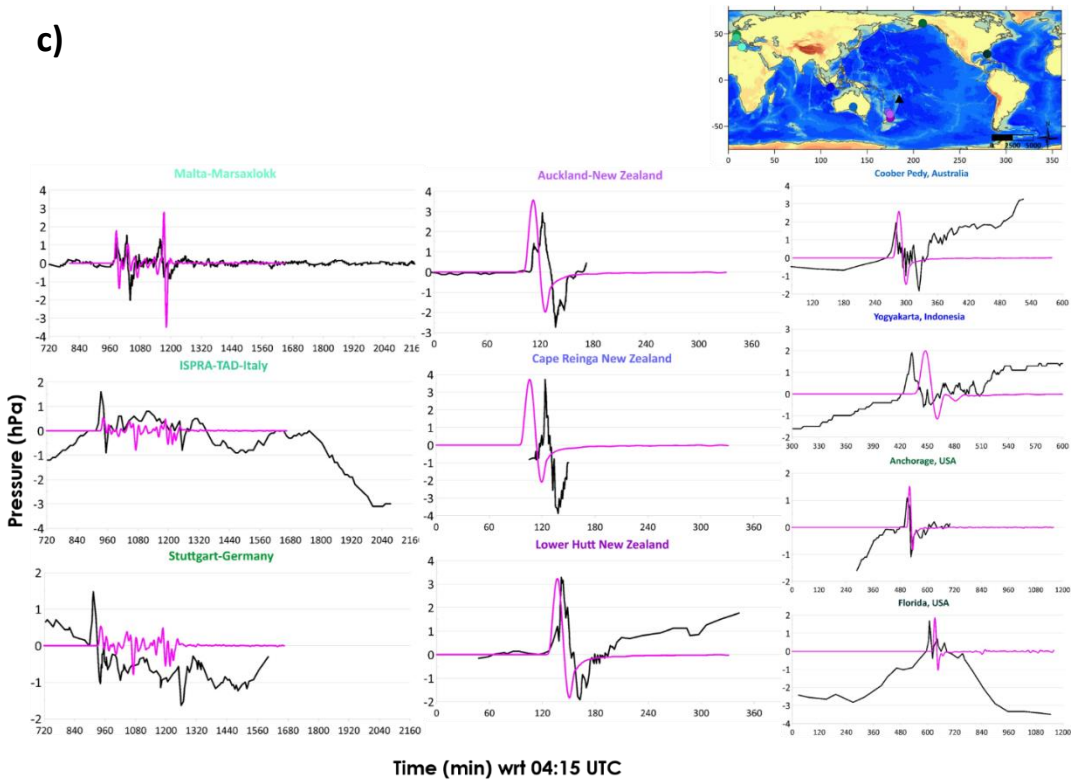

Figure 5.8 Comparison of computed pressure waves from hydrodynamic simulations (magenta) with the measurements (black) at selected gauges a) in Japan (R2), b) in Turkey, and c) in other locations.

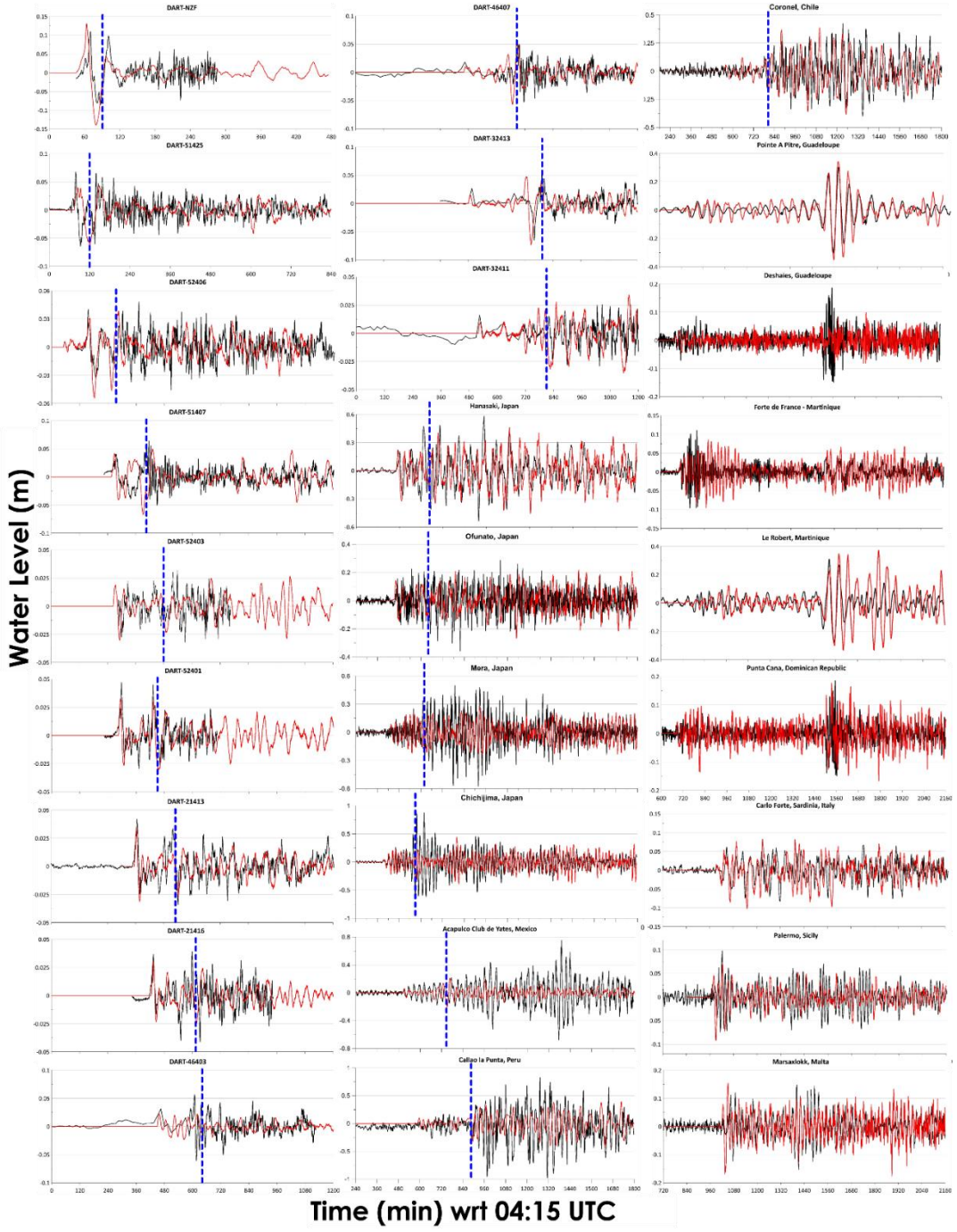

Figure 5.9 Comparison of sea level measurements at the selected gauges with the computed sea levels from the simulations forced by the synthetic pressure model

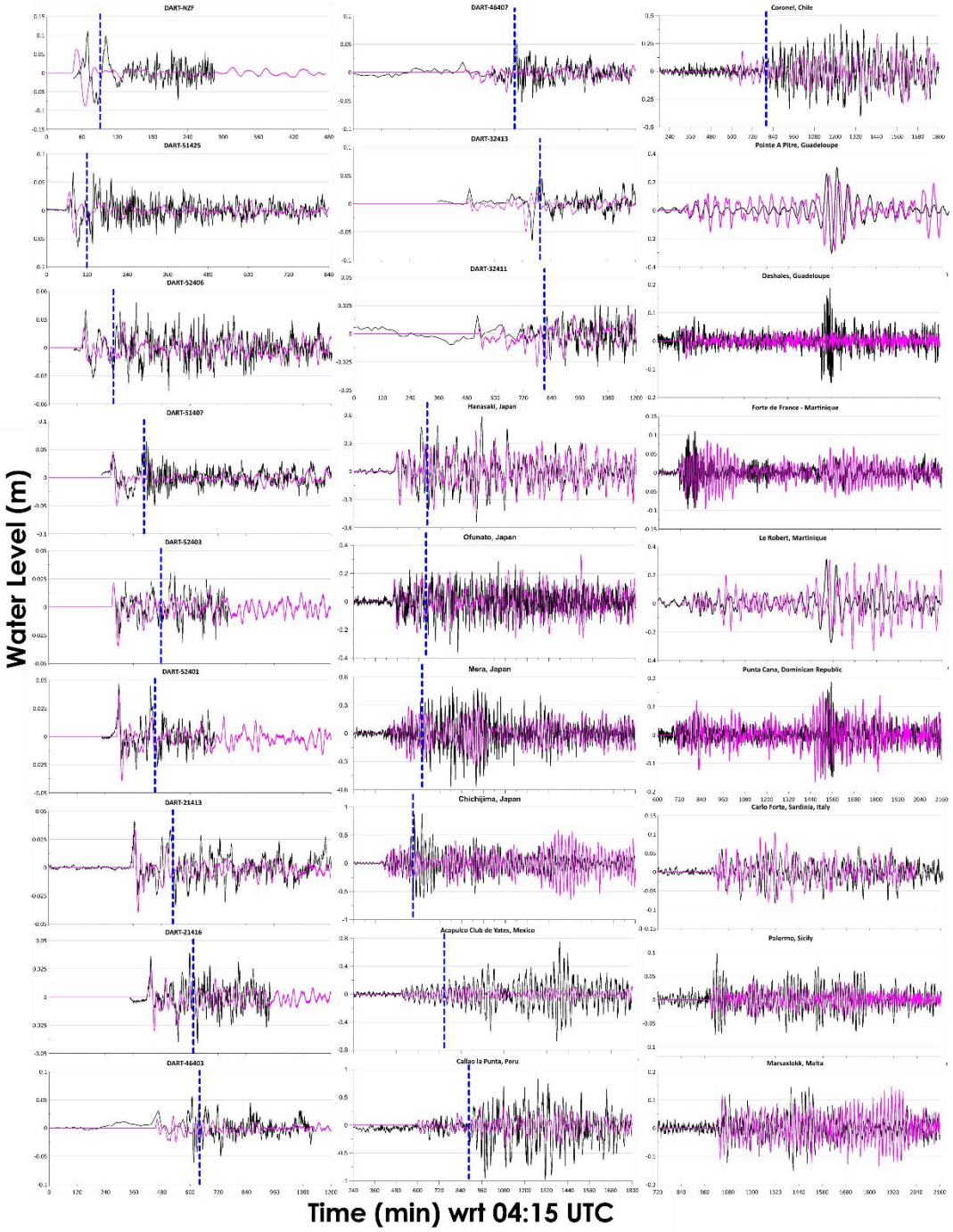

Figure 5.10 Comparison of sea level measurements at the selected gauges with the computed sea levels from the simulations forced by pressure waves from hydrodynamic simulations

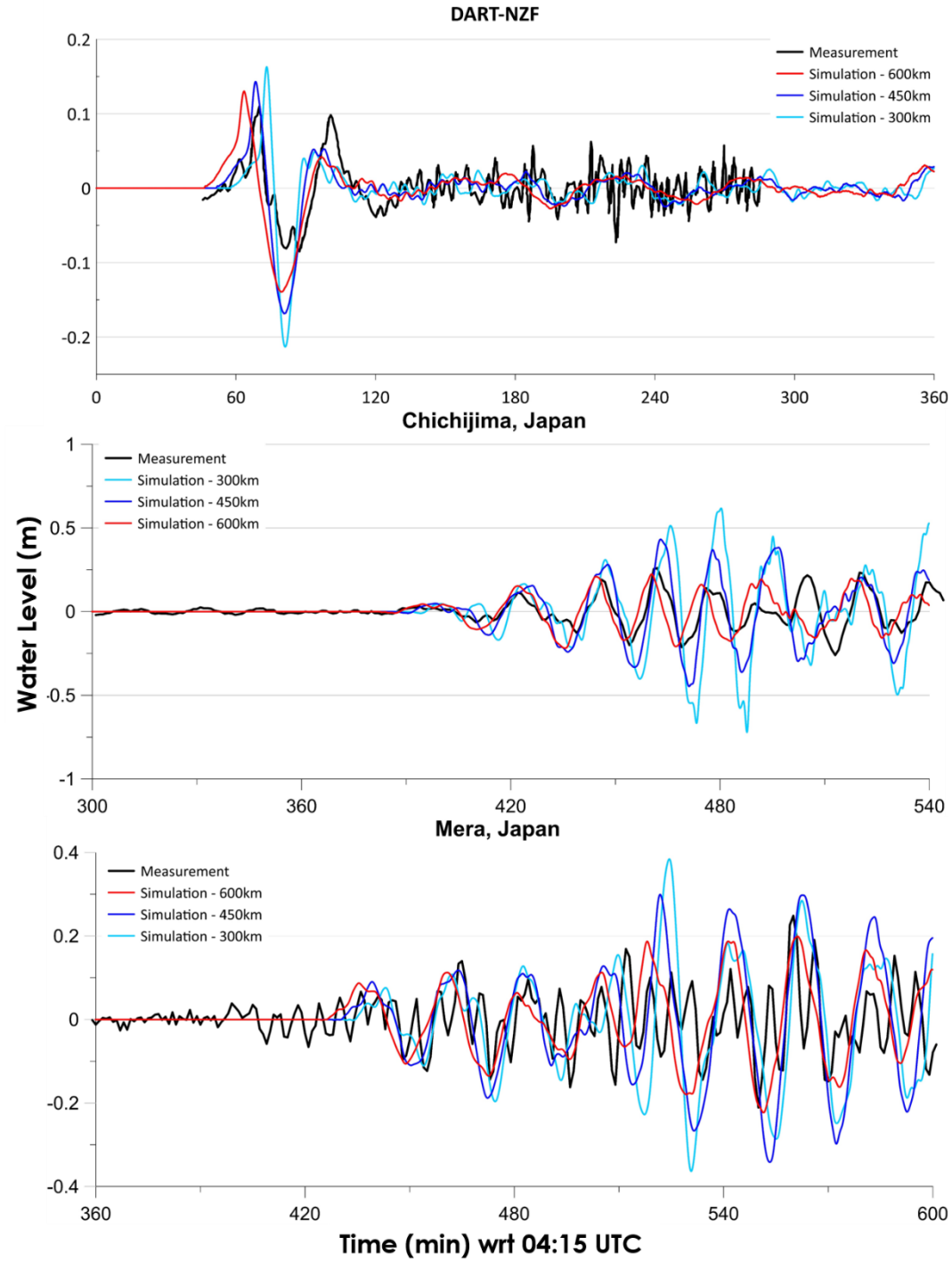

Figure 5.11 Comparison of computed sea levels from the synthetic pressure model with 600 km, 450 km and 300 km bandwidths (given in red, blue and turquoise colors, respectively) at selected gauges located near deep trenches, NZF DART buoy and two tide gauges in Japan

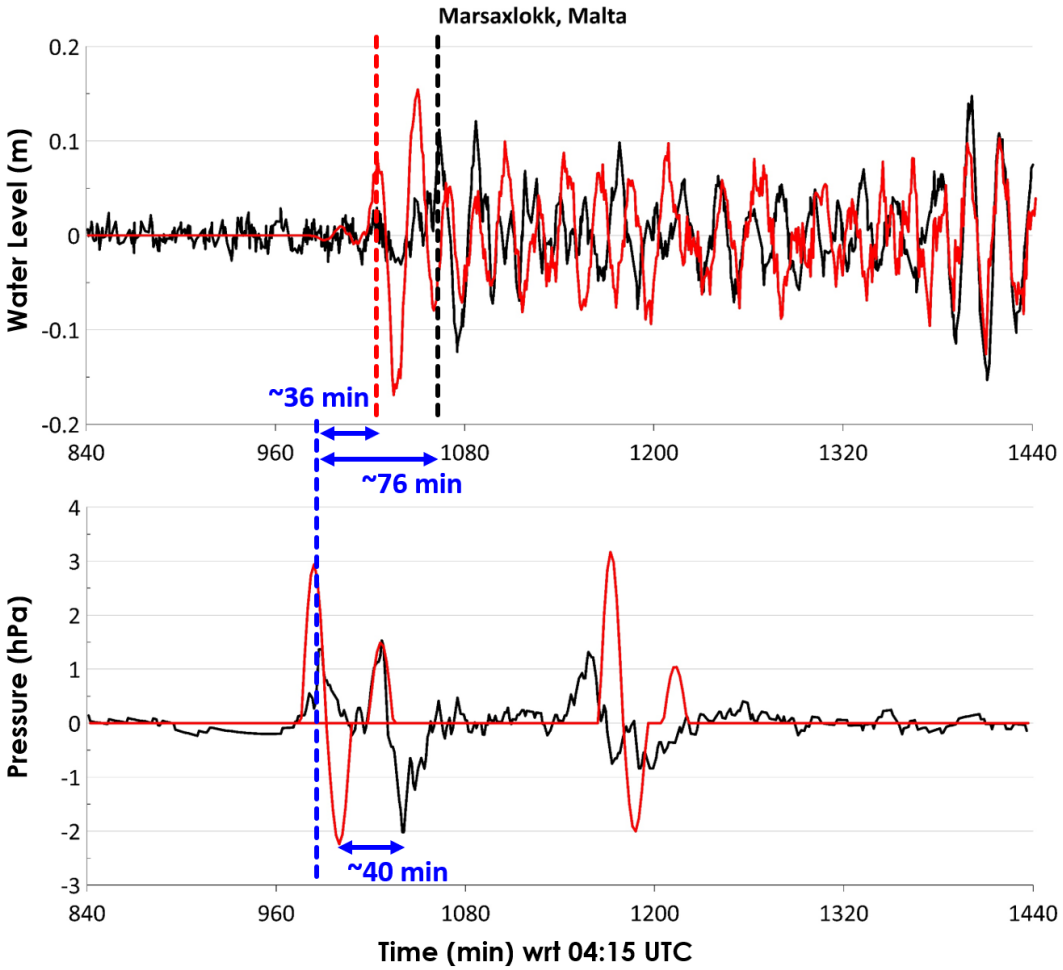

Figure 5.12 Time series analysis of sea level and barometric measurements in Malta. The red, black and blue dashed lines indicate the computed sea level, measured sea level and measured pressure peak arrivals, respectively.

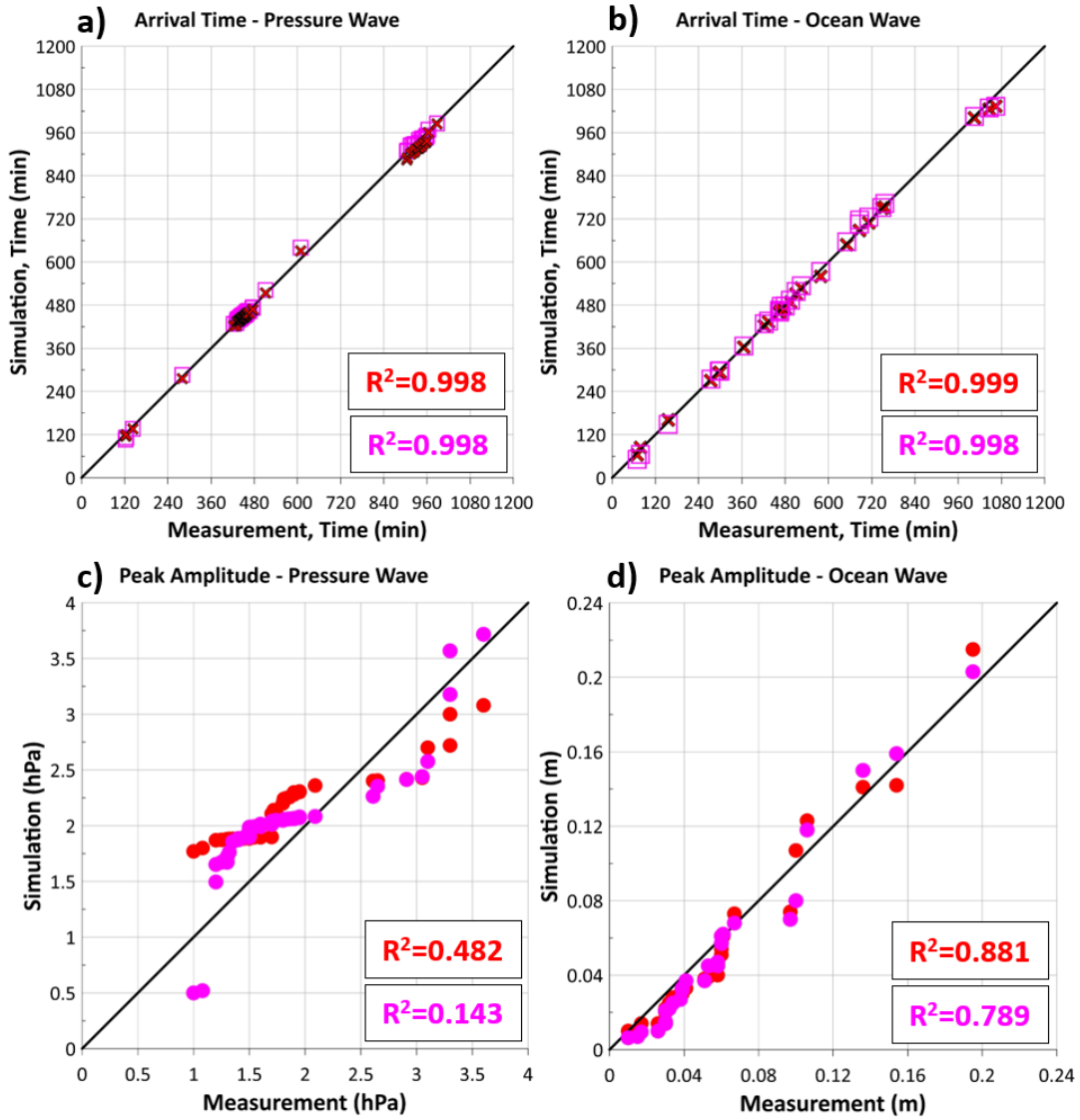

Figure 5.13 Plots of measured values versus modeling results for the arrival time (a and b) and the amplitude (c and d) of the first peaks of pressure wave and ocean wave, respectively. The red color represents the modeling results based on the synthetic model approach and the magenta is from producing pressure waves by hydrodynamic simulations (Chapter 5.2.1 and Chapter 5.2.2).

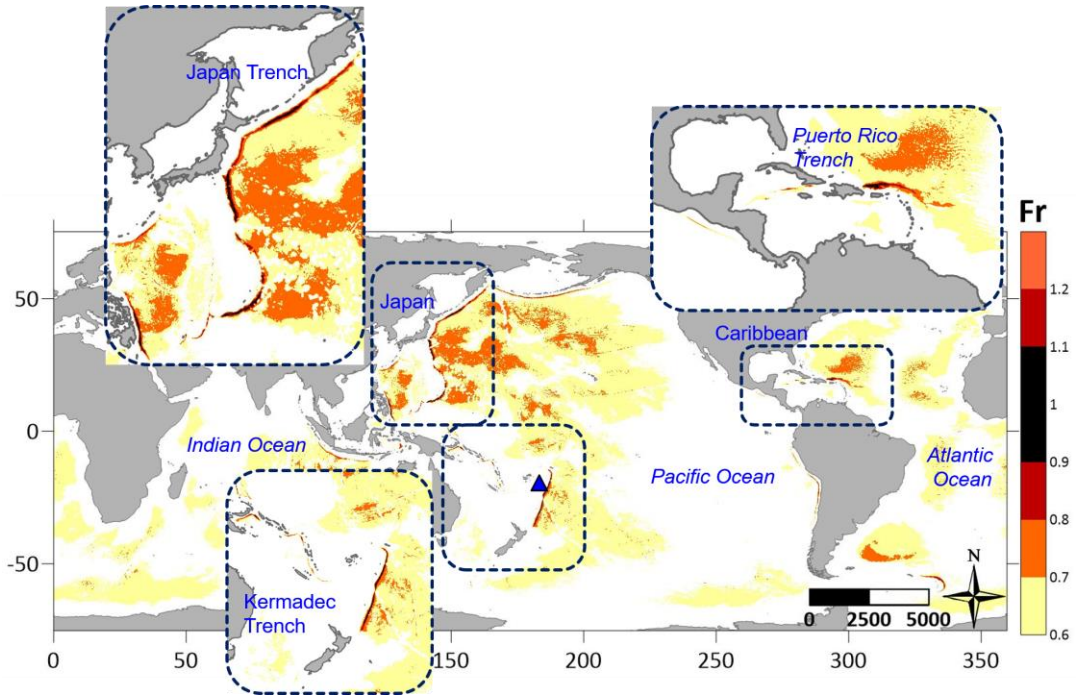

Figure 5.14 Map showing the areas with the corresponding Froude numbers (Fr) calculated for a constant speed propagation of pressure with 300 m/s ≈ 1080 km/hr sourcing from the Hunga Tonga-Hunga Ha'apai volcano explosion. Areas with Fr ≈ 0.9-1.1 can be considered where Proudman-like conditions are likely to occur. The bathymetry data source for the map where the ocean depth values are extracted is GEBCO (2021).

CHAPTER 6

SUMMARY AND CONCLUSIONS

This study is a humble attempt to provide insights on long wave generation, propagation and amplification originating from atypical sources, atmospheric disturbances and volcanic origin by i) employing tsunami numerical modeling, ii) developing new modeling approaches, iii) model verification and numerical tests on different bathymetries and resulting empirical curves to describe the relations between the wave amplifications and geometry of the bathymetries and iv) modeling applications on real scale recent events with the efficient utilization of freshly available measurement data. It should be emphasized that there is still much to be discovered from the recorded tsunami events increasing in number and involving different interesting/unique mechanisms, with a large amount of instrumental data available. Although significant developments have been achieved in tsunami research and practice (numerical modeling, hazard assessment, early warning systems and mitigation), it was clear after both the December 2018 Gunung Anak Krakatau and January 2022 Hunga Tonga-Hunga Ha'apai volcanic eruptions that the unusual tsunami events from atypical sources can be highly impactive and the community still needs huge progress on that direction, despite what has been achieved so far. Hence, it is humbly believed that this study contributes to the related research, gaining a place in the broad area from source processes to coastal hazard and warning, given the complexities and difficulties.

In the initial step, the study focuses on the demonstration of possible source alternatives for the December 22, 2018 Sunda Strait tsunami associated with the eruption of Gunung Anak Krakatau and attempts to better interpret the source mechanism by employing tsunami numerical modeling based on different scenarios involving submarine and subaerial mass movements and a combination of them. The field survey observations, as well as the tide gauge measurements, were used to

compare the modeling results and to achieve conclusions on the extent of tsunami hazard in the Sunda Strait region. Among the limited number of related studies, which was only a few up to this event, the presented work contributes to explaining the mechanism based on alternative hypothesis, considering the submarine changes in close proximity differently from others. It was also shown that the employed modeling strategy (coupling of a 2D landslide and a hydrodynamic model) worked fairly well, standing at a point between sophisticated landslide models and simple hydrodynamic models (summarized in Chapter 2.1.2), which is promising from the practical point of view, considering the large affected areas and consequent computational cost. Furthermore, the study provides insights into the volcanic tsunami hazard in the region, which has ramifications for different social and operational elements.

According to the interpretations, the volume and geometry of the mass movement (either subaerial or submarine) is a critical factor that can be configured based on scars and deposits or bathymetrical measurements needs to be carefully considered whether it occurred as a single event (like a block type rapid failure) or a series of sub-events. In this case, two different elliptical shape landslide related sources (Alternative 1 and Alternative 2) were tested assuming rapid failure and concluded that both alternatives were separate events not triggered by the December 22, 2018 GAK eruption and do not have any possible significant contribution to the observed tsunami. Alternative 1 most probably occurred in the form of a series of landslides, as our simulation results exhibit. In such a case, there may be some gradual failure or a series of discrete events that should be modeled in detail and accurately to exhibit the time intervals between failure of successive subunits and estimation of their volumes. However, this alternative can cause a significant tsunami in the Sunda Strait if it takes place as a single event and can be studied for potential tsunami generation by combined sources. On the other hand, it remains questionable if the slope failures considered in Alternative 2 occurred as a single event, even though this alternative does not seem to have a significant tsunami potential on the coast of Java and Sumatra Islands.

The flank collapse scenario is suggested as the best alternative for the source mechanism of the Sunda Strait tsunami, which can explain the observed coastal amplitudes. However, it is not a hundred percent certain that this scenario is the only responsible for producing the associated tsunami and its impacts in the study area due to the limitations of available bathymetric and topographic datasets. Note in this respect that the reflection of the effect of coastal topography, and the role of coastal protection, including coastal forests in modeling, are other important uncertainties in the numerical modeling of tsunami hazard. According to the simulation results of this scenario, the most impacted areas are Tanjung Lesung, Cigorondong (BBIP), and further southern region up to Paraja Bay in Pandeglang District, which are compatible with field survey observations. The modeling results also show the highest inundation in the Labuhan region according to this scenario, as pointed out in field survey studies by Syamsidik et al. (2019) and Muhari et al. (2019). Furthermore, the suggested source alternative is capable of producing the observed flow depths at the cliff-type beaches, whereas the simulated results and observations differ in flat type coastal areas. Still, the suggested scenario-based model could capture the observed waveforms satisfactorily. Lastly, shorter wave arrival times are computed at the places where higher amplitudes are experienced, implying a higher tsunami hazard potential in those locations.

In the next step, the research direction is oriented to a relatively young but important subject, long ocean waves of meteorological origin. The numerical model NAMI DANCE based on NLSW equations is upgraded to solve the long wave generation and propagation due to the spatial and temporal change of the atmospheric pressure and wind fields. The model is verified by comparing the numerical test results in a flat bottom basin against those from a newly developed analytical solution for meteotsunami generation in the water channel of the ‘power’ cross-section. Different speeds of pressure disturbance propagating over the 200 m deep flat bottom basin corresponding to different flow conditions (sub-critical, critical and super-critical) are used as the forcing mechanism. Satisfactory agreements between the numerical and analytical results are obtained. The model is further applied to basins with a

triangular lateral cross-section to investigate the generation and coastal amplification of the ocean waves toward shore in the propagation direction. Shown for the basin of triangular cross-section, the maximum wave amplification is observed at the water depth, where the speed of the pressure disturbance coincides with the wave celerity, satisfying the Proudman resonance condition. The examination of the wave amplification is extended with basins with shelf bathymetries which are much closer to the real conditions where meteotsunami waves are generated and propagated. Numerous numerical tests were conducted on stepwise shelf bathymetries with shelf slopes of 1:10-1:700 covering a wide range of steep and mild shelf slopes from 200 m to 20 m water depths. For each basin, thirteen different moving speeds of the pressure disturbance are tested. The upgraded hydrodynamic model was used to reveal the detailed behavior of long ocean waves due to atmospheric disturbances in different types of basins.

One of the primary factors affecting the sea level response is the average moving speed of pressure disturbance and the speed of the generated wave in the basin. When the speed of pressure disturbance coincides with the celerity of the generated wave, the continuous energy input to the generated wave results in higher wave amplitudes, increasing with time or the distance traveled as the analytical solution predicts. However, as shown in the numerical tests of the flat bottom basin, the wave evolves with the moving pressure disturbance and reaches a steady state at a certain point (of time/distance and amplitude) which depends on the pressure speed. Higher pressure speeds carry and induce more energy and result in higher resonance amplitudes which also require more time or distance of pressure propagation to achieve the maximum amplitude and stabilize. However, those mechanisms do not apply when the speed of pressure disturbance is slower or faster than the speed of the water wave, as the wave can not continue to evolve. This is simply because of the separation of the forcing and the generated wave after the generation.

Another important factor that leads to the amplification of meteotsunami generated by the propagating pressure disturbance is the bathymetric conditions of the basins. As the shelf slope is one of them, it is shown that the milder slopes can cause larger

wave amplification. On the other hand, the computed maximum wave amplitudes are smaller than the corresponding flat bottom basin cases where the Proudman resonance condition is achieved. Furthermore, the maximum amplification among the tests is achieved at a larger Fr, showing that the condition of $Fr = 1$ may not be a simple prediction method for the maximum amplification in basins with shelf bathymetries. Furthermore, the results have shown that the two parameters, the water depths before and after the sloping section, are as important as the shelf slope, providing favorable resonance conditions for specific pressure speeds. In addition, the effect of the wave reflection from the sloping section is quantified by calculating Root Mean Square Errors with respect to the base case, a flat bottom basin with 200 m depth. More reflection is observed at higher pressure speeds and steeper slopes, as expected.

The numerical tests performed within this part have certain conditions on the amount of pressure gradient, bandwidth of the pressure drop, water depths before and after the sloping section and the total basin length, including the lengths of pre-slope and post-slope sections. Therefore, it is essential to note that this part of the study provides discussions on several features based on the simulation results, but a more holistic analysis, comprising the quantification of wave amplification considering all the listed parameters, is needed. The problem will eventually become more complex and harder to solve as it resembles reality. At this point, an extensive database including the results of a sufficient number of simulations and interpolation methods between the results can be noted as a further research item. It is also evident that a more comprehensive study would include the combination of atmospheric pressure and wind forcing, which is another drawback of this study and can also be considered for further research.

As the last step, the explanation of the global tsunami generated by the January 15, 2022 Hunga Tonga-Hunga Ha'apai (HTHH) eruption, which had a worldwide signature, based on the methods and tools developed in the previous parts of the thesis study, is presented. This event has been a unique opportunity for modeling studies with a large amount of instrumental data and is of great importance, having

an unusual source mechanism, which has been a neglected source of tsunamis from volcanic eruptions, with resulting ocean waves observed on a global scale for the first time. The transoceanic waves excited by the dynamic coupling of the air and sea are numerically solved and the resonance mechanism that occurred in some areas is explained. I believe that succeeding in modeling both the air pressure waves and the ensuing sea waves satisfactorily by novel approaches has been one of the major outcomes of this study. Such demonstration can have wide implications for the hazard in similar settings.

Both the sea level measurements and the simulation results of the 2022 HTHH event (see Supplementary Files) show that the relatively small forced waves were followed by the free waves, which were propagating at their own speed before the regular tsunami sourcing from a volcanic mechanism arrived. It is also clear that the volcanic origin atmospheric pressure induced tsunami waves, which were in the order of a few centimeters according to the inverted barometer principle, went through some amplification mechanisms approaching the coast. It is well known that the waves are highly amplified when the strict Proudman resonance conditions (atmospheric pressure speed ≈ celerity of long ocean waves) occur. However, in this case, although the strict Proudman conditions did not occur, which require larger depths for a pressure traveling speed of more than 1000 km/hr, sea level amplifications were observed where Proudman-like resonance conditions were reached in deeper areas. As a consequence, some locations experienced larger waves like the southeast coast of the Pacific, Japan and the Caribbean. Therefore, the observed sea level amplitudes did not only depend on the amplitude of the pressure wave but also on its traveling speed and the near and far-field bathymetric conditions. Another important parameter affecting the sea level amplitudes at some locations is the bandwidth (wavelength) of the pressure wave, as observed in New Zealand DART and Chichijima and Mera tide gauges in Japan, which are located near the deep trenches of the Pacific Ocean. Furthermore, although there are different suggested average traveling speed values for the pressure wave by different researchers, my preliminary simulations of ocean waves using different constant traveling pressure speeds

showed great discrepancies between the measured and computed values of the arrival time in different regions of the world. Therefore, considering this and the extracted speed values from the pressure data, a varying pressure speed was adopted.

In summary, the presented modeling approaches explain well the global propagation of air pressure waves caused by the HTHH volcanic explosion and ensuing tsunami in the oceans and marginal seas. The best simulation results are achieved by using varying speed, amplitude, and altitude for the traveling pressure wave globally. Although the modeling approaches neglect several factors such as the Earth's rotation and air compressibility and are based on some assumptions (e.g., dry air), both the observed pressure waves and the resulting water waves could be fairly reproduced by the proposed modeling approaches in both DART buoys and tide gauges around the globe. Other meteorological conditions (i.e., strong winds) during the passage of the pressure waves may also have distorted the pressure profiles.

The good agreement between the computed and measured sea levels in terms of both the arrival times and the amplitudes at several locations around the globe is promising. The suggested approaches can be alternative modeling applications for such phenomena. However, several local (non-source) factors were also effective on the observed waveforms (i.e., the wave envelope characteristic in Palermo-Sicily) in most of the locations and the models were also able to capture them fairly as long as the local conditions could be reflected in the model. On the other hand, Malta appears as a singularity where the delay between the pressure wave and the ocean wave arrivals could not be achieved satisfactorily, which is most probably due to some local conditions which require further detailed analysis focusing on the area.

REFERENCES

Abadie, S. M., Harris, J. C., Grilli, S. T. & Fabre, R. (2012). Numerical modeling of tsunami waves generated by the flank collapse of the Cumbre Vieja Volcano (La Palma, Canary Islands): Tsunami source and near field effects. Journal of Geophysical Research, https://doi.org/10.1029/2011jc007646

Airy, G. B. (1878). I. On the tides at Malta. Proceedings of the Royal Society of London, 26(179-184), 485-487.

Amores, A., Monserrat, S., Marcos, M., Argüeso, D., Villalonga, J., Jordà, G., & Gomis, D. (2022). Numerical Simulation of Atmospheric Lamb Waves Generated by the 2022 Hunga-Tonga Volcanic Eruption. Geophysical Research Letters, 49(6), https://doi.org/10.1029/2022GL098240.

An, C., Liu, P. L., & Seo, S. N. (2012). Large-scale edge waves generated by a moving atmospheric pressure. Theoretical and Applied Mechanics Letters, 2(4), 042001.

Bailey, K. E., DiVeglio, C., & Welty, A. (2014). An examination of the June 2013 East Coast meteotsunami captured by NOAA observing systems, NOAA technical report NOS CO-OPS, 79, https://repository.library.noaa.gov/view/noaa/14435, last accessed on 22.08.2020.

Bechle, A. J., & Wu, C. H. (2014). The Lake Michigan meteotsunamis of 1954 revisited. In Meteorological Tsunamis: The US East Coast and Other Coastal Regions (pp. 155-177). Springer, Cham.

Belousov, A., Voight, B., Belousova, M., Murveyev, Y. (2000). Tsunamis generated by subaquatic volcanic explosions: unique data from 1996 eruption in Karymskoye Lake, Kamchatka, Russia. Pure and Applied Geophysics, 157(6-8), 1135-1143.

Benjamin, M. (2015). A mathematical study of meteo and landslide tsunamis: the Proudman resonance. Nonlinearity, 28(11), 4037-4080.

Bonaccorso, A., Calvari, S., Garfi, G., Lodato, L., & Patane, D. (2003). Dynamics of the December 2002 flank failure and tsunami at Stromboli volcano inferred by volcanological and geophysical observations. Geophysical Research Letters, https://doi.org/10.1029/2003GL017702

Borrero, J. C., Solihuddin, T., Fritz, H. M., Lynett, P. J., Prasetya, G. S., Skanavis, V., ... & Synolakis, C. E. (2020). Field survey and numerical modelling of the December 22, 2018 Anak Krakatau tsunami. Pure and Applied Geophysics, 177(6), 2457-2475. https://doi.org/10.1007/s00024-020-02515-y

Bruins, H. J., MacGillivray, J. A., Synolakis, C. E., et al. (2008). Geoarchaeological tsunami deposits at Palaikastro (Crete) and the Late Minoan IA eruption of Santorini. Journal of Archaeological Science, https://doi.org/10.1016/j.jas.2007.08.017

Bubalo, M., Janeković, I. & Orlić, M. (2018). Chrystal and Proudman resonances simulated with three numerical models. Ocean Dynamics, 68(4-5), 497-507.

Bubalo, M., Janeković, I. & Orlić, M. (2019). Simulation of flooding and drying as an essential element of meteotsunami modelling. Continental Shelf Research, 184, 81-90.

Burt, S. (2022). Multiple airwaves crossing Britain and Ireland following the eruption of Hunga Tonga–Hunga Ha'apai on 15 January 2022. Weather, 77(3), 76-81.

Candella, R. N. (2009). Meteorologically induced strong seiches observed at Arraial do Cabo, RJ, Brazil. Physics and Chemistry of the Earth, Parts A/B/C, 34(17-18), 989-997.

Carvajal, M., Sepúlveda, I., Gubler, A., & Garreaud, R. (2022). Worldwide signature of the 2022 Tonga volcanic tsunami. Geophysical Research Letters, 49(6), https://doi.org/10.1029/2022GL098153.

Chen, Y. & Niu, X. (2018). Forced wave induced by an atmospheric pressure disturbance moving towards shore. Continental Shelf Research, 160, 1–9.

Cho, K. H., Choi, J. Y., Park, K. S., Hyun, S. K., Oh, Y., & Park, J. Y. (2013). A synoptic study on tsunami-like sea level oscillations along the west coast of Korea using an unstructured-grid ocean model. Journal of Coastal Research, 65, 678–683.

Choi, B. H., Pelinovsky, E., Kim, K. O., & Lee, J. S. (2003). Simulation of the trans-oceanic tsunami propagation due to the 1883 Krakatau volcanic eruption. Natural Hazards and Earth System Sciences, 3(5), 321–332.

Choi, Y. K., & Seo, S. N. (2017). Shock capturing shallow water model for long waves generated by a moving atmospheric pressure. Journal of Coastal Research, 79, 354-358.

Churchill, D. D., Houston, S. H., & Bond, N. A. (1995). The Daytona Beach wave of 3–4 July 1992: a shallow-water gravity wave forced by a propagating squall line. Bulletin of the American Meteorological Society, 76(1), 21-32.

Cita, M. B., & Aloisi, G. (2000). Deep-sea tsunami deposits triggered by the explosion of Santorini (3500 y BP), eastern Mediterranean. Sedimentary Geology, 135(1-4), 181-203.

Day, S. J. (2015). Volcanic tsunamis. In The Encyclopedia of Volcanoes, https://doi.org/10.1016/B978-0-12-385938-9.00058-4

Defant, A. (1961). Physical Oceanography, Vol.2, Pergamon Press, Oxford.

Denamiel, C., Šepić, J., Ivanković, D., & Vilibić, I. (2019). The Adriatic Sea and Coast modelling suite: Evaluation of the meteotsunami forecast component. Ocean Modelling, 135, 71-93.

Deplus, C., Bonvalot, S., Dahrin, D., Diament, M., Harjono, H. & Dubois, J. (1995). Inner structure of the Krakatoa volcanic complex (Indonesia) from gravity and bathymetry data. Journal of Volcanology and Geothermal Research, 64(1-2), 23-52.

Didenkulova, I. & Pelinovsky, E. (2012). Resonant generation of tsunami waves by submarine landslides in fjords. Proc. XXII International Offshore and Polar Engineering (ISOPE) Conference, Rhodos Greece, 17-22 June 2012, ISOPE-I-12-393.

Didenkulova, I. & Pelinovsky, E. (2013). Analytical solutions for tsunami waves generated by submarine landslides in narrow bays and channels. Pure and Applied Geophysics, 170(9-10), 1661-1671.

Didenkulova, I., Nikolkina, I. & Pelinovsky, E. (2011). Resonant amplification of tsunami waves generated by an underwater landslide. Doklady Earth Sciences, 436(1), 66-69.

Didenkulova, I., Nikolkina, I., Pelinovsky, E., & Zahibo, N. (2010). Tsunami waves generated by submarine landslides of variable volume: analytical solutions for a basin of variable depth. Natural Hazards and Earth System Sciences, 10(11), 2407-2419.

Dogan G. G., Yalciner, A. C., Annunziato A., Yalciner B. and Necmioglu O. (2022). Global Propagation of the Atmospheric Pressure Wave and the Consequent Tsunami due to the January 2022 Hunga Tonga-Hunga Ha'apai Eruption. Submitted to Proceedings of the National Academy of Sciences on 13.07.2022.

Dogan G. G., Annunziato A., Hidayat R., Husrin S., Prasetya G., Kongko W. et al. (2021a). Numerical simulations of December 22, 2018 Anak Krakatau tsunami and examination of possible submarine landslide scenarios. Pure and Applied Geophysics, 178(1), 1-20. https://doi.org/10.1007/s00024-020-02641-7.

Dogan G. G., Pelinovsky E., Zaytsev A., Metin, A. D., Ozyurt Tarakcioglu, G., Yalciner, A. C. et al. (2021b). Long wave generation and coastal amplification due to propagating atmospheric pressure disturbances. Natural Hazards, 106(2), 1195-1221. https://doi.org/10.1007/s11069-021-04625-9

Dogan, G. G., Yalciner, A. C., Yuksel, Y., Ulutaş, E., Polat, O., Güler, I. et al. (2021c). The 30 October 2020 Aegean Sea tsunami: post-event field survey

along Turkish coast. Pure and applied geophysics, 178(3), 785-812. https://doi.org/10.1007/s00024-021-02693-3

Dogan, G. G., Annunziato, A., Papadopoulos, G. A., Guler, H. G., Yalciner, A. C., Cakir, T. E., ... & Synolakis, C. (2019). The 20th July 2017 Bodrum–Kos Tsunami Field Survey. Pure and Applied Geophysics, 176(7), 2925-2949.

Dominey-Howes, D. (2004). A re-analysis of the Late Bronze Age eruption and tsunami of Santorini, Greece, and the implications for the volcano–tsunami hazard. Journal of Volcanology and Geothermal Research, 130(1-2), 107-132.

Donelan, M. A., Haus, B. K., Reul, N., Plant, W. J., Stiassnie, M., Graber, H. C., ... & Saltzman, E. S. (2004). On the limiting aerodynamic roughness of the ocean in very strong winds. Geophysical Research Letters, 31(18).

Donn, W. L. (1959). The Great Lakes storm surge of May 5, 1952. Journal of Geophysical Research, 64(2), 191-198.

Donn, W. L., & Ewing, M. (1956). Stokes' edge waves in Lake Michigan. Science, 124(3234), 1238-1242.

Dragani, W. C. (2007). Numerical experiments on the generation of long ocean waves in coastal waters of the Buenos Aires province, Argentina. Continental shelf research, 27(5), 699-712.

Dragani, W. C., D'Onofrio, E. E., Grismeyer, W., Fiore, M. M., & Campos, M. I. (2009). Atmospherically-induced water oscillations detected in the port of Quequén, Buenos Aires, Argentina. Physics and Chemistry of the Earth, Parts A/B/C, 34(17-18), 998-1008.

European Commission World Sea Levels, https://webcritech.jrc.ec.europa.eu/SeaLevelsDb/, last accessed on 03.06.2022.

Ewing, M., & Press, F. (1953). Further study of atmospheric pressure fluctuations recorded on seismographs. Eos, Transactions American Geophysical Union, 34(1), 95-100.

Ewing, M., & Press, F. (1955). Tide-gage disturbances from the great eruption of Krakatoa. Eos, Transactions American Geophysical Union, 36(1), 53-60.

Ewing, M., Press F. & Donn, W. L. (1954). An explanation of the Lake Michigan wave of 26 June 1954. Science, 120(3122), 684-686.

Eze, C. L., Uko, D. E., Gobo, A. E. T., Sigalo, F. B. & Israel-Cookey, C. (2009). Mathematical evaluation of tsunami propagation. Research Journal of Applied Sciences, 4(6), 213-216.

Fritz, H. M., Hager, W. H., & Minor, H. E. (2004). Near field characteristics of landslide generated impulse waves. Journal of waterway, port, coastal, and ocean engineering, 130(6), 287-302.

Gaertner, M. A., Jacob, D., Gil, V., Domínguez, M., Padorno, E., Sánchez, E., & Castro, M. (2007). Tropical cyclones over the Mediterranean Sea in climate change simulations. Geophysical Research Letters, 34(14).

Garratt, J. R. (1977). Review of drag coefficients over oceans and continents. Monthly weather review, 105(7), 915-929.

Garrett, C. J. R. (1970). A theory of the Krakatoa tide gauge disturbances, Tellus, 22(1), 43– 52.

Giachetti, T., Paris, R., Kelfoun, K., & Ontowirjo, B. (2012). Tsunami hazard related to a flank collapse of Anak Krakatau Volcano, Sunda Strait, Indonesia. Geological Society, London, Special Publications, 361(1), 79-90.

Glimsdal, S., Pedersen, G. K., Harbitz, C. B., & Løvholt, F. (2013). Dispersion of tsunamis: does it really matter?. Natural Hazards and Earth System Sciences, 13(6), 1507-1526.

Government of Tonga (2022), Media Release on 18 January 2022. http://itic.ioc-unesco.org/images/stories/list_of_tsunamis/2022/15Jan2022_Hunga-Tonga/Tonga_MediaRelease_20220118.pdf, last accessed on 18.04.2022.

Greenspan, H. P. (1956). The generation of edge waves by moving pressure distributions. Journal of Fluid Mechanics, 1(06), 574-592.

Grilli, S. T., Tappin, D. R., Carey, S., Watt, S. F., Ward, S. N., Grilli, A. R., Engwell, S.L., Zhang, C., Kirby, J.T., Schambach, L., Muin, M. (2019). Modelling of the tsunami from the December 22, 2018 lateral collapse of Anak Krakatau volcano in the Sunda Straits, Indonesia. Scientific reports, 9(1), 1-13.

Gusman, A.R. & Roger, J. (2022). Hunga Tonga - Hunga Ha'apai volcano-induced sea level oscillations and tsunami simulations. GNS Science webpage, https://doi.org/10.21420/DYKJ-RK41, last accessed on 10.02.2022.

Harkrider, D., & Press, F. (1967). The Krakatoa Air—Sea Waves: An Example of Pulse Propagation in Coupled Systems. Geophysical Journal International, 13(1-3), 149-159.

Heidarzadeh, M., Ishibe, T., Sandanbata, O., Muhari, A., & Wijanarto, A. B. (2020a). Numerical modeling of the subaerial landslide source of the 22 December 2018 Anak Krakatoa volcanic tsunami, Indonesia. Ocean Engineering, https://doi.org/10.1016/j.oceaneng.2019.106733

Heidarzadeh, M., Sepic, J., Rabinovich, A., Allahyar, M., Soltanpour, A., & Tavakoli, F. (2020b). Meteorological tsunami of 19 March 2017 in the

Persian Gulf: Observation and analyses. Pure and Applied Geophysics, 177(3), 1231-1259. https://doi.org/10.1007/s00024-019-02263-8.

Heidarzadeh, M., Putra, P.S., & Nugroho, S.H. (2020c). Field survey of tsunami heights and runups following the 22 December 2018 Anak Krakatau volcano tsunami, Indonesia. Pure and Applied Geophysics, submitted.

Heidarzadeh, M., Tappin, D.R., Ishibe, T. (2019). Modeling the large runup along a narrow segment of the Kaikoura coast, New Zealand following the November 2016 tsunami from a potential landslide. Ocean Engineering, 175, 113-121. https://doi.org/10.1016/j.oceaneng.2019.02.024.

Heidarzadeh, M., Krastel, S. & Yalciner, A.C., 2014. The state-of-the-art numerical models for modeling landslide tsunamis: a short review, in Submarine Mass Movements and Their Consequences, pp. 483–495, eds

Hibiya, T., & Kajiura, K. (1982). Origin of the Abiki phenomenon (a kind of seiche) in Nagasaki Bay. Journal of the Oceanographical Society of Japan, 38(3), 172-182.

Honda, K., Terada, T., Yoshida, Y., & Isitani, D. (1908). Secondary undulations of oceanic tides. Journal of the College of Science, Imperial University of Tokyo, 24, 1–110.

Horvath, K., & Vilibić, I. (2014). Atmospheric mesoscale conditions during the Boothbay meteotsunami: a numerical sensitivity study using a high-resolution mesoscale model. In: Vilibić I., Monserrat S., Rabinovich A.B. (eds) Meteorological Tsunamis: The US East Coast and Other Coastal Regions (pp. 55-74). Springer, Cham. https://meetingorganizer.copernicus.org/EGU2017/EGU2017-1246.pdf

Imamura, F. (1996). Review of tsunami simulation with a finite difference method. In: Yeh, Liu and Synolakis (eds) Long-wave runup models, World Scientific, Singapore, pp 25-42.

Imamura, F. and Imteaz M. M. A. (1995): Long waves in two-layers: governing equations and numerical model. Science of Tsunami Hazards, 13(1), 3-24.

Imamura, F., Yalciner, A. C. & Ozyurt, G. (2006). Tsunami modelling manual. UNESCO IOC international training course on Tsunami Numerical Modelling. http://www.tsunami.civil.tohoku.ac.jp/hokusai3/E/projects/manual-ver-3.1.pdf

IOC/UNESCO TOWS-WG Team, (2022). Report by IOC/UNESCO TOWS-WG Team on Atypical Tsunami Sources on 17.02.2022, http://www.ioc-tsunami.org/index.php?option=com_oe&task=viewEventDocs&eventID=3393, last accessed on 28.06.2022.

IOC/UNESCO TOWS-WG Team, (2020). Report of thirteenth meeting in Paris, France, 20–21 February, 2020, UNESCO Working Group on Tsunamis and Other Hazards Related to Sea-Level Warning and Mitigation Systems, unesdoc.unesco.org/ark:/48223/pf0000373571.locale=en)

Ioki, K., Tanioka, Y., Yanagisawa, H., & Kawakami, G. (2019). Numerical simulation of the landslide and tsunami due to the 1741 Oshima-Oshima eruption in Hokkaido, Japan. Journal of Geophysical Research, 124 (2), 1991–2002.

Kalligeris, N., Skanavis, V., Charalampakis, M., Melis, N. S., Voukouvalas, E., Annunziato, A., & Synolakis, C. E. (2021). Field survey of the 30 October 2020 Samos (Aegean Sea) tsunami in the Greek islands. Bulletin of Earthquake Engineering, 1-33.

Kânoğlu, U., Tanioka, Y., Okal, E. A., Baptista, M. A., & Rabinovich, A. B. (2019). Introduction to "Twenty-five years of modern tsunami science following the 1992 Nicaragua and Flores Island tsunamis, Volume I". Pure and Applied Geophysics, 176(7), 2757-2769.

Karstens, J., Berndt, C., Urlaub, M., et al. (2019). From gradual spreading to catastrophic collapse–Reconstruction of the 1888 Ritter Island volcanic sector collapse from high-resolution 3D seismic data. Earth and Planetary Science Letters, https://doi.org/10.1016/j.epsl.2019.04.009

Kawamata, K., Takaoka, K., Ban, K., Imamura, F., Yamaki, S., & Kobayashi, E. (2005). Model of tsunami generation by collapse of volcanic eruption: The 1741 Oshima-Oshima tsunami. In Tsunamis (pp. 79-96). Springer, Dordrecht.

Kian, R., Yalciner, A. C. & Zaytsev, A. (2014). Evaluating the performance of tsunami propagation models. Proceedings of the Forecast Engineering, Bauhaus Summer School, Weimar, Germany, 17-29.

Kim, J., Choi, B. J., & Omira, R. (2022). On the Greenspan resurgence of meteotsunamis in the Yellow Sea—insights from the newly discovered 11–12 June 2009 event. Natural Hazards, 1-18.

Kim, M.-S., Woo, S.-B., Eom, H., and You, S. H. (2021). Occurrence of pressure-forced meteotsunami events in the eastern Yellow Sea during 2010–2019, Nat. Hazards Earth Syst. Sci., 21, 3323–3337, https://doi.org/10.5194/nhess-21-3323-2021.

Kirby, J. T., Wei, G., Chen, Q., Kennedy, A. B., & Dalrymple, R. A. (1998). FUNWAVE 1.0: fully nonlinear Boussinesq wave model-Documentation and user's manual. research report NO. CACR-98-06, University of Delaware.

Knutson, T., McBride, J., Chan, J., Kerry, E., - Holland, G., Landsea, C., Held, I., Kossin, J. P., Srivastava, A. K., Sugi, Masato. (2010). Tropical cyclones and climate change. Nature Geosci 3, 157–163. https://doi.org/10.1038/ngeo779

Kowalik, Z. (2012). Introduction to Numerical Modeling of Tsunami Waves, Institute of Marine Science, University of Alaska, Fairbanks. 195 pp. https://www.sfos.uaf.edu/directory/faculty/kowalik/Tsunami_Book/book_sum.pdf.

Kusky T.M. (2022). Déjà vu: Might Future Eruptions of Hunga Tonga-Hunga Ha'apai Volcano be a Repeat of the Devastating Eruption of Santorini, Greece (1650 BC)?, Journal of Earth Science, 33(2), 229–235. https://doi.org/10.1007/s12583-022-1624-2

La Rocca, M., Galluzzo, D., Saccorotti, G., Tinti, S., Cimini, G. B., & Del Pezzo, E. (2004). Seismic signals associated with landslides and with a tsunami at Stromboli volcano, Italy. Bulletin of the Seismological Society of America, 94(5), 1850-1867.

Latcharote P., Suppasri A., Imamura F., Aytore B., Yalciner A.C. (2016). Possible worst-case tsunami scenarios around the Marmara Sea from combined earthquake and landslide sources. In Geist E.L., Fritz H.M., Rabinovich A.B., Tanioka Y. (eds) Global Tsunami Science: Past and Future, Volume I. Pageoph Topical Volumes. Birkhäuser, Cham

Latter, J.H., (1981). Tsunamis of volcanic origin: summary of causes, with particular reference to Krakatoa, 1883. Bulletin volcanologique, 44(3), 467-490.

Lavigne, F., Morin, J., Wassmer, P., Weller, O., Kula, T., Maea, A. et al. (2021). Bridging Legends and Science: Field Evidence of a Large Tsunami that Affected the Kingdom of Tonga in the 15th Century. Frontiers in Earth Science, 9. https://doi.org/10.3389/feart.2021.748755

Levin B.W.&Nosov, M.A. (2016) Physics of tsunamis, 2nd edn. Springer, Berlin

Lipa, B., Parikh, H., Barrick, D., Roarty, H., & Glenn, S. (2014). High-frequency radar observations of the June 2013 US East Coast meteotsunami. Natural Hazards, 74(1), 109-122.

Liu, P. L. F., Yeh, H., & Synolakis, C. E. (2008). Advanced numerical models for simulating Tsunami waves and run-up. Advances in Coastal and Ocean Engineering, 10, 344.

Liu, P. L. F., Monserrat, S., Marcos, M., & Rabinovich, A. B. (2003a). Coupling between two inlets: Observation and modeling. Journal of Geophysical Research: Oceans, 108(C3), 3069.

Liu, P. L. F., Lynett, P., & Synolakis, C. E. (2003b). Analytical solutions for forced long waves on a sloping beach. Journal of Fluid Mechanics, 478, 101-109.

Liu, P.L.-F., Cho, Y.-S., Briggs, M.J., Synolakis, C.E., Kanoglu, U. (1995). Run-up of solitary waves on a circular island. J. Fluid Mech. 302, 259–285.

Liu, P.L.-F., Cho, Y.-S., Yoon, S.B., Seo, S.N. (1994). Numerical simulations of the 1960 Chilean tsunami propagation and inundation at Hilo, Hawaii. In: El-Sabh, M.I. (Ed.), Recent Development in Tsunami Research. Kluwer Academic Publishers, pp. 99–115.

Lowe, D. J., & De Lange, W. P. (2000). Volcano-meteorological tsunamis, thec. AD 200 Taupo eruption (New Zealand) and the possibility of a global tsunami. The Holocene, 10(3), 401-407.

Lynett, P. (2022). The Tsunamis Generated by the Hunga Tonga-Hunga Ha'apai Volcano on January 15, 2022. https://doi.org/10.21203/rs.3.rs-1377508/v1

Lynett, P. J., Gately K., Wilson R., et al. (2017). Inter-model analysis of tsunami-induced coastal currents, Ocean Modelling, 114, 14–32. https://doi.org/10.1016/j.ocemod.2017.04.003

Mays, L.W., 2001. Water Resources Engineering. Wiley, New York

Melinand, B. (2015). A mathematical study of meteo and landslide tsunamis: the Proudman resonance. Nonlinearity, 28(11), 4037-4080.

Mercer, D., Sheng, J., Greatbatch, R. J., & Bobanović, J. (2002). Barotropic waves generated by storms moving rapidly over shallow water. Journal of Geophysical Research: Oceans, 107(C10), 16-1.

Metin, A.D. (2016). Long waves generation and coastal amplification due to atmospheric pressure disturbances. (Master's thesis), Middle East Technical University. Retrieved from http://etd.lib.metu.edu.tr/upload/12620257/index.pdf

Miles, J., & Munk, W. (1961). Harbor paradox. Journal of the Waterways and Harbors Division, 87(3), 111-132.

Mirchina, N. R., & Pelinovsky, E. N. (1982). Nonlinear and dispersive effects for tsunami waves in the open ocean. Int. J. Tsunami Soc, 2(4), 1073-1081.

Monserrat S., Vilibic I., and Rabinovich. A. B. (2006). Meteotsunamis: atmospherically induced destructive ocean waves in the tsunami frequency band, Nat. Hazards Earth Syst. Sci., 6(6), 1035-1051.

Monserrat, S., Ibbetson, A., & Thorpe, A. J. (1991). Atmospheric gravity waves and the ‘rissaga’ phenomenon. Quarterly Journal of the Royal Meteorological Society, 117(499), 553-570.

Muhari, A., Heidarzadeh, M., Susmoro, H., et al. (2019). The December 2018 Anak Krakatau Volcano tsunami as inferred from post-tsunami field surveys and spectral analysis. Pure and Applied Geophysics, 176(12), 5219-5233.

Murphy, O. (2019). Romantic Climates: A Change in the Weather. In Romantic Climates (pp. 1-16). Palgrave Macmillan, Cham.

Nappo CJ. (2013). An Introduction to Atmospheric Gravity Waves. New York: Academic. 359 pp. 2nd ed.

NASA (2022), Dramatic Changes at Hunga Tonga-Hunga Ha‘apai, https://earthobservatory.nasa.gov/images/149367/dramatic-changes-at-hunga-tonga-hunga-haapai, last accessed on 03.06.2022.

Nielsen, P. (2009), Coastal and Estuarine Processes. Advanced Series on Ocean Engineering, 29, World Scientific, Singapore.

Nishikawa, Y., Yamamoto, M. Y., Nakajima, K., Hamama, I., Saito, H., & Kakinami, Y. (2022). What excited tsunami from Tonga 2022 eruption? Observation and theory. https://doi.org/10.21203/rs.3.rs-1513574/v1

Nishimura, Y. (2008). Volcanism-induced tsunamis and tsunamiites. In Tsunamiites (pp. 163-184). Elsevier.

Niu, X. & Chen, Y. (2020). Energy accumulation during the growth of forced wave induced by a moving atmospheric pressure disturbance. Coastal Engineering Journal, 62(1), 23-34.

Niu, X. & Zhou, H. (2015). Wave pattern induced by a moving atmospheric pressure disturbance. Applied Ocean Research, 52, 37–42.

NOAA National Data Buoy Center (https://www.ndbc.noaa.gov/dart/dart.shtml), DART (Deep-ocean Assessment and Reporting of Tsunamis) buoys data, https://www.ngdc.noaa.gov/hazard/dart/2022tonga.html, last accessed on 03.06.2022.

Nomanbhoy, N., & Satake, K. (1995). Generation mechanism of tsunamis from the 1883 Krakatau eruption. Geophysical Research Letters, 22(4), 509-512.

Nomitsu, T. (1935). A theory of tsunamis and seiches produced by wind and barometric gradient. Memoirs of the College of Science; Kyoto Imperial University Series A, 18, 201–214.

Omira, R., & Ramalho, I. (2020). Evidence-calibrated numerical model of December 22, 2018, Anak Krakatau flank collapse and tsunami. Pure and Applied Geophysics, 177(7), 3059-3071.

Omira, R., Dogan, G. G., Hidayat, R., Husrin, S., Prasetya, G., Annunziato, A., ... & Yalciner, A. C. (2019). The September 28th, 2018, tsunami in Palu-Sulawesi, Indonesia: a post-event field survey. Pure and Applied Geophysics, 176(4), 1379-1395.

Omira, R., Quartau, R., Ramalho, I., Baptista, M. A., & Mitchell, N. C. (2016). The tsunami effects of a collapse of a volcanic island on a semienclosed basin:

The Pico-São Jorge Channel in the Azores Archipelago. Plate boundaries and hazards, 219, 271-287.

Orlić, M., Belušić, D., Janeković, I., & Pasarić, M. (2010). Fresh evidence relating the great Adriatic surge of 21 June 1978 to mesoscale atmospheric forcing. Journal of Geophysical Research: Oceans, 115(C6). https://doi.org/10.1029/2009JC005777

Papadopoulos, G. A. (1993). On some exceptional seismic (?) sea-waves in the Greek archipelago. Science of Tsunami Hazards, 11, 25-34.

Pararas-Carayannis, G. (1992). The tsunami generated from the eruption of the volcano of Santorin in the Bronze Age. Natural Hazards, 5(2), 115-123.

Paris, A., Heinrich, P., Paris, R., & Abadie, S. (2020). The December 22, 2018 Anak Krakatau, Indonesia, landslide and tsunami: preliminary modeling results. Pure and Applied Geophysics, 177(2), 571-590.

Paris R. (2015). Source mechanisms of volcanic tsunamis., Phil. Trans. R. Soc. A, 373(2053), 20140380. http://dx.doi.org/10.1098/rsta.2014.0380

Paris, R., Switzer, A. D., Belousova, M., Belousov, A., Ontowirjo, B., Whelley, P. L., & Ulvrova, M. (2014). Volcanic tsunami: a review of source mechanisms, past events and hazards in Southeast Asia (Indonesia, Philippines, Papua New Guinea). Natural Hazards, 70(1), 447-470.

Park, Y. H. (1986). Water characteristics and movements of the Yellow Sea Warm Current in summer. Progress in Oceanography, 17(3), 243-254.

Pasquet, S. & Vilibić, I. (2013). Shelf edge reflection of atmospherically generated long ocean waves along the central US East Coast. Continental Shelf Research, 66, 1-8.

Pattiaratchi, C. B., & Wijeratne, E. M. S. (2015). Are meteotsunamis an underrated hazard?. Philosophical Transactions of the Royal Society A: Mathematical, Physical and Engineering Sciences, 373(2053), 20140377.

Paxton, C. H. & Sobien, D. A. (1998). Resonant interaction between an atmospheric gravity wave and shallow water wave along Florida's west coast. Bulletin of the American Meteorological Society, 79(12), 2727-2732.

Pelinovsky E. (2006) Hydrodynamics of tsunami waves. In: Grue J., Trulsen K. (eds) Waves in Geophysical Fluids. CISM International Centre for Mechanical Sciences, vol 489. Springer, Vienna. https://doi.org/10.1007/978-3-211-69356-8_1

Pelinovsky, E., Choi, B. H., Stromkov, A., Didenkulova, I., & Kim, H. S. (2005). Analysis of tide-gauge records of the 1883 Krakatau tsunami. In K. Satake (Ed.), Tsunamis. Advances in natural and technological hazards research. vol 23. Dordrecht: Springer. https://doi.org/10.1007/1-4020-3331-1_4

Pelinovsky, E., Zahibo, N., Dunkley, P., Edmonds, M., Herd, R., Talipova, T., Kozelkov, A., Nikolkina, I. (2004). Tsunami generated by the volcano eruption on July 12–13, 2003 at Montserrat, Lesser Antilles. Science of Tsunami Hazards, 22(1), 44-57.

Pellikka, H., Rauhala, J., Kahma, K. K., Stipa, T., Boman, H., & Kangas, A. (2014). Recent observations of meteotsunamis on the Finnish coast. In Meteorological Tsunamis: The US East Coast and Other Coastal Regions (pp. 197-215). Springer, Cham.

Platzman GW (1958) A numerical computation of the surge of 26 June 1954 on Lake Michigan. Geophysica 6(1):407–438.

Powell, M. D., Vickery, P. J., & Reinhold, T. A. (2003). Reduced drag coefficient for high wind speeds in tropical cyclones. Nature, 422(6929), 279-283.

Proudman, J. (1929). The effects on the sea of changes in atmospheric pressure. Geophysical Supplements to the Monthly Notices of the Royal Astronomical Society, 2(4), 197-209.

Rabinovich, A. B. (2020). Twenty-seven years of progress in the science of meteorological tsunamis following the 1992 Daytona Beach event. Pure Appl. Geophys. 177, 1193–1230.

Rabinovich, A. B. (2009). Seiches and harbor oscillations. Handbook of coastal and ocean engineering, 193-236.

Rabinovich, A. B., & Monserrat, S. (1996). Meteorological tsunamis near the Balearic and Kuril Islands: Descriptive and statistical analysis. Natural Hazards, 13(1), 55-90.

Rabinovich, A. B., Monserrat, S., & Fain, I. V. (1999). Numerical modeling of extreme seiche oscillations in the region of the Balearic Islands. Oceanology, 39(1), 16–24.

Ramírez-Herrera, M.T., Coca, O. & Vargas-Espinosa, V. (2022) Tsunami Effects on the Coast of Mexico by the Hunga Tonga-Hunga Ha'apai Volcano Eruption, Tonga. Pure Appl. Geophys. 179, 1117–1137, https://doi.org/10.1007/s00024-022-03017-9

Romero, R., Vich, M., & Ramis, C. (2019). A pragmatic approach for the numerical prediction of meteotsunamis in Ciutadella harbour (Balearic Islands). Ocean Modelling, 142, 101441. https://doi.org/10.1016/j.ocemod.2019.101441

Sallenger Jr, A. H., List, J. H., Gelfenbaum, G., Stumpf, R. P., & Hansen, M. (1995). Large wave at Daytona Beach, Florida, explained as a squall-line surge. Journal of Coastal Research, 11(4), 1383-1388.

Satake, K., (2007). Volcanic origin of the 1741 Oshima-Oshima tsunami in the Japan Sea. Earth, planets and space, 59(5), 381-390.

Satake, K., and Kato, Y. (2001). The 1741 Oshima-Ohshima eruption: Extent and volume of submarine debris avalanche. Geophysical Research Letters, 28(3), 427-430.

Scorer, R. S. (1950). The dispersion of a pressure pulse in the atmosphere. Proceedings of the Royal Society of London. Series A. Mathematical and Physical Sciences, 201(1064), 137-157.

Šepić, J., Rabinovich, A. B. & Sytov, V. N. (2018). Odessa Tsunami of 27 June 2014: Observations and Numerical Modelling. Pure and Applied Geophysics, 175, 1545–1572.

Šepić, J., Vilibić, I., Rabinovich, A. B., & Monserrat, S. (2015). Widespread tsunami-like waves of 23-27 June in the Mediterranean and Black Seas generated by high-altitude atmospheric forcing. Scientific reports, 5(1), 1-8.

Šepić, J., Vilibić, I., & Strelec Mahović, N. (2012). Northern Adriatic meteorological tsunamis: Observations, link to the atmosphere, and predictability. Journal of Geophysical Research: Oceans, 117(C2). https://doi.org/10.1029/2011JC007608

Shuto, N., Goto, C., & Imamura, F. (1990). Numerical simulation as a means of warning for near-field tsunamis. Coastal Engineering in Japan, 33(2), 173-193.

Soloviev S. L., Go Ch. N. (1974) A catalogue of tsunamis on the western shore of the Pacific Ocean. Moscow, Russia: Academy of Sciences of the USSR, Nauka Publishing House.

Sozdinler, C. O., Yalciner, A. C., & Zaytsev, A. (2015). Investigation of tsunami hydrodynamic parameters in inundation zones with different structural layouts. Pure and Applied Geophysics, 172(3), 931-952.

Sun, Q., & Niu, X. (2021). Harbor oscillation induced by atmospheric pressure disturbances moving in different directions. Coastal Engineering Journal, 1-12.

Syamsidik, B., Luthfi, M., Suppasri, A., & Comfort, L. K. (2020). The 22 December 2018 Mount Anak Krakatau volcanogenic tsunami on Sunda Strait coasts, Indonesia: tsunami and damage characteristics. Natural Hazards and Earth System Sciences, 20(2), 549-565.

Takabatake T., Shibayama T., Esteban M., et al. (2019). Field survey and evacuation behaviour during the 2018 Sunda Strait tsunami, Coastal Engineering Journal, https://doi.org/10.1080/21664250.2019.1647963

Tanaka, K. (2010). Atmospheric pressure-wave bands around a cold front resulted in a meteotsunami in the East China Sea in February 2009. Natural Hazards and Earth System Sciences, 10(12), 2599-2610.

Thiebaut, S., & Vennell, R. (2011). Resonance of long waves generated by storms obliquely crossing shelf topography in a rotating ocean. Journal of fluid mechanics, 682, 261–288.

Tinti, S. & Bortolucci, E. (2000). Analytical investigation of tsunamis generated by submarine slides. Annali di Geofisica, 43, 519–536.

Tinti, S., Bortolucci, E., & Chiavettieri, C. (2001). Tsunami excitation by submarine slides in shallow-water approximation. Pure and Applied Geophysics, 158(4), 759-797.

Tinti, S., Bortolucci, E., & Romagnoli, C. (2000). Computer simulations of tsunamis due to sector collapse at Stromboli, Italy. Journal of Volcanology and Geothermal Research, 96(1-2), 103-128.

Tinti, S., Maramai, A., Armigliato, A., et al. (2006). Observations of physical effects from tsunamis of December 30, 2002 at Stromboli volcano, southern Italy. Bulletin of Volcanology, 68(5), 450-461.

Titov, V. V. & Synolakis, C. E. (1998). Numerical modeling of tidal wave run-up. Journal of Waterway, Port, Coastal and Ocean Engineering, 124(4), 157-171.

Toffoli, A., & Bitner-Gregersen, E. M. (2017), Types of ocean surface waves, wave classification, Encyclopedia of maritime and offshore engineering, 1-8.

Torsvik, T., Paris, R., Didenkulova, I., Pelinovsky, E., Belousov, A., & Belousova, M. (2010). Numerical simulation of tsunami event during the 1996 volcanic eruption in Karymskoe lake, Kamchatka, Russia. Natural Hazards and Earth System Sciences, 10(11), 2359-2369.

Triantafyllou, I., Gogou, M., Mavroulis, S., Lekkas, E., Papadopoulos, G. A., & Thravalos, M. (2021). The tsunami caused by the 30 October 2020 Samos (Aegean Sea) Mw7. 0 earthquake: hydrodynamic features, source properties and impact assessment from post-event field survey and video records. Journal of Marine Science and Engineering, 9(1), 68.

Turkish State Meteorological Service, https://mgm.gov.tr/, last accessed on 03.06.2022

UNESCO IOC Sea Level Station Monitoring Facility, https://www.ioc-sealevelmonitoring.org/, last accessed on 03.06.2022.

UNESCO IOC-ITIC (2022), How do earthquakes generate tsunamis?, http://itic.ioc-unesco.org/index.php?option=com_content&view=article&id=1158&Itemid=2026, Last accessed on 15.06.2022.

UNESCO-ITST (2014). International Tsunami Survey Team (ITST) Post-Tsunami Survey Field Guide. 2nd Edition. IOC Manuals and Guides No.37, Paris: UNESCO 2014 (English).

USGS (2022), U.S. Geological Survey M 5.8 Volcanic Eruption - 68 km NNW of Nuku'alofa, Tonga, https://earthquake.usgs.gov/earthquakes/eventpage/pt22015050/executive, Last accessed on 18.04.2022.

Velioglu-Sogut, D., Yalciner, A. C. (2019). Performance comparison of NAMI DANCE and FLOW-3D® models in tsunami propagation, inundation and currents using NTHMP benchmark problems. Pure and Applied Geophysics, 176, 3115-3153.

Vennell, R. (2007). Long barotropic waves generated by a storm crossing topography. Journal of Physical Oceanography, 37(12), 2809–2823.

Vennell, R. (2010). Resonance and trapping of topographic transient ocean waves gener ated by a moving atmospheric disturbance. J. Fluid Mech, 650, 427–442.

Vilibić, I. (2008). Numerical simulations of the Proudman resonance. Continental Shelf Research, 28(4-5), 574-581.

Vilibić, I., Domijan, N., Orlić, M., Leder, N., & Pasarić, M. (2004). Resonant coupling of a traveling air pressure disturbance with the east Adriatic coastal waters. Journal of Geophysical Research: Oceans, 109(C10). https://doi.org/10.1029/2004JC002279

Vilibić, I., Monserrat, S., Rabinovich, A., & Mihanović, H. (2008). Numerical modelling of the destructive meteotsunami of 15 June, 2006 on the coast of the Balearic Islands. Pure and Applied geophysics, 165(11), 2169-2195.

Vilibić, I., Šepić, J., Ranguelov, B., Mahović, N. S., & Tinti, S. (2010). Possible atmospheric origin of the 7 May 2007 western Black Sea shelf tsunami event. Journal of Geophysical Research: Oceans, 115(C7). DOI: 10.1029/2009JC005904

Vučetić, T., Vilibić, I., Tinti, S., & Maramai, A. (2009). The Great Adriatic flood of 21 June 1978 revisited: An overview of the reports. Physics and Chemistry of the Earth, Parts A/B/C, 34(17-18), 894-903.

Walsh, K. J., Camargo, S. J., Knutson, T. R., Kossin, J., Lee, T. C., Murakami, H., & Patricola, C. (2019). Tropical cyclones and climate change. Tropical Cyclone Research and Review, 8(4), 240-250.

Walsh, K.J.E., Nguyen, K.-C., McGregor, J.L., 2004. Fine-resolution regional climate model simulations of the impact of climate change on tropical cyclones near Australia. Climate Dynamics 22, 47–56.

Walsh, K. J., McInnes, K. L., & McBride, J. L. (2012). Climate change impacts on tropical cyclones and extreme sea levels in the South Pacific—A regional assessment. Global and Planetary Change, 80, 149-164.

Walter, T. R., Haghighi, M. H., Schneider, F. M., et al. (2019). Complex hazard cascade culminating in the Anak Krakatau sector collapse. Nature communications, 10(1), 1-11.

Wang, X., Li, K., Yu, Z., & Wu, J. (1987). Statistical characteristics of seiches in Longkou Harbour. Journal of physical oceanography, 17(7), 1063-1065.

Ward, S.N. & Day, S.J., (2003). Ritter Island Volcano Lateral collapse and tsunami of 1888. Geophysical Journal International, 154(3), 891-902.

Watts, P., Grilli, S. T., Kirby, J. T., Fryer, G. J., & Tappin, D. R. (2003). Landslide tsunami case studies using a Boussinesq model and a fully nonlinear tsunami generation model. Natural Hazards and Earth System Sciences, 3(5), 391-402.

Weathernews Inc. barometric pressure data, from https://global.weathernews.com/news/16551/, last accessed on 03.06.2022

Williams, D. A., Horsburgh, K. J., Schultz, D. M., & Hughes, C. W. (2021). Proudman resonance with tides, bathymetry and variable atmospheric forcings. Natural Hazards, 106(2), 1169-1194.

Williams, R., Rowley, P., & Garthwaite, M. C. (2019). Reconstructing the Anak Krakatau flank collapse that caused the December 2018 Indonesian tsunami. Geology, 47(10), 973-976.

Wood, G. D. A. (2014). Tambora: the eruption that changed the world. Princeton University Press.

Yalciner A. C., Alpar B., Altinok Y., Ozbay I., Imamura F., (2002). Tsunamis in the Sea of Marmara: Historical Documents for the Past, Models for Future. Special Issue of Marine Geology, 190(1-2), 445-463.

Yalciner, A. C. & Pelinovsky, E. (2007). A short cut numerical method for determination of resonance periods of free oscillations in irregular shaped basins, Ocean Engineering, 34(5-6), 747-757.

Yalciner, A. C., Zaytsev, A., Aytore, B., Insel, I., Heidarzadeh, M., Kian, R., & Imamura, F. (2014). A possible submarine landslide and associated tsunami at the Northwest Nile Delta, Mediterranean Sea. Oceanography, 27(2), 68–75.

Yalciner, B. & Zaytsev, A. (2017). Assessment of efficiency and performance of tsunami numerical modeling with GPU. Abstract EGU2017-1246 Presented in European Geoscience Union, EGU April 2017.

Yavari-Ramshe, S., & Ataie-Ashtiani, B. (2016). Numerical modeling of subaerial and submarine landslide-generated tsunami waves—recent advances and future challenges. Landslides, 13(6), 1325-1368.

Yeh, H. H., Liu, P. L., & Synolakis, C. (Eds.). (2008). Advanced numerical models for simulating tsunami waves and runup (Vol. 10). World Scientific.

Yokoyama I. 1987 A scenario of the 1883 Krakatau tsunami. J. Volcanol. Geotherm. Res. 34, 123–132, doi:10.1016/0377-0273(87)90097-7.

A. Supplementary Files

1. Video presentation of the simulated pressure waves and water level based on the synthetic pressure model from t=0 to t=36 hr.
2. Video presentation of the simulated pressure waves and water level based on the pressure fields from hydrodynamic simulations from t=0 to t=36 hr.

The files are available at:

https://drive.google.com/drive/folders/19D7vE07uyDynill6Yk7d0cxvR8geb6Ec?usp=sharing

NOTE: If the URLs above do not work, you can request the files via e-mail from gguneydogan@gmail.com.

CURRICULUM VITAE

Surname, Name: Doğan Bingöl, Gözde Güney
Date and Place of Birth: 25 January 1989, Ankara
Phone: +90 505 490 91 20
email: gguneydogan@gmail.com, guneydo@metu.edu.tr

EDUCATION

Degree	Institution	Year of Graduation
MS	METU Civil Engineering	2016
BS	METU Civil Engineering	2013
High School	Ankara Atatürk Anadolu High School	2007

WORK EXPERIENCE

Year	Institution	Enrollment
2017 - Current	METU Civil Engineering	Project Assist.
2013-2016	METU Civil Engineering	Research Asssist.

FOREIGN LANGUAGES

Advanced English, Beginner Spanish

PUBLICATIONS

Journal Publications

1. **Dogan G. G.**, Yalciner A. C., Annunziato A., Yalciner B., Necmioglu O. (2022), Global Propagation of the Atmospheric Pressure Wave and the Consequent Tsunami due to the January 2022 Hunga Tonga-Hunga Ha'apai Eruption. Submitted to *Proceedings of the National Academy of Sciences* on 13.07.2022.
2. **Dogan G. G.**, Yalciner A. C., Yuksel Y., Ulutas E., Polat O., Guler I., Şahin C., Tarih A., Kanoglu U., (2021), The 30 October 2020 Aegean Sea Tsunami: Post-Event Field Survey Along Turkish Coast, *Pure and Applied Geophysics*, 178(3), 785-812. https://doi.org/10.1007/s00024-021-02693-3

3. **Dogan, G.G.**, Annunziato, A., Hidayat, R., Semeidi Husrin, Prasetaya G., Kongko W., Zaytsev A., Pelinovsky E., Imamura F., Yalciner A. C., (2021), Numerical Simulations of December 22, 2018 Anak Krakatau Tsunami and Examination of Possible Submarine Landslide Scenarios. *Pure and Applied Geophysics.* 178, 1–20. https://doi.org/10.1007/s00024-020-02641-7

4. **Dogan G.G.**, Pelinovsky E., Zaytsev A., Metin A. D., Tarakcioglu G. O., Yalciner A. C., Yalciner B., Didenkulova I, (2021), Long wave generation and coastal amplification due to propagating atmospheric pressure disturbances. *Natural Hazards*, 106(2), 1195-1221. https://doi.org/10.1007/s11069-021-04625-9

5. **Dogan G.G.,** Annunziato A, Papadopoulos G. A., Guler H. G., Yalciner A. C., Cakir T. E., Ozer Sozdinler C., Ulutas E., Arikawa T., Suzen M. L., Guler I., Probst P., Kanoglu U., Synolakis C. (2019), "The 20th July 2017 Bodrum-Kos Tsunami Field Survey", *Pure and Applied Geophysics*, 176: 2925 https://doi.org/10.1007/s00024-019-02151-19

6. Tufekci-Enginer D., **Dogan G.G.,** Suzen M.L., Yalciner A.C., (2022) "Performance analysis of open-source DEMs in tsunami inundation modelling", *Earth Science Informatics*, in revision process.

7. Omira R., **Dogan G. G.,** Hidayat R., Husrin S., Prasetya G., Annunziato A., Proietti C., Probst P., Paparo M.A., Wronna M., Zaytsev A., Pronin P., Giniyatullin A., Putra P.S., Hartanto D., Ginanjar G., Kongko W., Pelinovsky E., Yalciner A.C. (2019), "The September 28th, 2018, Tsunami in Palu-Sulawesi, Indonesia: A Post-Event Field Survey", *Pure and Applied Geophysics*, 176(4), 1379-1395.

8. Heidarzadeh, M., Pranantyo, I.R., Okuwaki, R., **Dogan G.G.** and Yalciner A.C. (2021). "Long Tsunami Oscillations Following the 30 October 2020 Mw 7.0 Aegean Sea Earthquake: Observations and Modelling", *Pure and Applied Geophysics*, 178, 1531–1548. https://doi.org/10.1007/s00024-021-02761-8

9. Zaytsev A, Pelinovsky E., **Dogan G.G.**, Yalciner B., Yalciner A., Kurkin A., Moskvitin A.A. (2020), Numerical Simulation of the Storm Surge at the Sakhalin Island Southern Part on November 15, 2019, *Morskoy Gidrofizicheskiy Zhurnal*, https://doi.org/10.22449/0233-7584-2020-4-396-406

10. Zaytsev, A., Pelinovsky, E., Yalciner A.C., Susmoro H., Prasetya G., Hidayat R., Dolgikh G.I., Dolgikh, S.G., Kurkin, A., **Dogan, G.G.**, Zahibo, N., Pronin P. (2019), Generation of the 2018 Tsunami on Sulawesi Island: Possible Sources, In *Doklady Earth Sciences*, 486(1), 588-592.

11. Lynett, P. J., Gately K., Wilson R., Montoya L., Arcas D., Aytore B., Bai Y., Bricker J. D., Castro M. J., Cheung, K. F. David G. C., **Dogan G. G.**, Escalante C., González-Vida J. M., Grilli S. T., Heitmann T. W., Horrillo

J., Kânoglu U., Kian R., Kirby J. T., Li W., Macías J., Nicolsky D. J., Ortega S., Pampell-Manis A., Park Y. S., Roeber V., Sharghivand N., Shelby M., Shi F., Tehranirad B., Tolkova E., Thio H. K., Velioglu D., Yalciner A. C., Yamazaki Y., Zaytsev, A., Zhang Y. J., 2017, "Inter-model analysis of tsunami-induced coastal currents", *Ocean Modelling*, 114, 14–32.

12. Guler H. G., Cinar G. E., Sharghivand N., Sozdinler C. O., **Dogan G. G.,** Necmioglu O., Zaytsev A., Yalciner A. C. (2017), "Tsunami Action on Coasts and Constructions", Fundamental and Applied Geophysics (Fundamentalnaya I Prikladnaya Gidrofzika), 10(3), 65-72.
13. Harbitz C.B., Nakamura Y., Arikawa T., Baykal C., **Dogan G. G.,** Frauenfelder R., Glimsdal S., Guler H. G., Issler D., Kaiser G., Kanoglu U., Kisacik D., Kortenhaus A., Løvholt F., Maruyama Y., Sassa S., Sharghivand N., Strusinska-Correia A., Tarakcioglu G. O., Yalciner A. C. (2016), ''Risk Assessment and Design of Prevention Structures for Enhanced Tsunami Disaster Resilience (RAPSODI)/Euro-Japan Collaboration'', *Coastal Engineering Journal*, Vol. 58, No. 4.

Conference Proceedings

1. **Dogan G.G.**, Yalciner A.C., Annunziato A., Yalciner B., Necmioglu O. (2022) "Numerical Modeling of Global Propagation of Pressure Wave and Consequent Water Waves due to January 2022 Hunga Tonga-Hunga Ha'apai Eruption", 2nd World Conference on Meteotsunamis, 18-20 May 2022, Menorca, Spain.
2. **Dogan G.G.,** Yalciner A.C. (2021), **Invited Talk,** Analysis of the October 30th, 2020 Aegean Sea Tsunami Towards Future Tsunami Preparedness, EGU General Assembly 2021, Seismic Hazard Assessments and Disaster Resilience Session, April 2021, Wien, Austria.
3. **Dogan G.G.**, Yalciner A.C, Tufekci-Enginar D., Suzen M.L. (2022). "Numerical Modeling of the 30 October 2020 Seferihisar-Izmir (Aegean Sea) Tsunami and Its Coastal Effects", 14th International Conference on Hydroscience and Engineering, 26-27 May 2022, Izmir, Turkey.
4. **Dogan G.G.**, Annunziato A., Hidayat R., Husrin S., Prasetya G., Kongko W., Zaytsev A., Pelinovsky E., Imamura F., Yalciner A.C. (2019), "Investigation of December 22, 2018 Anak Krakatau Tsunami and Possible Future Events by Numerical Modeling", 27th IUGG General Assembly, Joint Tsunami Symposium (JP-05), 8-18 July 2019, Montreal, Canada.
5. Yalciner A.C., Hidayat R., Husrin S., Annunziato A., **Dogan G. G.,** Zaytsev A., Omira R., Proietti C., Probst P., Paparo M.A., Wronna M., Pronin P., Giniyatullin A., Putra P., Kongko W., Hartanto D., Pelinovsky E., Ginanjar G., "Field Survey on the Coastal Impacts of the September 28, 2018 Palu, Indonesia Tsunami", Poster, AGU Fall Meeting 2018 Washington D.C.

6. **Dogan G. G.,** Yalciner A.C., Tüfekçi Enginar D., Süzen M.L., Yalciner B., "Bodrum-Kos Deprem ve Tsunamisinin Kıyılardaki Etkilerinde Karaada'nın Rolü" (in Turkish), 71. Jeoloji Kurultayı, April 2018, Ankara, Turkey.

7. Yalciner A.C., Annunziato A., Papadopoulos G.A., **Dogan G. G.,** Guler H.G., Cakir T.E., Sozdinler C.O, Ulutas E., Arikawa T., Suzen L., Tufekci Enginar D., Kanoglu U., Guler I., Synolakis C., (2018), "The July 20, 2017 (22:31 UTC) Bodrum/Kos Earthquake and Tsunami; Field Surveys, Lessons and Modeling", ICCE 2018, Baltimore.

8. **Dogan G. G.**, Yalciner A.C., Kilic N., Yucemen S., "Tsunami Hazard Assessment for Izmir Bay, Turkey", 16th European Conference on Earthquake Engineering, Thessaloniki, Greece, June 2018.

9. **Dogan G. G.** and Yalciner A.C., "Deterministic and Probabilistic Tsunami Hazard Assessment for Inner Basin of Izmir Bay by High Resolution Tsunami Inundation Modeling", European Geoscientists Union (EGU) General Assembly 2018, April 2018, Wien, Austria.

10. Tufekci Enginar D., Suzen M.L., Yalciner A.C., Kolat C.**, Dogan G. G.**, Yalciner B, and Zaytsev A., "Tsunami Human Vulnerability Assessment of Silivri District, Istanbul", European Geoscientists Union (EGU) General Assembly 2018, April 2018, Wien, Austria.

11. Papadopoulos G., Annunziato A., Yalciner A.C., Agalos A., Charalampakis M., **Dogan G. G.**, Necmioglu O., Ozer Sozdinler C., Novikova T., Probst P., and Proietti C., "The east Aegean Sea seismic tsunamis of 12 June and 20 July 2017: lessons learned for the tsunami potential and the early warning in the Mediterranean", European Geoscientists Union (EGU) General Assembly 2018, April 2018, Wien, Austria.

12. Yalciner A.C., Annunziato A., Papadopoulos G.A., **Dogan G. G.,** Guler H.G., Cakir T.E., Sozdinler C.O, Ulutas E., Arikawa T., Suzen L., Kanoglu U., Guler I., Probst P., Synolakis C., "The Bodrum-Kos strong (Mw6.6) earthquake and the associated tsunami of 20 July 2017: results of post-event field surveys", International Tsunami Symposium, ITS 2017, Bali, Flores.

13. Papadopoulos G.A., Agalos A., Charalampakis M., Novikova T., Triantafyllou I., Annunziato A., Probst P., Proietti Ch., Kleanthi M., Necmioğlu Ö., Sozdinler C. Ö., **Dogan G. G.,** Yalciner A. C., "The Lesvos Isl. (East Aegean Sea) strong (Mw6.3) earthquake and the associated tsunami of 12 June 2017", International Tsunami Symposium, ITS 2017, Bali, Flores.

14. **Dogan G.G.,** Tarakcıoğlu Ozyurt G., Baykal C.,''Performance of Rubble Mound and Caisson Type Breakwaters under Extreme Waves'', International Conference on Coastal Engineering, ICCE 2016, Antalya, Turkey.

15. Pekcan O., Ersöz A.B., Teke T., **Dogan G. G.,** Tarakcıoğlu G.O., Baykal C., "Damage Identification of Coastal Structures Using Image Processing

Techniques", International Conference on Coastal Engineering, ICCE 2016, Antalya, Turkey.

16. **Dogan G. G.,** Tarakcıoğlu Ozyurt G., Baykal C., ''Modelling of Performance of Caisson Type Breakwaters under Extreme Waves'', European Geoscientists Union General Assembly 2016, Wien, Austria
17. **Dogan G. G.,** Tarakcıoğlu Ozyurt G., Baykal C., ''Taş Dolgu ve Keson Tipi Dalgakıran Performanslarının Ekstrem Dalgalar Altında Fiziksel Model Deneyleri ile İncelenmesi'' (in Turkish), Türkiye Deniz Bilimleri Konferansı (National), 2016, Turkey
18. **Dogan G. G.,** Tarakcıoglu Ozyurt G., ''Failure Mechanisms of Coastal Protection Structures under Tsunamis'', YCSEC 2015, Manchester, UK
19. **Dogan G. G.,** Tarakcıoglu Ozyurt G., Yalciner A.C., 'Kıyı Koruma Yapılarının Tsunami Yükleri Altındaki Hasar Mekanizmaları'' (in Turkish), 8th Coastal Engineering Symposium (National), 2015, Turkey.

RESEARCH PROJECTS

- UNESCO IOC CoastWAVE Project, "Strengthening the Resilience of Coastal Communities in the North East Atlantic, Mediterranean Region to the Impact of Tsunamis and Other Sea Level-Related Coastal Hazards", ongoing, funded by EU DG ECHO
- "Tsunami Hazard Assessment, Vulnerability and Risk Analysis for the Izmir Metropolitan Coast, supported by Izmir Metropolitan Municipality", January 2022 – ongoing
- "Fault Based Probabilistic Tsunami Generation and Hazard Analysis for Aegean Coasts: Online Interactive Tsunami Information System", The Scientific and Technological Research Council of Turkey (TUBITAK) funded, January 2022 – ongoing
- "The Risk Assesment and the Development Of Disaster Prevention Methods For the Tsunami Induced Hazards In Ports Considering the Floating Docks, the Marine Vessels, the Sea Bed Scour and the Deposition", January 2022 – ongoing
- "Istanbul City Tsunami Action Plan Project", supported by Istanbul Metropolitan Municipality, April 2019 – December 2019
- "The Tsunami LAST-MILE Project", "Supply and installation of two Seismic Alert Systems (SASs) and related services", European Commission (EC), JRC/IPR/2018/E.1/0018/NC-ExA, January 2018 – September 2019
- "Tsunami Hazard Assessment, Vulnerability and Risk Analysis for the Marmara Coast of Istanbul Metropolitan Municipality", supported by Istanbul Metropolitan Municipality, August 2017 – December 2018

- European Union, Humanitarian Aid and Civil Protection, DG-ECHO Project TSUMAPS-NEAM, "Probabilistic TSUnami Hazard MAPS for the NEAM Region", ECHO/SUB/2015/718568/PREV26 (Completed, 2018).
- ERASMUS+ Project DESIMAR, "Parametric Design for Marine and Coastal Structures", 2017-2-TR01-KA205-047156, (2017-2019)
- ASTARTE Project "Assessment, STrategy And Risk Reduction for Tsunamis in Europe", FP7 Framework of European Union (EU), November 2013 - April 2017
- RAPSODI Project "Risk Assessment and design of Prevention Structures fOr enhanced tsunami DIsaster resilience", CONCERT-Japan Research and Innovation Consortium, July 2013 - July 2015.

OTHER ACADEMIC ACTIVITIES

- 2022: Reviewer in Natural Hazards
- 2021: Session Chair, "Sources and Uncertainties in Tsunami Hazard Assessment" in 30th International Tsunami Symposium, 2021, Sendai, Japan

Important Events Attended

- Researcher, Leading team member of National Tsunami Suvery Teams, Post-tsunami Field Survey of 30th October, 2020 Aegean Sea Tsunami, 31 October – 01 November & 04-06 November, 2020, Izmir Coast in Kusadasi Bay, Aegean Sea, Turkey
- Researcher, Team member of UNESCO International Tsunami Suvery Team, "Post-tsunami Field Survey of 28th September, 2018, Palu Sulawesi Earthquake and Tsunami", November 07-11, 2018, Palu Sulawesi, Indonesia.
- Graduate Student, "Japan-Turkey Student Exchange program on Resilience Engineering for Energy and Urban Systems", University of Tokyo, July 15-28, 2018, Japan.
- Researcher, Team member of National and International Tsunami Suvery Teams, Post-tsunami Field Survey of 20th July, 2017 Bodrum-Kos Earthquake and Tsunami Event, 22-23 July 2017, Bodrum Peninsula-Aegean Sea, Turkey
- Guest Project Assistant, Technical University of Braunschweig, June-July, 2014, Braunschweig, Germany, Laboratory Experiments within RAPSODI Project, "Risk Assessment and design of Prevention Structures fOr enhanced tsunami DIsaster resilience", CONCERT-Japan Research and Innovation Consortium